**This preprint is not an accepted peer-reviewed manuscript. A version of this preprint has been resubmitted to *Journal of Petrology* following one round of peer-review.**

# Persistent high-pressure magma storage beneath a near-ridge ocean island volcano (Isla Floreana, Galápagos)

Matthew Gleeson[1,2]*, Penny Wieser[1], Charlotte L. DeVitre[1], Sarah C. Shi[1,3], Marc-Alban Millet[2], Duncan D. Muir[2], Michael J. Stock[4], and Johan Lissenberg[2]

[1]Department of Earth and Planetary Science, University of California, Berkeley, McCone Hall, 94720, USA

[2]School of Earth and Environmental Sciences, Cardiff University, Main Building, Park Place, CF10 3AT, UK

[3]Lamont-Doherty Earth Observatory, Columbia University. New York, NY USA

[4]Discipline of Geology, School of Natural Sciences, Trinity College Dublin, Dublin 02, Ireland

## ABSTRACT

Volcanic evolution in ocean island settings is often controlled by variations in the chemistry and volumetric flux of magma from an underlying mantle plume. In locations such as Hawai'i or Réunion, this results in predictable variations in magma chemistry, the rate of volcanic activity, and the depth of magma storage with volcanic age and/or distance from the center of plume upwelling. These systems, however, represent outliers in global plume volcanism due to their high buoyancy flux, frequent eruptions, and large distance from any plate boundary. Most mantle plumes display clear interaction with nearby plate boundaries, influencing the dynamics of solid plume material in the upper mantle and the distribution of melt across regions of active volcanism. Yet, the influence of plume-ridge interaction and plume-ridge distance on the structure, characteristics, and evolution of magma storage beneath ocean island volcanoes remains under constrained. In this study, we consider the evolution of magmatic systems in the Galápagos Archipelago, a region of mantle plume

volcanism located 150-250 km south of the Galápagos Spreading Centre (GSC), focusing on the depth of magma storage during the eastward transport of volcanic systems away from the centre of plume upwelling. Geochemical analysis of gabbro xenoliths from Isla Floreana in the south-eastern Galápagos suggest that they formed at ~2-2.5 Ma, when the island was located close to the centre of plume upwelling. These nodules, therefore, provide rare insights into the evolution of volcanic systems in the Galápagos Archipelago, tracking variations in the magma system architecture as the Nazca plate carried Isla Floreana eastwards, away from the plume centre.

Mineral thermobarometry, thermodynamic modelling, and $CO_2$ fluid inclusion barometry reveal that Isla Floreana's plume-proximal stage of volcanic activity – recorded in the gabbro xenoliths – was characterized by the presence of high-pressure magma storage (> 25 km), below the base of the crust. In fact, we find no petrological evidence that sustained, crustal-level magma storage ever occurred beneath Isla Floreana. Our results contrast with the characteristics of volcanic systems in the western Galápagos above the current centre of plume upwelling, where mid-crust magma storage has been identified. We propose that this change in magmatic architecture of plume-proximal volcanic centres in the Galápagos – from high-pressure mantle storage at 2.5 Ma to mid-crustal storage at the present day – is controlled by the variations in plume-ridge distance. Owing to the northward migration of the GSC, the distance separating the plume stem and GSC is not constant, and was likely <100 km at 2.5 Ma, significantly less than the current plume-ridge distance of 150 – 250 km. We propose that smaller plume-ridge distances result in greater diversion of plume-material to the GSC, 'starving' the eastern Galápagos islands of magma during their initial formation and restricting the ability for these systems to develop long-lived crustal magma reservoirs.

# 1 INTRODUCTION

Ocean island volcanoes, primarily formed through melting of anomalously hot, hydrous, or lithologically distinct mantle plumes, represent some of the most active volcanic systems in the world (Harpp and Weis, 2020; Herzberg et al., 2014; Matthews et al., 2021; Métrich et al., 2014; Neal et al., 2019; Sobolev et al., 2007; Weis et al., 2023). Owing to the deep-mantle origin of many mantle plumes, these volcanoes provide a snapshot into the dynamic nature of the Earth's mantle and the origin of large-scale mantle features identified through geophysical techniques (Cabral et al., 2013; Cottaar and Lekic, 2016; French and Romanowicz, 2015; Gleeson et al., 2021; Harpp and Weis, 2020; Jackson et al., 2008; Koppers et al., 2021). In addition, ocean island volcanoes can have significant impacts on local populations, infrastructure, and the global climate (Whitty et al., 2020; Wilson et al., 2014). Despite their scientific and societal importance, uncertainties remain regarding the growth and evolution of ocean island volcanoes, and the interplay between magma chemistry/storage and geodynamic setting (e.g., near-ridge vs intraplate; Cleary et al., 2020a; Geist et al., 2014a; Harpp and Geist, 2018a).

The magmatic architecture and volcanic evolution of ocean island volcanoes has traditionally been studied through petrological analysis of erupted volcanic products (e.g., lava and tephra) and analysis of the geodetic and seismic signatures of volcanic unrest (Bagnardi et al., 2013; Bell et al., 2021; Boudoire et al., 2019; Dayton et al., 2023; DeVitre et al., 2023b; Harpp and Geist, 2018; Neal et al., 2019; Stock et al., 2018). These approaches have demonstrated diversity in the characteristics of ocean island volcanoes, with variations in the composition and temperature of the mantle source, and the flux of magma into the lithosphere translating into dramatic differences in the chemistry and magmatic architecture of the volcanic plumbing systems (Baxter et al., 2023; Baxter and Maclennan, 2024; Geist et al., 2014; Gleeson et al., 2020a; Maclennan, 2019). However, important questions remain, including the influence of geodynamic setting on the architecture of magmatic systems and the evolution of magmatic activity in near-ridge settings (Cleary et al., 2020). In addition, with the

growing consensus that magma reservoirs are dominated by crystal-rich, mushy domains, there is increasing recognition that petrological analysis of magmatic cumulates in addition to conventionally-examined erupted material can aid investigation of the chemical, thermal and structural history of ocean island magmatic plumbing systems (Cashman et al., 2017; Gao et al., 2022, 2016; Gleeson et al., 2020a; Horn et al., 2022; Sparks et al., 2019).

At ocean islands, direct access to the cumulate section of the underlying magmatic system is not often available. Instead, snapshots of the underlying mush are provided by cumulate nodules brought to the surface during volcanic eruptions (Clague and Bohrson, 1991; Holness et al., 2019; Lyons et al., 2007). These nodules range from melt-bearing mush fragments to fully solidified xenoliths and typically cover a range of mineralogical assemblages and bulk compositions (Gao et al., 2016; Horn et al., 2022; Stock et al., 2012). In many cases, cumulate xenoliths brought to the surface at post-shield volcanic systems (i.e. downstream of the main region of plume upwelling) record several hundred thousand to millions of years of activity at a single volcanic centre (Clague and Bohrson, 1991; Gao et al., 2016; Lyons et al., 2007). As a result, these cumulate xenoliths not only provide insights into the architecture of mush-dominated magmatic systems beneath ocean island volcanoes, but also the temporal evolution of the volcanoes from which they are collected.

In this study, we utilize recent developments in the analytical capabilities of Energy Dispersive Spectrometry (EDS) to extract quantitative, multi-scale petrological data from cumulate xenoliths in the Galápagos Archipelago. We couple this with depth constraints from thermodynamic models and fluid inclusion barometry to examine the formation and storage history of these nodules. Specifically, we target Isla Floreana, a low melt-flux volcanic system located in the south-eastern Galápagos where ~2.5 Myr of magmatic activity is recorded in the composition of cumulate nodules found in lava and scoria deposits (Harpp et al., 2014; Lyons et al., 2007). We focus on a suite of gabbroic xenoliths that are hypothesized to have formed when the island was located close to the center of plume upwelling (2 - 2.5 Ma; Gleeson et al., 2020a; Lyons et al., 2007a). Our new data,

alongside recent analysis of the present-day Isla Floreana magmatic system (Gleeson et al., 2020a, 2022), is used to evaluate the evolution of an ocean island magmatic system in a near-ridge setting, focusing on the depth of magma storage. Furthermore, comparison of our results to active volcanic centres in the present-day western Galápagos provides insights into the role of geodynamic settings in the construction of magmatic plumbing systems, owing to the migration of the Galápagos mantle plume away from the Galápagos Spreading Centre over the last 5 Myr (Mittelstaedt et al., 2012).

# 2 GEOLOGICAL BACKGROUND

## 2.1 VOLCANIC HISTORY AND TECTONIC SETTING

The Galápagos Archipelago, located ~1000 km off the western coast of Ecuador, represents one of the most volcanically active regions in the world. Magmatic activity in the Galápagos is a consequence of adiabatic decompression melting in a chemically and lithologically heterogeneous mantle plume that is likely ~50-150$^{o}$C hotter than the surrounding ambient mantle (Gibson et al., 2015; Hooft et al., 2003). Seismic tomography indicates that the current centre of plume upwelling is located beneath the islands of Isabela and Fernandina in the western Galápagos (Fig. 1), which are the most volcanically active islands in the archipelago (eruptions occur every 2-3 years on average; Villagómez et al., 2014). However, historical eruptions have also been documented in the eastern and northern Galápagos, on the islands of Santiago (1759, 1904 - 1906), Pinta (1928) and Marchena (1991), and volcanic activity elsewhere in the eastern Galápagos has been shown to be long-lived (Global Volcanism Program, 2013). For example, volcanic activity on the island of San Cristobal in the eastern Galápagos covers a period of more than 2 Myrs, with the most recent eruption dated at ~9 ka (Mahr et al., 2016). Holocene to late Pleistocene eruptions have also been identified at several of the other eastern Galápagos islands, including Isla Floreana on the southern margin of the archipelago (~26 ka; Harpp et al., 2014a).

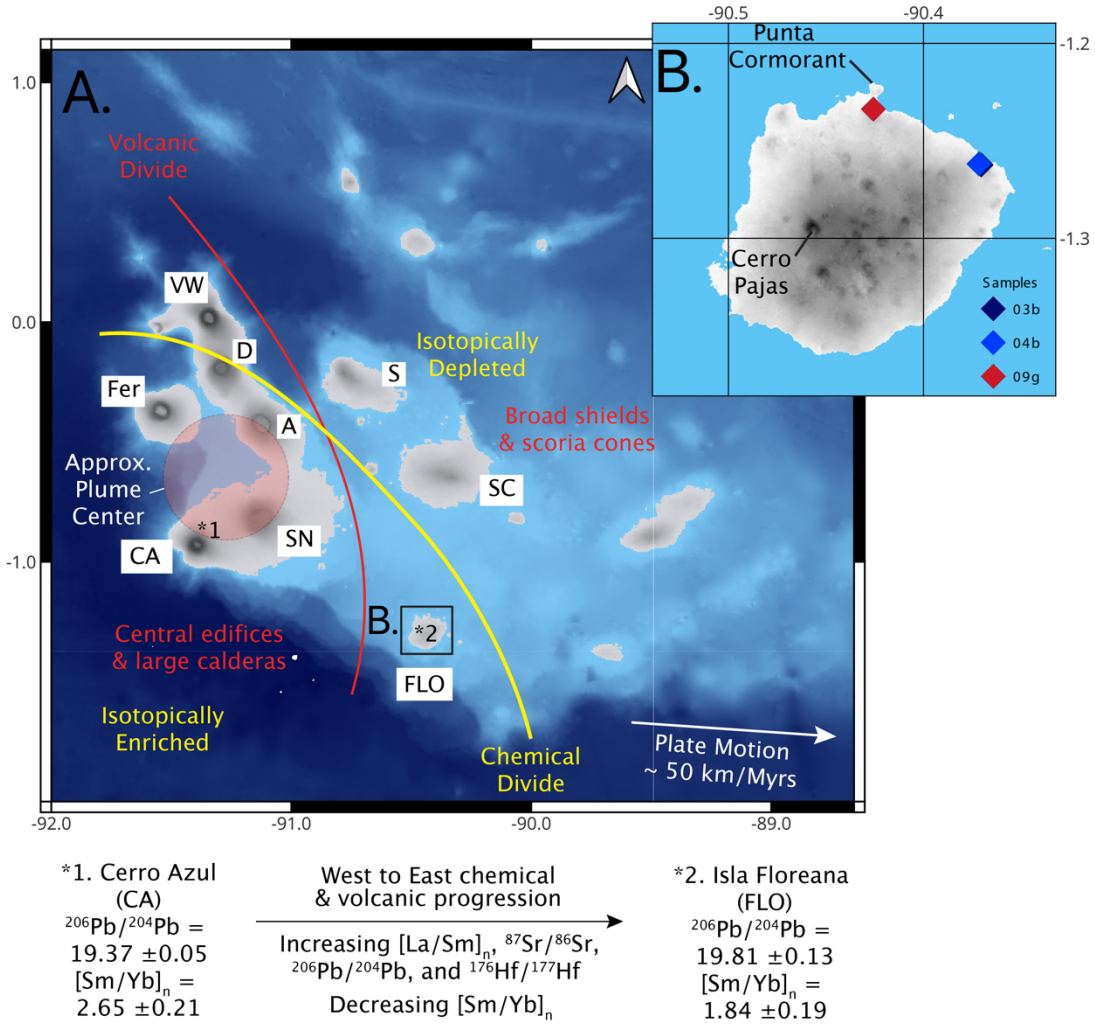


***Figure 1 –*** *Map of the Galápagos Archipelago with the boundaries between different morphological and chemical domains indicated by the red and yellow lines, respectively.* ***A.*** *Topographic and bathymetric map of the Galápagos, data from GEBCO (General Bathymetric Chart of the Oceans). Plate motion estimate taken from Harpp et al. (2014).* ***B.*** *Topographic map of Isla Floreana using high resolution topographic data from the Terra Advanced Spaceborne Thermal Emission and Reflection Radiometer (ASTER) Global Digital Elevation Model (GDEM) Version 3 (ASTGTM) (~30m resolution). Both* ***A.,*** *and* ***B.*** *are created using the World Geodetic Survey (1984) Geographic Coordinate System with an equirectangular projection system. The mean and standard deviation of the $^{206}Pb/^{204}Pb$ and $[Sm/Yb]_n$, ratios, key chemical parameters that can be used to differentiate between the volcanic systems of Cerro Azul and Isla Floreana, are displayed below alongside the key characteristics defining the chemical progression from west to east along the southern margin of the archipelago. VW – Wolf; CA – Cerro Azul, SN – Sierra Negra, FLO – Isla Floreana, Fer – Isla Fernandina, D – Darwin, A – Alcedo, S – Santiago, SC – Santa Cruz.*

118

119 The wide geographic distribution of recent volcanic activity in the Galápagos is likely related to

120 variations in lithospheric thickness across the archipelago (Gibson and Geist, 2010), extensional

121 faulting on the eastern islands (Schwartz et al., 2014), and the near-ridge tectonic setting. The

Galápagos mantle plume is centered roughly 150 – 250 km south of the east-west trending Galápagos Spreading Centre (GSC), a mid-ocean ridge spreading centre separating the Nazca and Cocos tectonic plates. Transfer of material from the Galápagos plume stem to the GSC (whether in the solid or melt phase) has a clear influence on the composition of erupted basalts along the ridge and may contribute to the volcanism observed in the Northern Galápagos Volcanic Province (Gleeson and Gibson, 2021; Mittal and Richards, 2017).

The distance between the Galápagos mantle plume and the GSC has not been constant over the last 5 Myrs. Owing to the eastward motion of the Nazca tectonic plate and the north-east motion of the Cocos plate, the GSC is migrating north, away from the centre of Galápagos plume upwelling (Mittelstaedt et al., 2012; Wilson and Hey, 1995). In fact, ~5 – 12 Myr ago, the Galápagos mantle plume was likely located directly beneath the GSC, in a tectonic situation analogous to modern Iceland (Wilson and Hey, 1995). Since then, the separation distance between the mantle plume and spreading center has increased, with its northward migration punctuated by a series of southward ridge-jumps on the eastern GSC (the most recent of which occurred at ~1 Ma) that resulted in the formation of the Galápagos Transform Fault at ~91°W (Mittelstaedt et al., 2012). As a result, when the eastern Galápagos volcanic islands of Floreana and Santa Cruz were first constructed (at around 2 – 3 Ma) the Galápagos mantle plume was located up to ~100 km closer to the GSC than it is at the present day. The 2-3 Myr old eastern Galápagos and the modern western Galápagos, therefore, formed in different geodynamic settings, which might have had a substantial influence on the characteristics of magma storage (Cleary et al., 2020; Harpp and Geist, 2018).

## 2.2 Variations in volcanic style and morphology

Across the Galápagos Archipelago, there are variations in the style of magmatic activity, which result in key chemical and morphological differences between the various volcanic centres. Broadly, these differences can be used to define two volcanic regions within the Galápagos Archipelago; a western volcanic domain with regular activity focused at 6 central shield volcanoes and an eastern domain

with less frequent eruptions and more spatially-distributed eruptive activity (Harpp and Geist, 2018a; Fig. 1).

The western volcanic region, which encompasses the islands of Isabela and Fernandina, is characterized by the presence of 6 large shield volcanoes and the dissected shield of Volcán Ecuador on the northern margin of Isla Isabela (Geist et al., 2014, 2002). These volcanoes range from ~1100 m to ~1700 m in height and are characterized by the presence of a large central caldera and an inverted soup-bowl morphology (Bernard et al., 2019; Geist et al., 2005; Naumann and Geist, 2000; Fig. 1c). The major element, trace element, and isotopic variations observed in erupted material at each of the western volcanic centers is typically relatively narrow (compared to the eastern Galápagos islands), indicating that mantle-derived magmas are efficiently mixed in their magmatic systems and buffered over a narrow range of temperatures by the regular input of new, mantle-derived magma into the system (Geist et al., 2014, 1995). Recent barometric work, using both petrological and geophysical monitoring data, indicates that the bulk of magma storage occurs in the mid-to-lower crust (7-15 km; Higgins and Stock, 2024; Stock et al., 2018), with a secondary magma storage region present at shallow depths beneath most of the western Galápagos shields (Bagnardi et al., 2013).

The eastern volcanic region encompasses the islands of Santa Cruz, Santa Fe, Floreana, Española, San Cristóbal and Santiago (Harpp and Geist, 2018). These islands are characterized by shallow slope gradients, distributed volcanism, monogenetic scoria cones, and lack of large central edifices (Fig. 1d). There is little to no evidence to indicate the presence of buried calderas beneath the surface of any of the eastern Galápagos islands, which has been presented as evidence that these systems are unlikely to represent the late-stage evolution of a system analogous to the current western Galápagos shield volcanoes (Cleary et al., 2020). Unlike the western Galápagos shield volcanoes, there is a substantial major, trace element and isotopic heterogeneity in the erupted products of each eastern volcanic island (Bow and Geist, 1992; Harpp et al., 2014; Harpp and Geist, 2018). This

heterogeneity has been hypothesized to occur due to the lower flux of mantle-derived melts into these islands (relative to the western shields), which is insufficient to form a centralized, thermally buffered mush system capable of homogenizing chemical variations from incoming mantle melts (Gleeson et al., 2020a; Harpp and Geist, 2018). Instead, the magmatic systems are likely ephemeral, poorly connected, and are characterized by a range of melt temperatures and compositions. Melt inclusion and clinopyroxene-based barometry from Isla Floreana, which shows the greatest degree of compositional heterogeneity anywhere in the Galápagos, indicates that magma storage beneath the eastern Galápagos islands is substantially deeper than beneath the western Galápagos shield volcanoes and likely exceeds the depth of the Moho (~16 km; Gleeson et al., 2020a, 2022).

## 2.3 GALÁPAGOS PLUME HETEROGENEITY

The wide distribution of Holocene and late Pleistocene volcanism in the Galápagos has been used to unravel the compositional heterogeneity in the upwelling mantle plume (Geist et al., 1988; White et al., 1993). Several different mantle components have been identified or proposed, including enriched mantle reservoirs with highly radiogenic Pb and Sr isotope ratios (most prominently seen on Isla Floreana; Harpp et al., 2014a; White et al., 1993), primordial mantle domains retaining unradiogenic He isotope signatures ($^3He/^4He$ up to ~29 $R/R_A$; Isla Fernandina; Kurz et al., 2009; Kurz and Geist, 1999), and a depleted component whose origin (intrinsic plume material vs entrained upper mantle) remains debated (Gibson et al., 2012; Harpp and White, 2001; Hoernle et al., 2000).

Overall, at least 4 chemically and/or lithologically distinct components have been proposed (Geist et al., 1988; Gleeson et al., 2021, 2020b; Gleeson and Gibson, 2019; Harpp and White, 2001; Vidito et al., 2013). These components have a complex spatial arrangement that is long-lived on timescales of several 10s of Myrs (Hoernle et al., 2000). At the most basic level, the Galápagos can be split into an isotopically depleted north-eastern domain – where basalts have isotopic signatures that are similar to the global MORB field – and an isotopically enriched south-western domain (Gleeson et al., 2021; Harpp and Weis, 2020). The boundary separating these two domains is sub-parallel to the boundary

197 separating the western and eastern volcanic regions (yellow line, Fig. 1a). As a result, Volcán Wolf on
198 northern Isabela falls within the western volcanic region (Harpp and Geist, 2018), but is chemically
199 more closely related to volcanic systems in the north-eastern Galápagos (Harpp and Weis, 2020).
200 Conversely, Isla Floreana in the southern Galápagos forms part of the eastern volcanic region (gentle
201 slopes and an abundance of monogenetic scoria cones) yet displays the most radiogenic Sr and Pb
202 isotope signatures of any volcanic island in the Galápagos and is thus associated with the chemically
203 enriched south-western domain (Gleeson et al., 2020a; Harpp et al., 2014; Harpp and Weis, 2020).

204 The chemical asymmetry of the Galápagos Archipelago is similar to the presence of the Loa and Kea
205 geochemical trends in Hawai'i (Harpp and Weis, 2020). The main difference between the two
206 systems is that the chemical asymmetry in the Galápagos is not orientated parallel to the direction
207 of plate motion. As this chemical asymmetry in the Galápagos is long-lived on timescales >15 Myrs
208 (Hoernle et al., 2000), the isotopic and trace element composition of erupted material at the surface
209 of each individual volcanic system will change through time as the Nazca Plate moves east-southeast
210 above the mantle plume. The anticipated chemical evolution of any particular volcanic system is
211 controlled by the position of the volcano with respect to latitude; for example, in a central strip
212 spanning west to east across the archipelago (e.g., Isla Fernandina, Volcán Alcedo, Isla Pinzón, and
213 Isla Santa Cruz) the mantle source region will move across the boundary separating the enriched
214 south-western domain and the depleted north-eastern domain leading to a temporal progression
215 from enriched to depleted isotopic signatures (Wilson et al., 2022). In contrast, along the southern
216 margin of the Galápagos platform (Volcán Cerro Azul, Volcán Sierra Negra, and Isla Floreana) the
217 west-to-east progression is characterized by variations in the degree of enrichment and differences
218 in key trace element and isotopic parameters (Fig. 1). Specifically, Isla Floreana basalts contain more
219 radiogenic Sr and Pb isotope signatures relative to Volcán Cerro Azul and Volcán Sierra Negra, as well
220 as offsets in many trace element ratios (e.g., $[Sm/Yb]_n$, where n indicates normalization to the
221 primitive mantle estimate of Sun and McDonough, 1989; Fig. 1; Harpp et al., 2014a). Consequently,
222 volcanic evolution over millions of years at the southern margin of the Galápagos platform – the

region targeted in this study – should be associated with a systematic shift to more enriched isotopic signatures and concave Rare Earth Element patterns (high $[La/Sm]_n$ but low $[Sm/Yb]_n$ ratios).

# 3 METHODS

The gabbroic xenoliths analysed in this study represent 2 – 5 cm diameter nodules collected from scoria cones in the north-east corner of Isla Floreana (17MMSG03b, 17MMSG04b; hereafter 03b and 4b) and small fragments (exposed areas of ~0.5-3 $cm^2$) found in the core of a blocky lava flow near Punta Cormorant on Isla Floreana's northern coast (17MMSG09; Fig. 1). Prior to analysis, all samples were cut into small blocks <1 cm thick with exposed areas ranging from <0.5 – 5 $cm^2$. Lava samples containing small gabbroic fragments (17MMSG09; hereafter 09g1, 09g2, and 09g3) were cut to maximize the surface exposure of the gabbro. The cut samples were ground down using various grades of silicon carbide grit and then prepared for analysis by polishing the exposed surface areas with a 1 µm diamond suspension.

## 3.1 FEG-SEM ANALYSIS

The polished gabbroic blocks were carbon coated to a thickness of ~10 - 13 nm and analyzed using both the Zeiss Sigma HD Field Emission Gun Scanning Electron Microscope (FEG-SEM) at Cardiff University School of Earth and Environmental Science and the JEOL JSM IT800HL FEG-SEM at the University of California, Berkeley. Analyses were performed over a range of length-scales, from whole-sample compositional maps to high-precision analysis of major and minor elements in linescans and individual point analyses.

### 3.1.1 Quantitative compositional mapping

Quantitative compositional maps of the exposed gabbroic regions were produced for all samples using the Cardiff Zeiss Sigma HD FEG-SEM and two Oxford Instruments X-Max 150 Energy Dispersive Spectrometers. Maps were created with a pixel size of 25 X 25 µm using a beam current of ~1.1 nA

(determined through the choice of aperture size – 60 µm) and an accelerating voltage of 20 kV. To reduce background noise and increase spectral resolution, the signal process time was set to the AZtec preset 3 (~2 microseconds per X-ray). The dwell time was 0.05 seconds for each pixel, and a quantitative chemical composition was generated using a predefined calibration file (determined through analysis of mineral and metal standards; see Supplementary Material), and a XPP matrix correction routine (implemented through the associated AZtec software).

To assess the accuracy and precision of our map data, 15 mineral standards were mapped within the same analytical session as our gabbroic xenoliths. The estimated concentrations of all elements >2 wt% are typically within 2% of the published standard value. Relative offsets between predicted and published values for oxides with lower concentrations are larger, in part owing to uncertainties in the published standard compositions and the presence of minor element heterogeneity within these samples. The analytical precision for each pixel was low (relative 1σ precision of >39% for Na in Diopside – Astimex standard), but is substantially improved by binning multiple pixels. For example, generating 1000 compositions of each mapped standard by averaging the composition of 25 pixels in a randomly selected 5-by-5 grid indicates that the analytical precision of Na in Diopside (concentration of 0.3 wt%) in this binned region is ~7.5% (calculated as the relative 1σ value). For elements present in concentrations > 1 wt% (e.g., Ca in Diopside), the analytical precision for each pixel is between 10% and 2%, improving to 3% to <1% for a 5-by-5 pixel region.

### 3.1.2 Map Data processing

Quantitative EDS mapping provides a wealth of information for each of the gabbroic xenoliths. Using this data, we can identify the major phases within a sample, constrain the compositional distribution of each phase, and determine the bulk sample composition. We used the Python3 package mineralML to identify the major phases present in each sample (Shi et al., 2023). mineralML uses Bayesian neural networks, trained on over 86,000 analyses of 17 minerals (data compiled from literature) and validated upon ~1 million analyses (data from EarthChem, GEOROC, and LEPR), to

predict the mineral phase for each chemical composition provided (i.e., every map pixel). mineralML also supplies the probability of classification for each analysis; we filter out pixels where the predicted probability is less than 0.6. The primary effect of this filtering step is the removal of pixels whose analytical totals are < 90 wt%, typically representing cracks and/or holes where high-quality analyses were not possible.

Once the mineral abundances and mean compositions have been determined (Fig. 2; Supplementary Information) a 'bulk-rock' composition can also be calculated by determining the weighted average of all pixels assigned a phase by mineralML:

$$C = \frac{\sum_{i=0}^{n} C_i \times \rho_i}{\sum_{i=0}^{n} \rho_i}$$

Where $C$ represents the bulk concentration of the chosen oxide; $C_i$ indicates the measured concentration in pixel $i$; and $\rho_i$ represents the estimated density of the mineral located at each pixel (based on the identified mineral phase; see Supplementary Material). To estimate the uncertainty associated with these bulk concentration estimates, we generate 200 possible compositions for samples 03b and 04b where an area accounting for >33% of the total sample were randomly selected for each calculation. In general, the uncertainties estimated by this method are very low, typically less than 2% (relative 1σ variation) for most oxides.

We consider the compositions estimated from samples 03b and 04b to be representative of their bulk-rock compositions. This is supported by the similarity between the SEM-derived bulk-rock estimates presented here and the bulk-composition of other Isla Floreana gabbros previously determined by XRF analysis (Lyons et al., 2007; see Supplementary Material). Furthermore, our error analysis indicates that samples 03b and 04b are homogeneous on scales smaller than the analyzed areas (see Supplementary Material). Nevertheless, we caution that the composition of samples 09g1, 09g2, and 09g3 must be treated with care, as these samples are characterized by relatively

small areas (<0.5 $cm^2$), and the presence of heterogeneity on scales smaller than the pixel resolution of our large-scale maps (see below).

### 3.1.3 Qualitative, high-resolution chemical mapping

To supplement the large-scale maps and provide more information about any small-scale heterogeneity within each sample, qualitative chemical maps of orthopyroxene-clinopyroxene grain boundaries were also collected on the Cardiff Zeiss Sigma HD FEG-SEM. No standards were mapped alongside these high-resolution maps and so quantitative chemical compositions were not calculated. Each map was collected under identical analytical conditions to the large-scale maps, but with a pixel size of 1.5 X 1.5 µm (Fig. 3).

### 3.1.4 Linescans

In addition to the qualitative maps of clinopyroxene-orthopyroxene grain boundaries, EDS linescans were collected, using the Zeiss Sigma HD FEG-SEM and 2 X-Max EDS detectors, to provide quantitative chemical information of these regions. Five passes, with a dwell time of 3 seconds per spot on each pass, were carried out along each line (ranging from 140 to 220 µm in length with a spatial resolution of 1.5 µm). Data collection was performed using a 1.1 nA beam current, a 20 kV accelerating voltage, and a process time of 3 (AZtec preset value). Quantification was performed using the same calibration file that was used for individual spot analyses (see Supplementary File), which was constructed using point analyses of a range of mineral and metal standards. To check the accuracy and precision of analyses, linescans were also performed on two clinopyroxene standards. Data from these standards indicate that the precision of analyses ranges from ~5% (1σ relative standard deviation) for minor components such as $Al_2O_3$ and $Na_2O$ (0.6 wt% and 0.41 wt% respectively) to <0.5% (1σ relative standard deviation) for $SiO_2$ and CaO. Measured compositions of the secondary standard materials are typically within 1% of the preferred standard values.

### 3.1.5 Point Analyses

In addition to compositional maps and linescans, we perform high-precision point analyses of clinopyroxene, orthopyroxene and plagioclase crystals in all the Isla Floreana gabbros. The major and minor element composition of pyroxene crystals was determined through EDS analysis (using two X-Max 150 detectors) on the Cardiff Zeiss Sigma HD FEG-SEM. For these analyses, the beam was rastered over an area of 1 µm by 1.5 µm and analyses were performed using a 1.1 nA beam current and a 20 kV accelerating voltage. As with the compositional maps and EDS linescans, the process time was set as the AZtec preset 3, and a 15 second live dwell time was used for all EDS point analyses. The EDS calibration file was constructed via analyses of appropriate mineral and metal standards (see supplementary file).

The composition of plagioclase crystals hosted in the Isla Floreana gabbros was determined through EDS-WDS (Wavelength Dispersive Spectrometry) analysis on the JEOL JSM IT800HL FEG-SEM at UC Berkeley. The JEOL FEG-SEM provides a greater range in possible beam conditions than the Zeiss SigmaHD FEG-SEM in Cardiff, providing access to higher beam currents (~100 nA) suitable for minor element analysis by WDS. The concentration of most major and minor elements in the plagioclase crystals (i.e., $SiO_2$, $Al_2O_3$, $FeO_t$, CaO, $Na_2O$, and $K_2O$) was determined through EDS analysis using a single Ultim-Max 100 $mm^2$ detector. During analysis the beam was rastered over a 1-by-1.5 µm area using a beam current of 2 nA and an accelerating voltage of 20kV. The process time for these analyses was set at the Aztec process time 5 (~10 microseconds). Following EDS analyses the beam current was increased to 100 nA and the concentration of MgO (and $K_2O$ in some crystals), at the location of each EDS analysis, was determined via WDS using an Oxford Instruments Wave detector. Counts of Mg were collected for 40 seconds on peak using a TAP crystal, and background counts were collected for 20 seconds on either side of the peak. When measured, counts of K were also collected with a 40 second peak count time and 2*20 second background count time using a PET crystal. Analysis of MgO and $K_2O$ via WDS were calibrated through analysis (at 10nA) of a synthetic Forsterite standard and an Orthoclase standard, respectively.

Analyses of secondary standard materials, including clinopyroxene, plagioclase and garnet, were performed at regular intervals (~2 – 3 hours) to determine the accuracy and precision of analyses (see Supplement for full list of standard sources). These data demonstrate that our EDS analysis is typically accurate to within 1% for high concentration elements (i.e., > 2 wt%) within the secondary standard materials. Outputted error estimates (determined by the Aztec software), and the variability in the estimated composition of secondary standard materials, indicates that the 1σ relative precision of all EDS analyses is <0.5 - 1 % for elements present in high concentrations (> 2 wt%) and increases to ~10-15% for analyses of minor elements (0.2 – 1 wt%). The relative 1σ precision of WDS analyses is estimated to be <3% for MgO in plagioclase (at ~0.12 wt%) and <1.5% for $K_2O$ (at 0.12 wt%). For all analyses we consider the detection limit to equivalent to 3σ.

## 3.2 Laser Ablation Inductively Coupled Plasma Mass Spectrometry

Clinopyroxene trace element abundances were determined using an ASI RESOlution 193 nm Laser Ablation system coupled to an Agilent 8900 triple quadrupole ICP-MS hosted in the CELTIC laboratory at Cardiff University. Data was collected for 2 minutes per analysis, including a 20 second delay prior to laser initiation, 60 seconds of data collection with the laser active, and a 40 second wash-out period. A 4.5 J/cm$^2$ fluence, a 10 Hz repetition rate, and an 80 μm spot size was used for all analyses.

Data processing was carried out using the LaserTram software (Lubbers et al., 2021) with BCR-2g as the calibration standard. $^{43}$Ca was used as the internal standard for all analyses and the accuracy of analysis was tracked through regular measurements of multiple secondary standards (Jochum et al., 2005). These analyses indicate that all elements reported here return values within ~5% of the published standard values. The relative 1σ precision of analysis is typically <2 – 3% for most elements, although it is important to note that the concentration of most trace elements in the clinopyroxene unknowns are substantially lower than those in the glass secondary standards. Repeat analysis of clinopyroxene cores from our gabbroic samples indicates that the relative 1σ analytical

precision is <5% for all light and middle Rare Earth Elements (REEs), increasing to ~8 – 10% for the heavy REEs.

## 3.3 Fluid Inclusion Analysis

The density of $CO_2$ in fluid inclusions (FIs) can provide a powerful barometer in $CO_2$-dominated magmatic systems as $CO_2$ density is strongly related to the pressure and relatively insensitive to temperature (Hansteen and Klügel, 2008; Wieser et al., 2025). We quantify $CO_2$ densities in clinopyroxene and plagioclase-hosted FIs using microthermometry and calibrated Raman Spectroscopy following the methods of DeVitre and Wieser (2024). To isolate crystals containing FIs we carefully cut a small section (~5 mm x 5 mm x 1mm) of samples 03b and 04b following completion of EDS chemical analysis. These sections were then crushed and individual clinopyroxene and plagioclase crystals were picked from the crushed material and examined for the presence of FIs. These crystals were mounted in crystal bond and ground down using 1200 and 2500 grade silicon carbide paper. Crystals with visible fluid inclusions were then polished using 10000 grade paper and 1μm 3M polishing paper before they were flipped and polished on the other side. Once a thin wafer (< 300 μm) had been prepared with FIs clearly visible within ~100 μm of the surface, crystals were extracted from the crystal bond using a hot plate and Acetone and placed into separate vials. We primarily target fluid inclusions with no visible evidence of decrepitation. Most fluid inclusions in sample 04b appear as isolated inclusions with no clear connection to trails or fracture planes and are thus labelled as 'apparent primary fluid inclusions'. Many of the inclusions measured in 03b are interpreted as secondary as they are located in trails (see Supplementary Material for full textural characterization).

Heating and cooling experiments were performed on a Linkam THMSG600 heating and freezing stage at UC Berkeley. Temperature was calibrated using the melting temperature of a pure $H_2O$ fluid inclusion (0°C) and the melting temperature of $CO_2$ (-56.6 °C) in a $H_2O$-$CO_2$ fluid inclusion. We recorded the melting point/interval and homogenization temperature of each fluid inclusion with a

precision of ~+/- 0.1°C using the cycling technique (Hansteen and Klügel, 2008). Homogenization temperatures were converted into $CO_2$ densities using equations 3.14 and 3.15 of Span and Wagner (1996), implemented in DiadFit (Wieser and DeVitre, 2024).

We also analyzed all fluid inclusions from sample 04b by calibrated Raman spectroscopy, following the methods of DeVitre and Wieser (2024). In summary, we utilize a WiTec Alpha 300R Raman spectrometer at the Department of Earth and Planetary Sciences at the UC Berkeley, with a green 532.046 nm laser and an 1800 grating. Accounting for the small and variable size of fluid inclusions, we use 50-100X objectives for analysis. Laser powers of 6 mW were used throughout to minimize the effects of laser heating (DeVitre et al., 2023a; Hagiwara et al., 2019). Instrument drift was corrected using the ~1117 and 1447 $cm^{-1}$ Ne emission lines (see DeVitre and Wieser, 2024; Lamadrid et al., 2017). All peak fitting was performed in the Python3 tool DiadFit (Wieser and DeVitre, 2024). The $CO_2$ densities determined through Raman Spectroscopy and Microthermometry are typically equivalent within analytical uncertainties, consistent with prior work (DeVitre and Wieser, 2024). To check for the presence of other gaseous species that may have contributed to the derivation in observed melting temperatures from the theorectical melting point of $CO_2$ (e.g., CO, $CH_4$, $N_2$), we analyzed fluid inclusion covering the complete range of observed melting temperatures at higher laser power (49 mW) and a 300 grating, resulting in higher signal strength and a wider range of wavenumbers recorded in a single acquisition.

To calculate pressure from the density of $CO_2$ in a fluid inclusion using the $CO_2$ equation of state, an estimate of the entrapment temperature is required. Fluid inclusion pressures will likely relax via diffusion creep during prolonged storage and cooling of the system (Hansteen and Klügel, 2008; Wanamaker and Evans, 1989) to equilibrate internal and external pressures. Consequently, under the assumption of full re-equilibration, we use the temperatures derived from clinopyroxene-orthopyroxene thermobarometry and Mg-in-plagioclase thermometry to invert the measured homogenization temperatures and calculated $CO_2$ densities into pressure. These calculations were

performed using the CO2 EOS of Span and Wagner (1996), implemented in CoolProp (Bell et al., 2014), and accessed through DiadFit (Wieser and DeVitre, 2024). Further calculations were performed to investigate the potential influence of $H_2O$, He, and Ar on the calculated pressures (see Supplementary Material).

# 4 Results & Discussion

## 4.1 Mineralogical & chemical signatures in the context of Galápagos Volcanism

All gabbro samples considered here display a high degree of textural equilibrium, with 120$^o$ grain boundary angles at plagioclase triple junctions and a narrow range in grain sizes (mean size ~500 μm; Gleeson et al., 2020a). While these textures restrict petrographic characterization of the xenoliths based on their original igneous texture (i.e., forming through mechanical settling vs. in situ crystallization) estimated bulk-rock compositions derived from the EDS maps are consistent with that expected from crystal fractionation (i.e., the residual solid assemblage), with density sorted settling of plagioclase and mafic mineral phases in a liquid-rich reservoir resulting in the observed compositional variations (see Supplementary Information).

EDS maps and associated phase predictions from mineralML also reveal a consistent mineralogical signature across our Isla Floreana gabbros (2 pyroxene + plagioclase + spinel) with no residual melt. All samples are dominated by plagioclase (32 – 69%) and clinopyroxene (22 – 49%), with lower proportions of orthopyroxene (1 – 16%) and an Al-rich spinel (typically < 5%; Fig. 2). No olivine is identified in samples 03b and 04b, with only a small number of olivine pixels (associated with orthopyroxene rims) in samples 09g1 – 3 (Fig. 2, 3). High-resolution chemical maps of the orthopyroxene grain boundaries confirm the presence of these inferred olivine pixels, revealing small crystals of olivine forming in orthopyroxene breakdown rims (Fig. 3). Consequently, the presence of minor olivine in samples 09g1-3 is unlikely to represent the equilibrium mineral

441 assemblage, indicating that all 5 samples considered here display essentially the same mineralogy.

442 This is consistent with the mineralogy reported for gabbroic xenoliths collected from Isla Floreana by

443 Lyons et al. (2007a), with substantial olivine only reported in samples with high MgO contents (> 20

444 wt%).

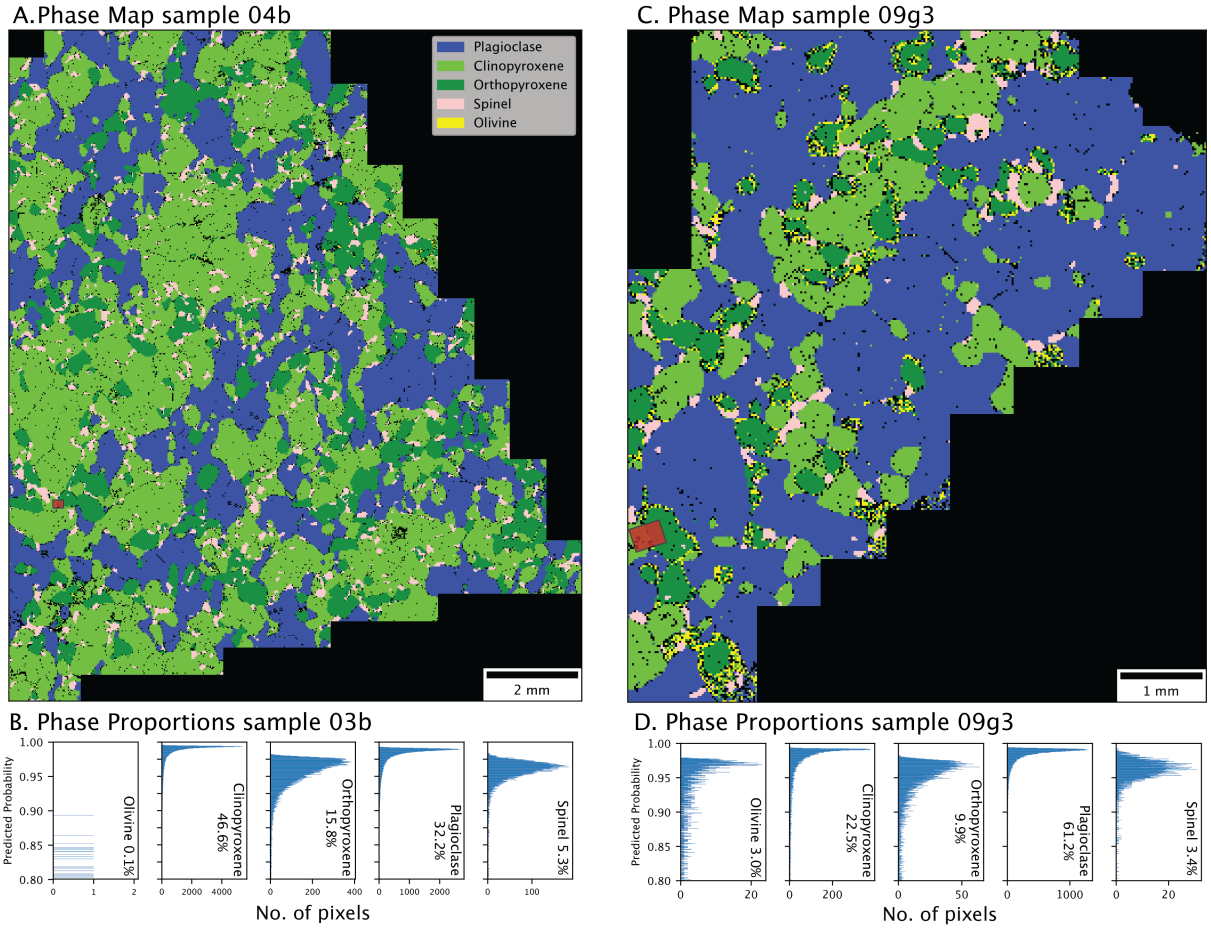


***Figure 2 –*** *Phase maps and associated modal abundances in characteristic gabbro samples.* ***A.*** *Phase map of sample 03b. This sample shows a clear 4 phase mineralogy, with no olivine present.* ***B.*** *Phase proportions, determined by mineralML (Shi et al. 2023), with the associated predicted probability for each analysis shown in the histograms. These confirm the absence of olivine in sample 03b.* ***C.*** *Phase map of sample 09g3. Pixels identified as olivine by MineralML can be seen in the rim regions of orthopyroxene grains.* ***D.*** *Phase proportions confirm the presence of olivine in this sample. Red boxes in panels* ***A.*** *and* ***C.*** *show the areas displayed in Fig. 3.*

445

446 The abundant plagioclase in our samples is, however, at odds with many petrographic and

447 geochemical characteristics of Isla Floreana lavas. Plagioclase is absent or only present as a minor

448 phase in most lavas exposed at the surface of Isla Floreana (< 1.5 Ma), and may represent

449 disaggregated xenolith material where it does occur (Gleeson et al., 2020a; Harpp et al., 2014).

Similarly, most lavas on Isla Floreana are olivine-phyric, a phase conspicuously absent from our xenolith samples. Furthermore, erupted lava whole-rock major element trends – such as negatively correlated $Al_2O_3$ vs MgO contents – indicate that erupted lava compositions are controlled by crystallization or addition of olivine and minor clinopyroxene, with plagioclase playing little to no role in the evolution of the Isla Floreana magmas (Harpp et al., 2014).

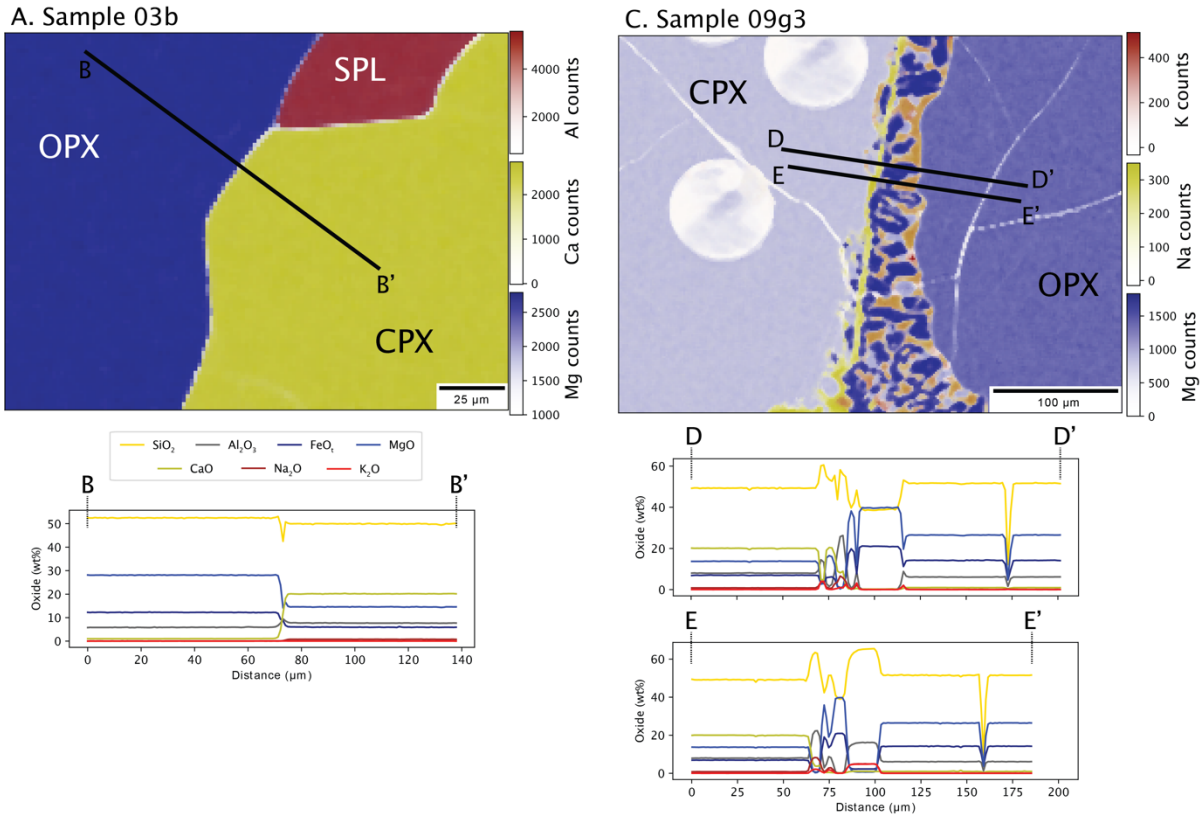


***Figure 3 –*** *High-resolution EDS maps of clinopyroxene-orthopyroxene (cpx-opx) grain boundaries.* ***A.*** *EDS map of sample 03b demonstrates a sharp cpx-opx boundary without any breakdown features.* ***B.*** *An EDS linescan across this boundary reveals an absence of chemical zoning in the region near the cpx-opx boundary.* ***C.*** *EDS maps of sample 09g3 demonstrates the presence of an opx-cpx boundary characterised by the presence of an Mg-rich phase and an Si, K, and Na-rich phase.* ***D.&E.*** *Linescans across this boundary reveal the presence of olivine (Mg-rich) and silicate melt (Si-rich) in the rim zone separating the clinopyroxene and orthopyroxene crystals.*

The differences between the Isla Floreana gabbros and the recent Isla Floreana magmatic system (detailed by Gleeson et al. (2022, 2020a)) extend beyond the mineralogy of these xenoliths. The composition of the clinopyroxene crystals found in the Isla Floreana gabbros contrasts with the composition of crystals collected from scoria cones and lava flows that are not associated with any xenolith group (termed ‘autocrysts’ by Gleeson et al., 2020a). The gabbroic clinopyroxenes are

460 characterized by relatively low Mg# (where Mg# = Mg/(Mg+Fe) molar), with crystals in samples

461 09g1-3 averaging Mg# ~0.77, slightly lower than those measured in samples 04b (~0.79) and 03b

462 (~0.81; Fig. 4). By contrast, autocrystic clinopyroxenes measured in the Isla Floreana lavas typically

463 have Mg# between 0.84 and 0.90 (Fig. 4).

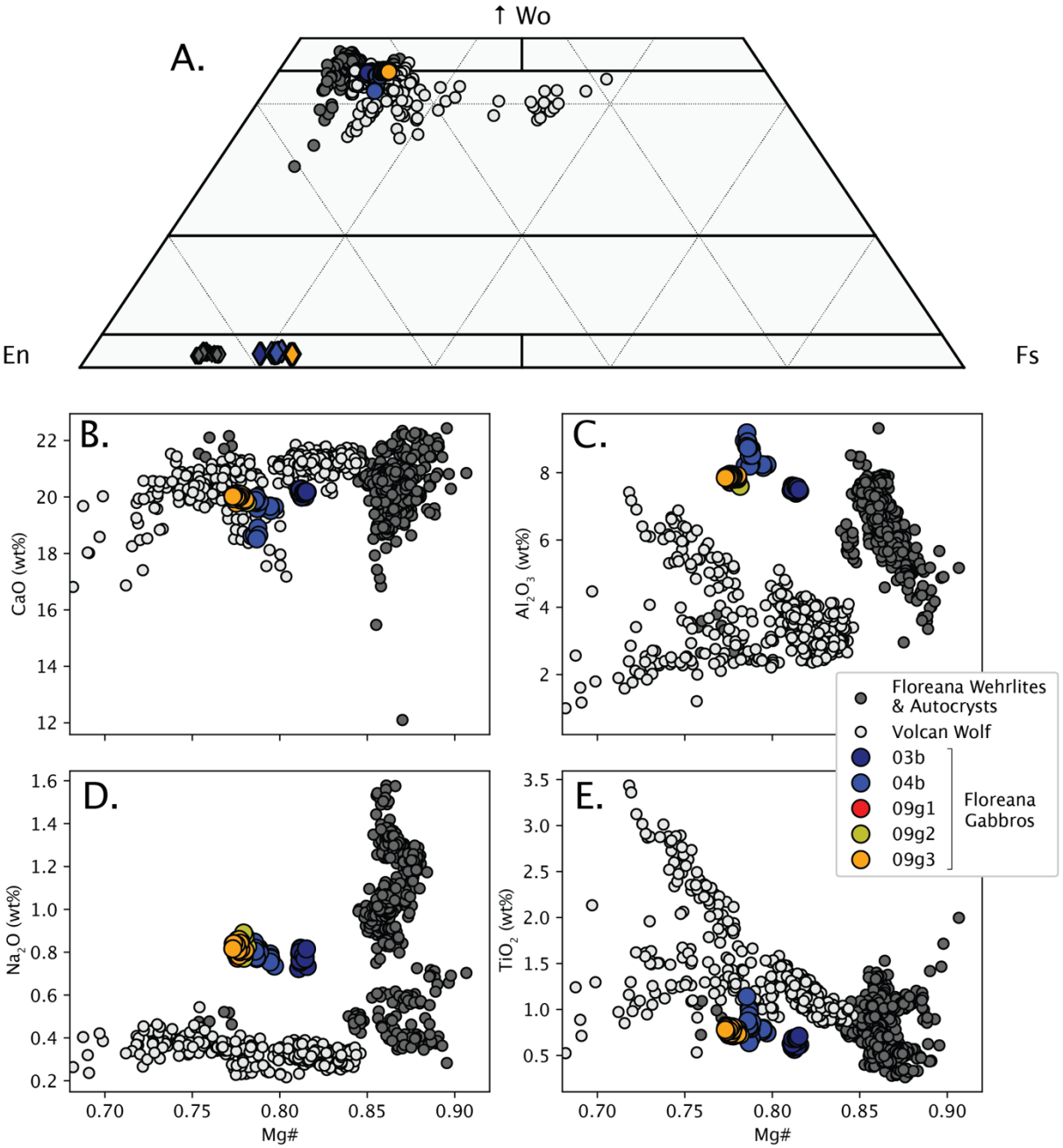


***Figure 4 –*** *Clinopyroxene (and orthopyroxene) compositions from the Isla Floreana Gabbros compared against clinopyroxene data from Volcán Wolf (Stock et al. 2018), chosen as a 'characteristic' western Galápagos volcanic system, and pyroxene analyses from wehrlite xenoliths and clinopyroxene autocrysts from Isla Floreana based on the classification of Gleeson et al. (2020a).* ***A.*** *Pyroxene quadrilateral displaying the narrow range of compositions measured in the Isla Floreana gabbros relative to other datasets from the Galápagos Archipelago (made in Thermobar; Wieser et al. 2022).* ***B. – E.*** *Mg# vs CaO, $Al_2O_3$, $Na_2O$, and $TiO_2$ respectively.*

In addition, the trace element signature of the gabbroic clinopyroxene crystals are distinct from those measured in other clinopyroxene groups from Isla Floreana (autocrysts, wehrlite and dunite xenoliths; Gleeson et al., 2020a). The primitive mantle normalized REE patterns of the gabbro clinopyroxenes display a positive light-to-middle REE slope, and a negative slope from the middle to heavy REEs (Fig. 5). This pattern is expressed by the high $[Sm/Yb]_n$ ratios measured in the gabbroic clinopyroxenes (>1.7; where 'n' symbolizes normalization to the primitive mantle values of Sun and McDonough, 1989), which are significantly higher than those measured in the other clinopyroxene groups (1 – 1.5; Fig. 5b,c). When converted into equilibrium melt compositions, using the parameterization of Sun and Liang (2012), our new clinopyroxene data exceed the measured $[Sm/Yb]_n$ ratio of any basalt erupted on the surface of Isla Floreana (Fig. 6). Taken together, these data indicate that the gabbroic xenoliths found in scoria and lava deposits on Isla Floreana are

475 unlikely to have formed from crystallization of their carrier liquid, or any magma composition that is
476 related to basaltic compositions currently exposed on the surface of the island.

477 Prior work has revealed that the present style of volcanism on Isla Floreana (i.e., infrequent eruption
478 of olivine-physic basalts) has lasted for around 1 – 1.5 Myrs (Harpp et al., 2014). As the gabbro
479 xenoliths show no clear geochemical relationship to this 'recent' period of volcanism on Isla
480 Floreana, it is necessary to consider other possible origins. For example, at other ocean island
481 volcanoes worldwide (e.g., Hualalai, Hawai'i; Gao et al., 2022), trace element and isotopic signatures
482 have been used to identify the presence of gabbro xenoliths originating from the underlying oceanic
483 crust. However, xenoliths of gabbroic cumulates associated with the Nazca oceanic crust (that are
484 unrelated to Galapagos plume volcanism) would be expected to have very different chemical and

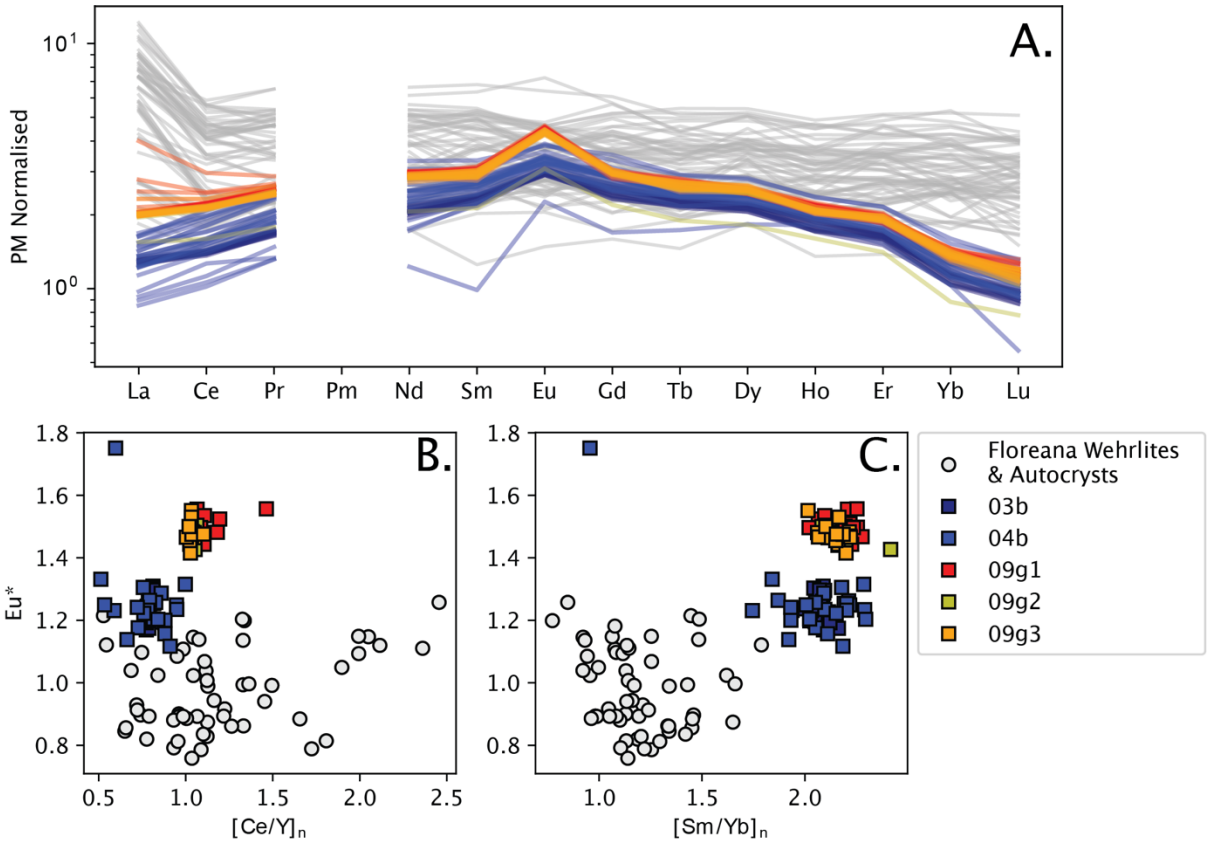


***Figure 5 –*** *Trace element composition of Isla Floreana clinopyroxenes.* ***A.*** *REE diagram of clinopyroxenes from the Isla Floreana gabbros (colors) and published data from wehrlite xenoliths and clinopyroxene autocrysts (Gleeson et al. 2020a), normalized using the primitive mantle (PM) estimate of Sun and McDonough (1989).* ***B.*** *Eu anomaly (Eu*) vs $[Ce/Y]_n$, which is used to demonstrate the degree of incompatible trace element enrichment in each sample.* ***C.*** *The $[Sm/Yb]_n$ content of the gabbroic clinopyroxenes is distinct from crystals measured in the wehrlite xenoliths.*

485 mineralogical characteristics to those observed in the Isla Floreana gabbros. Most importantly, the
486 clinopyroxene trace element (e.g., high $[La/Yb]_n$ and $[Sm/Yb]_n$ ratios) and radiogenic isotope
487 systematics (from Lyons et al. 2007) confirm that the Isla Floreana gabbros must be formed by
488 magmas generated at high pressure in the Galapagos mantle plume and cannot be associated with
489 periods of ridge volcanism.

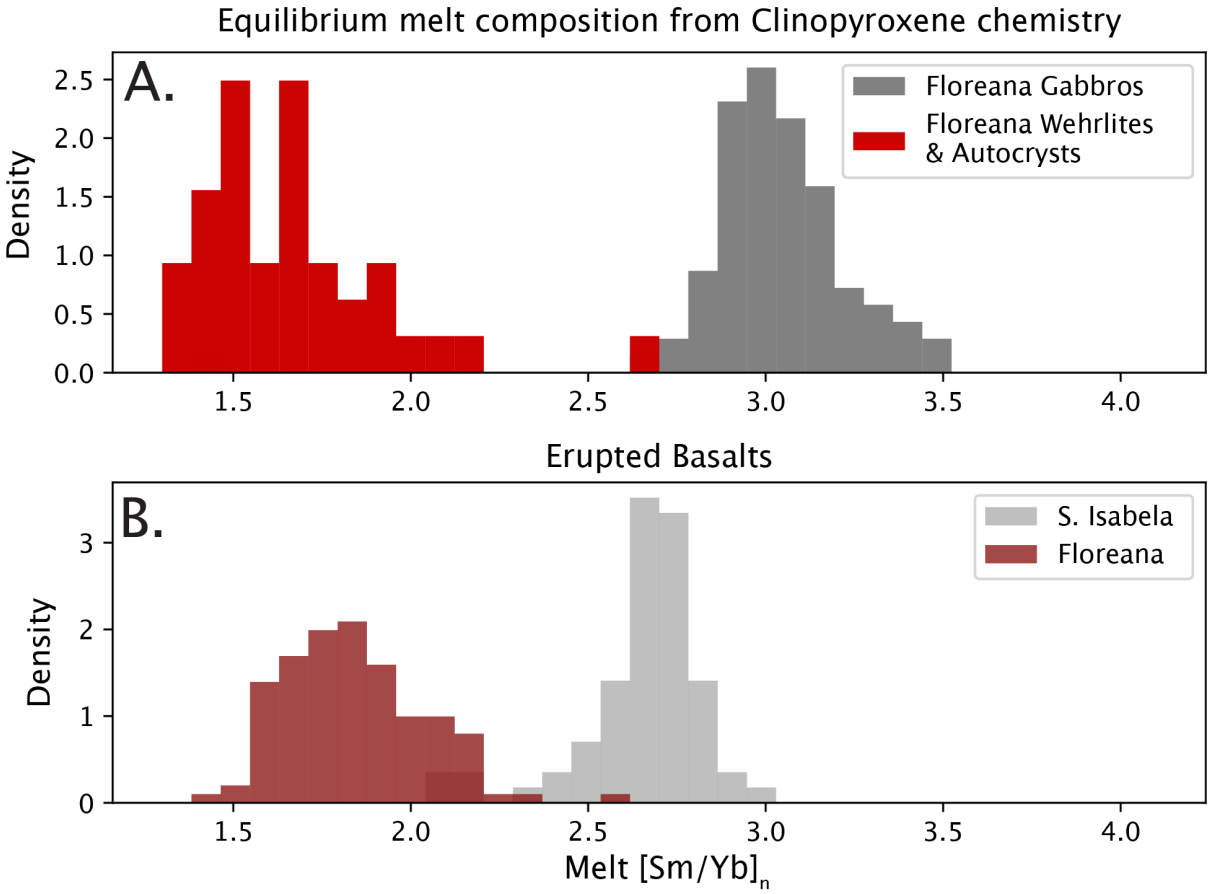


***Figure 6 –*** *Equilibrium melt $[Sm/Yb]_n$ compositions calculated from the Isla Floreana clinopyroxenes (**A.**) and published whole-rock data (**B.**). Clinopyroxene trace element data collected in this study (gabbros) and in Gleeson et al. (2020; wehrlites and antecrysts) are converted to equilibrium melt trace element compositions using the REE partitioning model of Sun and Liang (2012) at a temperature of 1150°C and a pressure of 0.5 GPa.*

490 Consequently, we consider possible formation of these gabbros during an earlier period of Isla
491 Floreana's magmatic history, prior to the period of current volcanism starting at ~1.5 Ma. At ~2 – 2.5
492 Ma Isla Floreana was located close to the present-day position of Volcán Cerro Azul, near the centre
493 of plume upwelling owing to the west-to-east motion of the Nazca tectonic plate (Argus et al., 2011;
494 Harpp et al., 2014). Lavas erupted at western Galápagos shield volcanoes, including Volcán Cerro

Azul, are typically plagioclase-phyric (Geist et al., 2002; Naumann and Geist, 2000), possess overlapping clinopyroxene Mg# and plagioclase An compositions with the Isla Floreana gabbros (Stock et al., 2020, 2018). They also possess high melt $[Sm/Yb]_n$ contents (Gibson and Geist, 2010) – indicating high pressure melting in the plume centre – that overlap with the equilibrium melt values predicted from the Isla Floreana gabbros (Fig. 6). In addition, radiogenic isotope data from a separate suite of Isla Floreana gabbros reveal Sr, Nd, and Hf isotope compositions that are distinct from the erupted Isla Floreana basalts, but overlap with the compositions measured from basalts in the western Galapagos (Volcán Cerro Azul and Volcán Sierra Negra). As a result, we propose that the Isla Floreana gabbros likely originate from a 'plume proximal' stage of Isla Floreana's magmatic history when the island was located close the centre of plume upwelling – near the present-day location of Volcán Cerro Azul – at around 2-2.5 Ma.

The proposed age of these xenoliths is also supported by the EDS maps and linescans, which can identify the degree of chemical heterogeneity and zoning within individual crystal phases. Chemical zoning – be it concentric, patchy, or oscillatory – is a common feature of plagioclase and clinopyroxene crystals in volcanic and plutonic environments worldwide (Bennett et al., 2019; Lissenberg and MacLeod, 2016; Sanfilippo et al., 2020). Our data, however, indicates almost complete homogeneity across each crystal phase with only smooth core-rim zoning of An contents identified in some plagioclase crystals (see Supplementary Material). This indicates that there has been sufficient time for chemical diffusion to smooth (or remove) any chemical zoning, even for the slowest diffusing elements. For example, EDS linescans reveal an absence of zoning in minor components of clinopyroxene (e.g., Ti) over length scales of ~100 μm, an observation in consistent with late-stage crystallization of magma within a cumulate mush (Lissenberg et al. 2016 and others). Assuming a temperature of 1000°C and diffusivities from Cherniak and Liang, (2012) simple calculations of diffusive length scales (i.e., $x = \sqrt{(4Dt)}$ ) indicate that homogenization over these distances likely require timescales more than 350,000 kyrs. Furthermore, Ca-Na interdiffusion in plagioclase is often considered to be negligible in volcanic systems due to the extremely low

diffusivities ($D_{Ca-Na}^{plag} \sim 7 * 10^{-25}\ m^2/s$ at 1000°C and $\sim 2 * 10^{-21}\ m^2/s$ at 1250°C; Grove et al., 1984). Nevertheless, given the ~2 Myr timescale proposed here, these diffusivities equate to Ca-Na diffusion length scales in plagioclase between 15 and 750 μm. Even at the lower end of this range these distances are consistent with diffusive 'smoothing' of any original An zoning in plagioclase crystals during cooling of these xenoliths, consistent to the gentle core-rim profiles observed in a subset of crystals. Combined with the high degree of textural equilibrium observed in the Isla Floreana gabbros (Gleeson et al., 2020a) this chemical homogeneity supports the proposed long-term storage of these samples and their origin within an ancient (~2 – 2.5 Myr) magmatic system beneath Isla Floreana.

## 4.2 THERMODYNAMIC CONSTRAINTS ON CUMULATE STORAGE AND SUBSOLIDUS HISTORY

The mineralogy, trace element composition, and isotopic signature of the Isla Floreana gabbros links these samples to the plume-proximal stage of the island's magmatic history at 2-2.5 Ma. However, there are several features within the Isla Floreana gabbros that contrast with the petrographic and chemical characteristics of the modern-day plume-proximal volcanic systems (e.g., Cerro Azul; Gleeson et al., 2020a; Harpp et al., 2014; Lyons et al., 2007; Naumann and Geist, 2000) and may provide insights into the storage conditions, and subsolidus history of these cumulate xenoliths.

The first difference lies in the absence of a stable olivine phase in the gabbros and the presence of orthopyroxene (Fig. 2). All shield volcanoes in the current western Galápagos erupt lavas saturated in some combination of olivine, clinopyroxene, and plagioclase (plus minor oxide phases), with orthopyroxene rare or absent (Geist et al., 2002; Naumann and Geist, 1999; Reynolds and Geist, 1995). In contrast, all gabbros considered here contain abundant orthopyroxene macrocrysts (>5%), but no stable olivine. Furthermore, the clinopyroxene crystals in Isla Floreana gabbros contain anomalously high $Na_2O$ contents (0.72 – 0.89 wt%) relative to data from volcanic systems in the western Galápagos (Fig. 4; Stock et al., 2020, 2018). Offsets are also seen in the clinopyroxene trace element contents. For example, our gabbroic clinopyroxenes contain clear Eu anomalies (defined as

$Eu^* = \frac{Eu_n}{\sqrt{Sm_n + Gd_n}}$), ranging from ~1.15 – 1.35 in samples 03b and 04b, to 1.4 – 1.6 in samples 09g1, 09g2, and 09g3 (Fig. 5). Similar Eu* values are not seen in any other clinopyroxene data from Isla Floreana (Fig. 5; Gleeson et al., 2020a) and while clinopyroxene trace element data is not available for any western Galápagos shield volcano, the Eu* values of erupted lavas in the western Galápagos does not exceed 1.1 (using compiled data from Gleeson et al., 2021 and Harpp and Weis, 2020).

As the Isla Floreana gabbros contain little chemical heterogeneity (i.e., an absence of chemical zoning) and high extents of textural equilibrium have previously been reported (Gleeson et al., 2020a), we hypothesize that the unusual chemical and mineralogical signatures of the Isla Floreana gabbros might result from chemical reactions that take place as the systems transition into equilibrium subsolidus assemblages. To investigate this, we use estimated whole-rock compositions from the EDS maps as inputs to thermodynamic models calibrated for sub-solidus igneous systems to examine the chemical and mineralogical changes that would occur during subsolidus cooling of cumulates. We use the Python3 package PetThermoTools (Gleeson & Wieser, 2024) to create phase diagrams for samples 03b and 04b using the pMELTS (Ghiorso et al., 2002), and Holland et al. (2018) thermodynamic models, implemented through alphaMELTS and MAGEMin (Riel et al., 2022; Smith and Asimow, 2005).

Results using the pMELTS thermodynamic model are shown in Fig. 7. The pMELTS simulations indicate that olivine is stable in these samples at pressure below ~750 MPa at 950°C, increasing to 800 – 850 MPa at the solidus (1200 – 1250°C). Garnet – also absent from our samples – is predicted to be stable at pressures >750 MPa at 950°C, increasing to >1100 MPa at the solidus. Consequently, it is only between these phase boundaries (olivine-out and garnet-in reactions), at temperatures above 950°C, where our observed mineral assemblage is predicted to be stable (Fig. 7). This indicates a final pressure of equilibration for these gabbros >750 MPa, far greater than the pressures expected at the base of the crust beneath Isla Floreana (~380-450 MPa; Feighner and Richards, 1994, using their assumed density of 2800 kg/m$^3$ for the crust). Calculations performed using the

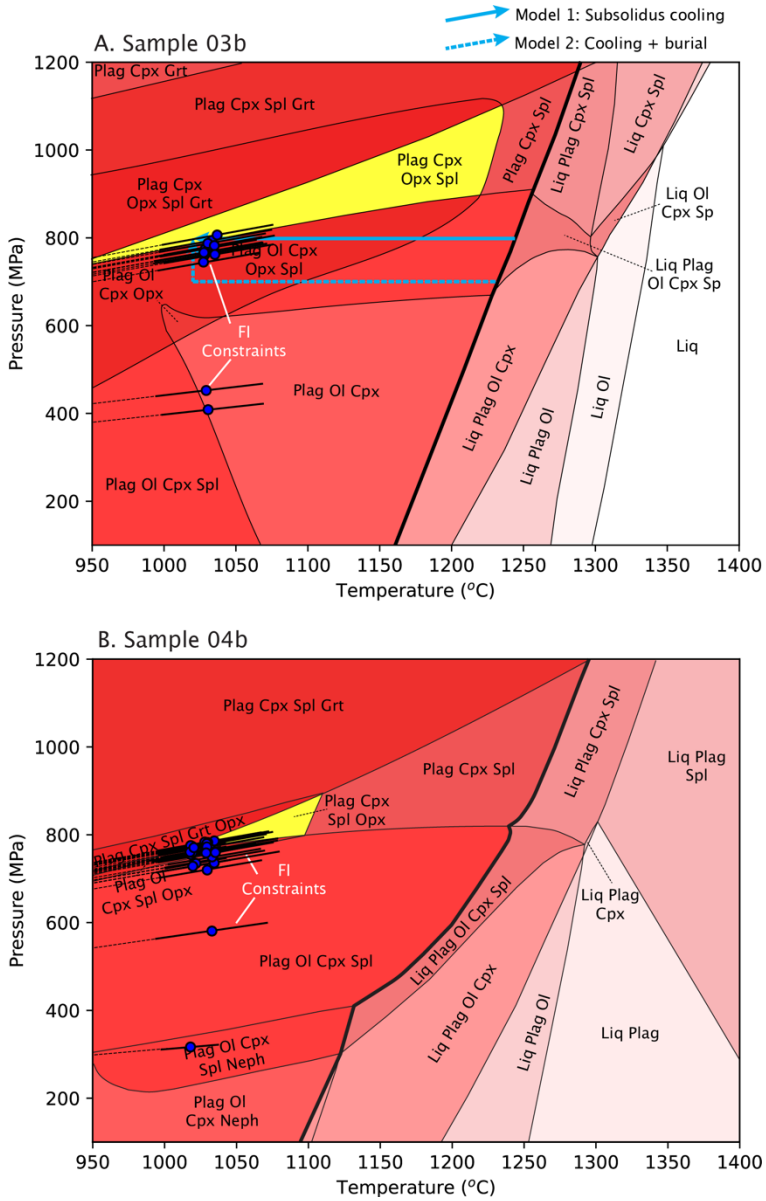


***Figure 7 –*** *Phase diagrams of samples 03b (**A.**) and 04b (**B.**) constructed in the NCFMASTOCr (Na, Ca, Fe, Mg, Al, Si, Ti, O, and Cr) system. All calculations are performed in PetThermoTools using the pMELTS thermodynamic model (Ghiorso et al. 2002, Gleeson & Wieser, 2024). P-T region where the observed mineralogy is recreated is highlighted in yellow. Also shown are the results of Fluid Inclusion (FI) barometry (solid lines indicate pressures calculated using clinopyroxene-orthopyroxene determined temperatures, dashed lines indicate pressures calculated using Mg-in-plagioclase determined temperatures), and the different subsolidus cooling and burial models used to investigate the phase compositions. For all calculations the $Fe^{3+}/Fe_{tot}$ ratio was set to 0.10. Thicker line indicates the position of the solidus. FI pressures are determined by randomly sampling 1000 temperatures from the clinopyroxene-orthopyroxene thermometry results with the median (circles) and mean ± 2*standard deviation (solid lines) pressure and temperature results shown. Similar calculations are performed using the Mg-in-plagioclase determined temperatures, with the results displayed using the dashed black lines.*

571 Holland et al. (2018) thermodynamic models, however, predict greater pressures for the garnet-in

572 and olivine-out reaction boundaries. For example, the olivine-out phase reaction occurs between

573 ~800 and 900 MPa for the Holland et al. (2018) thermodynamic model (see Supplementary
574 Information).

575 In addition to estimating the final storage pressure of these cumulates, the pMELTS phase diagrams
576 also provide insights into the phase reactions that occur during subsolidus cooling. For example, our
577 phase calculations indicate that orthopyroxene is not stable at or above the solidus. In fact,
578 assuming these gabbro nodules originated as a cumulate mush (melt + crystals), the initial cumulus
579 phases were likely clinopyroxene + plagioclase + olivine +/- spinel, consistent with the cumulus
580 assemblage predicted for active volcanic systems in the western Galápagos where orthopyroxene is
581 rarely observed (Geist et al., 2002; Naumann and Geist, 1999; Stock et al., 2020). The presence of
582 orthopyroxene therefore supports our hypothesis that significant chemical and mineralogical
583 changes occurred during subsolidus cooling, which we examine in more detail using two possible
584 subsolidus cooling models.

585 In the first model we assume that the system starts at the solidus at a pressure of 800 MPa and
586 undergoes isobaric cooling to a temperature of 1020$^{o}$C (Fig. 8) based on clinopyroxene-
587 orthopyroxene thermobarometry. In our second model, we assume the solidified gabbroic mush
588 zone undergoes an initial period of isobaric cooling at lower pressure, followed by a period of burial
589 (increasing pressure) due to emplacement of lava/intrusions at shallower levels (Fig. 8). This second
590 model is similar to that proposed by Lyons et al. (2007) and assumes emplacement of ~5 km of lava
591 or shallow level intrusions following initial formation of the gabbro cumulates (approximately half of
592 the total thickness of the Galápagos Platform). Ultimately, this leads to an increase in the system
593 pressure from ~670 MPa to 800 MPa.

594 For both samples considered here the two models demonstrate a sequence of phase changes during
595 cooling (and burial) that can be simplified as:

596 $$plagioclase + olivine \rightarrow spinel + orthopyroxene\ (+clinopyroxene)$$

The decrease in the modal proportion of olivine and plagioclase in these samples during cooling (and pressurization, Fig. 8) requires a re-distribution of Na, Sr, and Eu – elements that are dominantly found in plagioclase – into other mineral phases. Our models reveal an increase in the $Na_2O$ content of clinopyroxene during cooling (by a factor of ~1.6-1.8X; Fig. 8). While MELTS cannot model Sr-Eu partitioning directly, we propose that these sub-solidus reactions may also be responsible for the strong positive Eu anomalies found in the gabbroic clinopyroxenes. Interestingly, in the subsolidus cooling models there is a decrease in the clinopyroxene $TiO_2$ content, consistent with the slightly lower concentration of $TiO_2$ in the gabbro clinopyroxenes compared to data from Volcán Wolf (Fig. 4).

The thermodynamic models also provide a potential explanation for the presence of olivine crystals in orthopyroxene breakdown rims of samples 09g1-3, identified through high-resolution EDS mapping paired with automated mineral classification by mineral ML (Fig. 3). The stability of orthopyroxene is highly sensitive to pressure (Fig. 7), with replacement of orthopyroxene by olivine predicted to occur during depressurization. We suggest that the breakdown rims formed during ascent and decompression of these nodules either shortly prior to, or during eruption. What remains uncertain is why breakdown rims are observed in the 09g samples, but not in 03b and 04b. One important difference between the sample groups is that 03b and 04b were collected from explosively emplaced scoria cones, whereas 09g were found within the centre of a blocky lava flow. This could suggest that variations in ascent rate and/or surface cooling timescales could influence the formation of these orthopyroxene break-down rims.

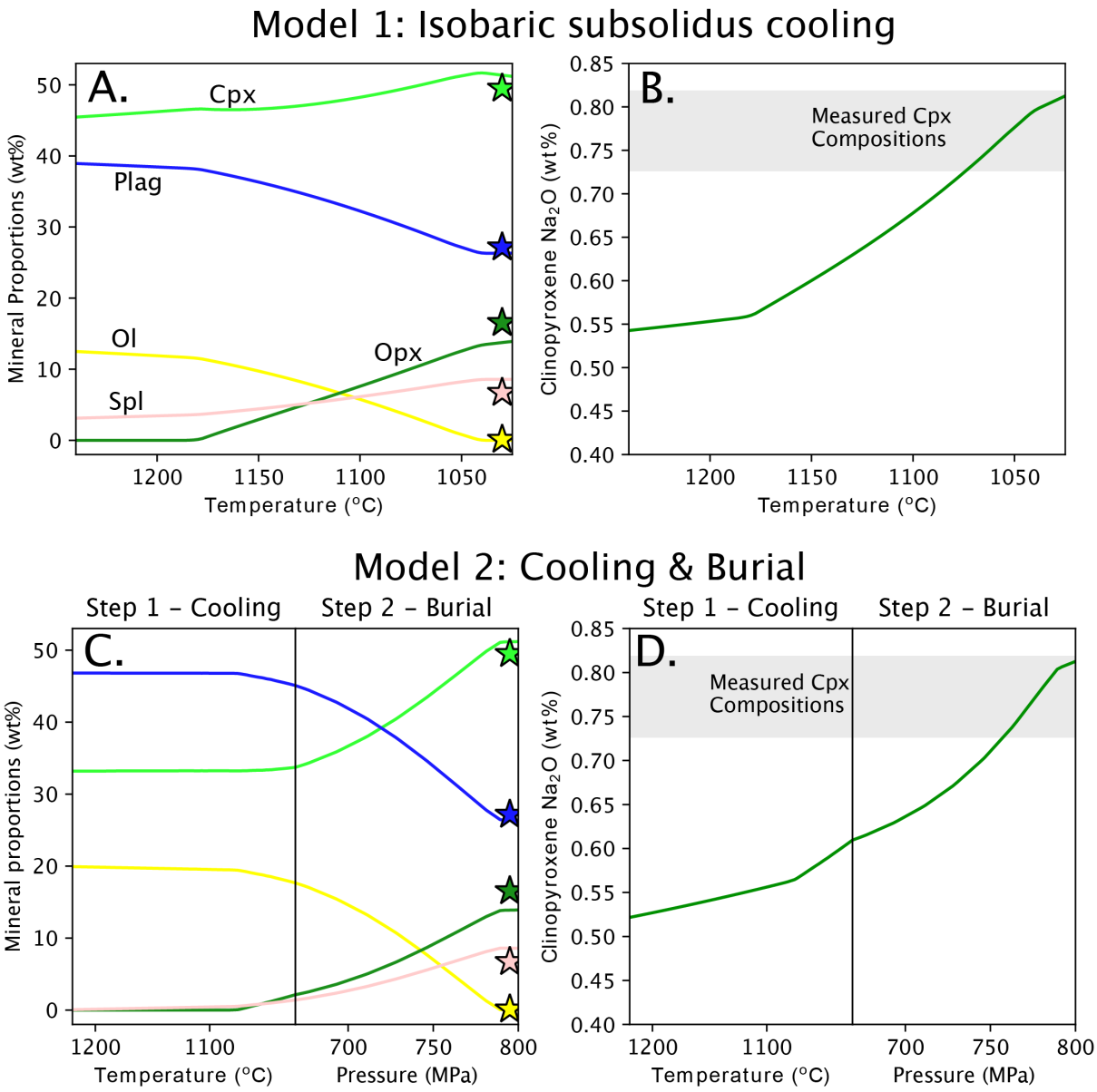


***Figure 8*** *–Phase proportions and mineral chemistry predicted during cooling and burial from the solidus.* ***A.*** *Mineral proportions predicted during isobaric cooling at 800 MPa. Color scheme as in Fig. 2. Stars indicate the measured mineral proportions derived from the EDS maps.* ***B.*** *Change in clinopyroxene $Na_2O$ contents during isobaric cooling. The grey region represented the range of measured clinopyroxene $Na_2O$ contents in sample 03b.* ***C. & D.*** *Mineral proportions and clinopyroxene chemistry, respectively, predicted during (i) isobaric cooling at 670 MPa, and (ii) burial to 800 MPa.*

## 4.3 Formation and Storage Depths

One of the key predictions from the thermodynamic modelling described above is that the absence of olivine in these gabbros requires pressures greater than that found at the Moho, and thus formation and/or storage below the base of the oceanic crust (Fig. 7). The thermodynamic modelling does, however, contain significant uncertainties that are difficult to fully quantify or demonstrate

(including the offset between different models, the uncertainty in bulk-rock estimates, and the oxygen fugacity/water content of the subsolidus system). To more rigorously assess the pressure of gabbro formation and storage beneath Isla Floreana, we consider the available independent barometric evidence from both mineral chemistry and fluid inclusion $CO_2$ densities.

### 4.3.1 Mineral Thermobarometry

Due to the presence of subsolidus equilibration in the Isla Floreana gabbros, widely used melt-based thermobarometers (e.g., Cpx-Liq) and single-phase thermobarometers that were calibrated on mineral-melt pairs (e.g. Cpx-only) cannot be applied to our samples (Gleeson et al., 2020a). However, thermobarometers based on equilibria between different solid phases might provide first order constraints on the pressure of gabbro storage and, more importantly, constrain the system temperature (a necessary input parameter for converting fluid inclusion measurements into pressure estimates). For example, the temperature dependent exchange of Mg (coupled with Ca) between clinopyroxene and plagioclase holds a lot of promise for sub-solidus mafic systems and has previously been used to evaluate the cooling history of oceanic gabbros (Faak et al., 2014; Sun and Lissenberg, 2018).

Plagioclase compositions for the gabbroic xenoliths, determined through coupled EDS (Si, Al, Ca, Na, Fe) and WDS (Mg, K) analysis, show little variability within each sample (both core and rim analyses were performed for each crystal). Samples 09g1-3 have low Anorthite contents (An = Ca/(Ca+Na+K) *molar*), ranging from 0.625 (09g1) to 0.643 (09g3), and moderately high $K_2O$ contents around 0.163 – 0.191 wt% (Fig. 9). Sample 04b is characterized by substantially higher An values (~0.76), with sample 03b displaying intermediate compositions (~0.67 – 0.69; Fig. 9). Samples 03b and 04b also show lower $K_2O$ contents than the 09g gabbros 0.061 – 0.112 wt%. Notably, the An-$K_2O$ relationships in the gabbroic plagioclase closely mirrors that observed in plagioclase data from Volcán Wolf, chosen as a characteristic volcanic system in the western Galápagos due to the abundance of mineral data available (Fig. 9b; Stock et al., 2020). The MgO contents measured in the gabbroic

647 plagioclase are, however, substantially lower than the bulk of the data from Volcán Wolf. Samples
648 09g1, 09g2, and 09g3 contain average MgO contents of 0.032 wt%, 0.027 wt%, and 0.024 wt%,
649 respectively (Fig. 9c). These values are lower than those measured in samples 03b and 04b (0.038
650 wt% and 0.037 wt%, respectively).

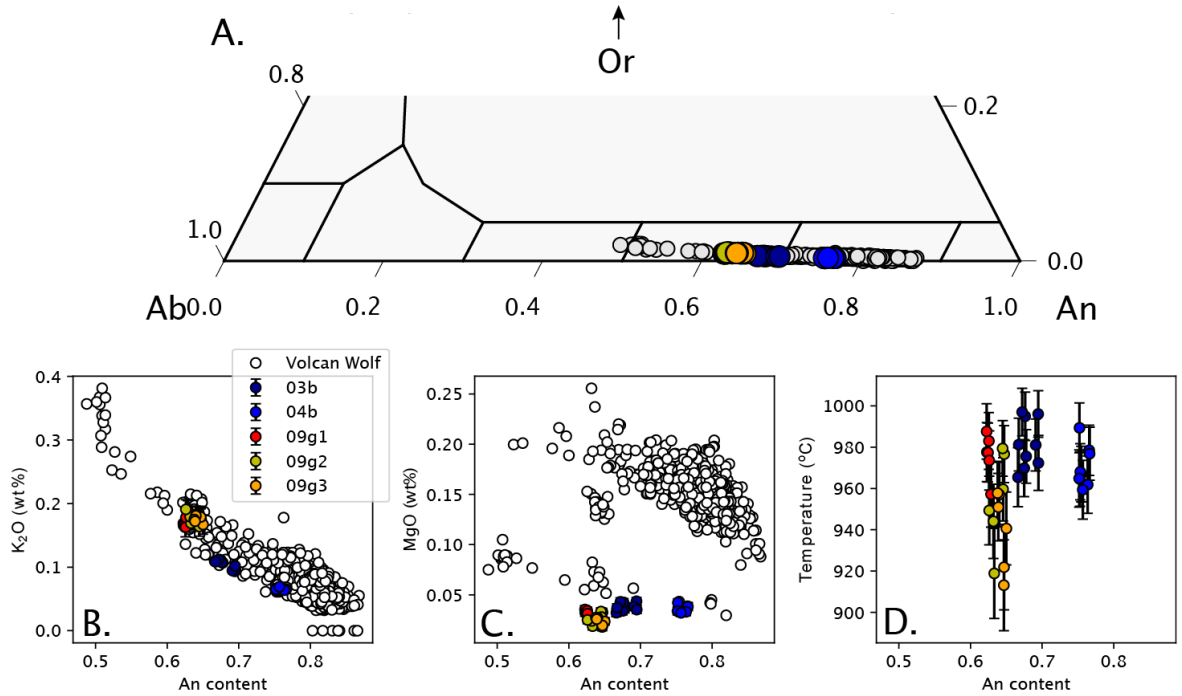


***Figure 9 –*** *Plagioclase compositions from the Isla Floreana gabbros compared to data from Volcán Wolf (Stock et al. 2020).* ***A.*** *Feldspar ternary plot produced using the Python3 package Thermobar (Wieser et al. 2022).* ***B.*** *$K_2O$ contents against plagioclase An content.* ***C.*** *Plagioclase MgO contents determined by WDS analysis.* ***D.*** *Temperature calculated from the thermometer of Sun and Lissenberg (2018). All error bars show the 1 sigma analytical uncertainty, with this uncertainty propagated through to the temperature calculations.*

651 These plagioclase MgO contents, combined with EDS analysis of clinopyroxene crystals in the same
652 samples (to determine the Mg partition coefficient $K_{Mg} = {Mg_{Plag}}/{Mg_{Cpx}}$), can be used to evaluate
653 the storage temperature of the Isla Floreana gabbros. To evaluate the uncertainty on our
654 temperature calculations, we use a Monte Carlo approach to propagate the analytical error
655 associated with the plagioclase MgO and An contents, and mean clinopyroxene MgO contents. For
656 each analysis and each parameter, we generate 2000 samples from a normal distribution with a
657 standard deviation defined by the either the 1 sigma analytical uncertainty (e.g., plagioclase MgO
658 contents) or the 1 sigma variation in measured composition (e.g., the mean clinopyroxene MgO

659 contents). As the parameterization is also pressure sensitive, we incorporate uncertainty in pressure
660 using a uniform distribution spanning 0.2 and 0.8 GPa, the previously determined range in magma
661 storage conditions for Galápagos basalts (Bell et al., 2021; Gleeson et al., 2020a; Stock et al., 2018).
662 The mean temperature estimated for each individual plagioclase analysis varies from 913.2°C
663 (±22.0°C) to 997.0°C (±11.5°C; Fig. 9d).

664 In addition to the Mg in plagioclase thermometer, the temperature and pressure of the system can
665 be estimated using the composition of co-existing clinopyroxene and orthopyroxene crystals
666 (Putirka, 2008). Importantly, EDS linescans reveal no compositional zoning in either clinopyroxene or
667 orthopyroxene crystals near the grain boundaries, indicating complete chemical equilibration
668 between these phases at their subsolidus storage conditions. To evaluate the role of analytical
669 uncertainties on the precision of our 2-pyroxene thermobarometric calculations we generated 200
670 hypothetical clinopyroxene/orthopyroxene compositions for each EDS analysis using Thermobar (3 –
671 5 analyses taken per crystal Wieser et al., 2022). These compositions were determined by assuming
672 a normal distribution of probabilities centered on the measured oxide concentration (i.e., the mean
673 of the distribution) with a standard deviation set by the estimated error of analysis. For each
674 clinopyroxene-orthopyroxene pair this process resulted in 600 – 1000 paired compositions that were
675 used to calculate the temperature and pressure of storage. Calculations were performed by iterating
676 the results of equations 36 & 38 and equations 36 & 39 from Putirka (2008), implemented in the
677 Python3 package Thermobar (Wieser et al., 2022).

678 Temperatures determined through clinopyroxene-orthopyroxene thermobarometry, iterating
679 equation 36 (temperature) with equation 38 (pressure) from Putirka (2008), range from 1042.3°C
680 (±18.9°C) for sample 04b to 1014.4°C (±11.4°C) in sample 09g1 (Fig. 10). If equation 39 is used to
681 determine the system pressure, the mean temperature estimated for each sample decreases by
682 approximately 10-20°C. Overall, our results indicate that clinopyroxene-orthopyroxene equilibrium
683 in the Isla Floreana gabbros records temperatures at the upper end of those estimated by Mg-in-

684 plagioclase thermometry, but with smaller uncertainties. At present, the cause of the offset between
685 the two methods is not clear, but the region of overlap between the two methods indicates that
686 storage at >900°C is likely for the Isla Floreana gabbros (Fig. 10).

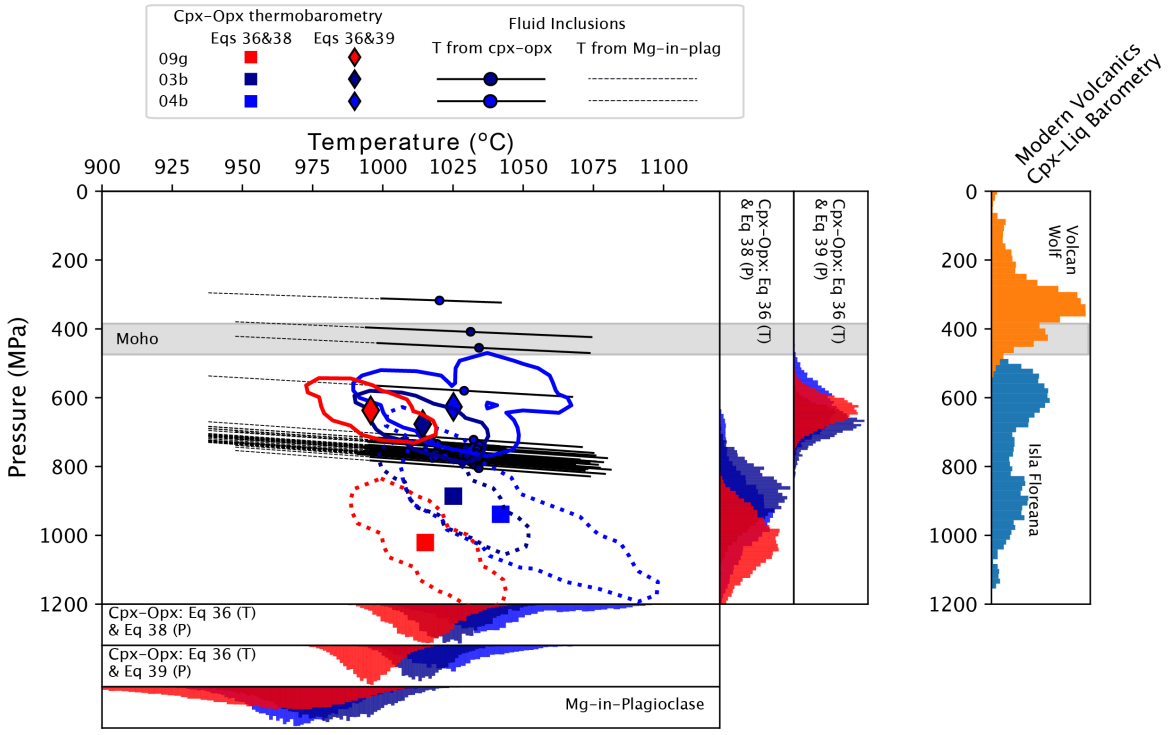


***Figure 10 –*** *Barometric results from the Isla Floreana gabbros (left hand panels) against the estimated Moho pressure and barometric analysis of modern day volcanics in the western (Volcán Wolf) and eastern (Isla Floreana) Galápagos. Modern day estimates are calculated using published clinopyroxene and liquid compositions from Stock et al. (2018) and Gleeson et al. (2020), for Volcán Wolf (orange) and Isla Floreana (blue), respectively. Calculations are performed in Thermobar, using the Neave and Putirka (2017) barometer solved iteratively with equation 33 from Putirka (2008). Melt matching algorithms were performed with the same limits as used in the original papers. Pressure and temperature estimates derived from the Isla Floreana gabbros, which include cpx-opx thermobarometry, Mg-in-plagioclase thermometry, and FI barometry (assuming pure $CO_2$ fluids), indicate storage of these gabbros at pressures below the Moho. FI pressures are determined by randomly sampling 1000 temperatures from the clinopyroxene-orthopyroxene thermometry results with the median (circles) and mean ± 2*standard deviation (solid lines) pressure and temperature results shown. Similar calculations are performed using the Mg-in-plagioclase determined temperatures, with the results displayed using the dashed black lines.*

687 Application of clinopyroxene-orthopyroxene equilibria to determining the pressure of gabbro
688 storage is, however, associated with significant uncertainty due to the large variation in estimated
689 pressures associated with different equation pairs. If equation 39 is iterated with equation 36 to
690 simultaneously solve for pressure and temperature our data indicates storage around 627 ±59 MPa
691 (sample 04b) to 678 ±42 MPa (sample 03b). If we instead use equation 38 (which is independent of

692 temperature) to determine the system pressure, we get estimates of 940 ±102 MPa and 886 ±72
693 MPa for samples 04b and 03b (Fig. 10). The large difference between the two barometric equations
694 indicates that there is a large degree of uncertainty in these pressure calculations. Considering the
695 95% confidence 'envelope' on a P-T plot (calculated using the Python3 package pyrolite; Williams et
696 al., 2020) reveals a small region of overlap between the two clinopyroxene-orthopyroxene pressure-
697 temperature calculations at ~750 MPa and 1000 – 1025°C (Fig. 10). However, given the difference
698 between the two equations, and the uncertainties estimated for each approach, all we can
699 realistically conclude from clinopyroxene-orthopyroxene barometry is that these gabbros were likely
700 stored at pressures higher than ~450 MPa, representing the maximum possible pressure at the base
701 of the oceanic crust beneath the Galápagos Platform (calculated using the crustal thickness estimate
702 of Feighner and Richards (1994a) and a constant crustal density of 2800 kg/m$^3$).

703 ### 4.3.2 Fluid Inclusion Barometry

704 Both thermodynamic simulations and clinopyroxene-orthopyroxene barometry indicate that the
705 gabbro xenoliths were stored at >450 MPa, below the base of the Galápagos crust. Unlike mineral
706 thermobarometers, which are relatively imprecise (e.g. Root Mean Square Error (RMSE) >3 kbar for
707 clinopyroxene-orthopyroxene; Wieser et al. 2025), the density of $CO_2$ fluids trapped within crystals
708 can provide a more sensitive barometer in $H_2O$-poor ocean island systems assuming the
709 temperature of the system is somewhat constrained (and that inclusions are not modified during
710 suberuptive ascent and/or cooling at the surface).

711 In sample 04b we identified and measured 30 apparent primary fluid inclusions (FIs) in 8
712 clinopyroxene crystals, and in sample 03b we found 3 apparent primary FI in 1 clinopyroxene and 1
713 plagioclases respectively, as well as 7 FIs across 2 secondary trails (1 plagioclase crystal and 1
714 clinopyroxene crystal; Fig. 11). Of the 43 fluid inclusions, 37 display homogenization temperatures
715 between -9.8°C and -19.1°C. Of the remaining FIs, 3 in sample 04b show clear signs of decrepitation
716 (see Supplementary material) and display $T_h$ values between 27 – 27.1°C (1 FI) and the critical point

717 of $CO_2$ (2 FIs). Other inclusions with higher homogenization temperatures include one FI in sample
718 04b ($T_h$ = 4.8 – 4.9°C), and 2 neighboring, apparent primary fluid inclusions in sample 03b ($T_h$ = 17.0 –
719 17.1°C and $T_h$ = 20.9 – 21.0°C). These 3 FIs are located near the crystal margins, and are among the
720 largest inclusions in our dataset, making them more susceptible to mechanical re-equilibration
721 during ascent and stalling (Wanamaker and Evans, 1989). As we are interested in determining the
722 long-term storage conditions of these xenoliths prior to ascent in their carrier liquid, we only
723 primarily consider inclusions with no clear signs of decrepitation/re-equilibration (and thus highest
724 densities) in the discussion below.

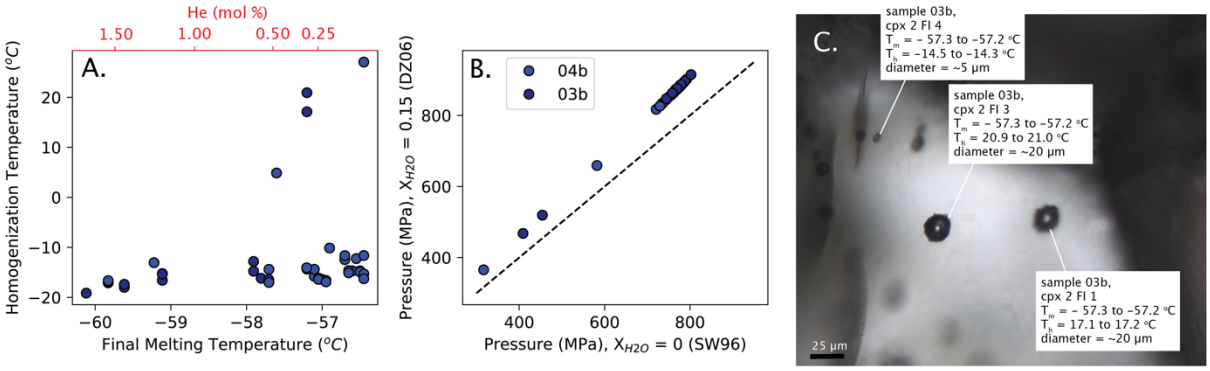


***Figure 11 –*** *Analysis of fluid inclusions (FIs) from samples 03b and 04b.* ***A.*** *Comparison of mean homogenization temperature against the final melting temperature. Mixed $CO_2$-He EOS calculations are used to convert the melting temperature of these inclusions into estimates of the possible He content of these fluid inclusions.* ***B.*** *Comparison of entrapment pressures (at the mean temperature determined by cpx-opx thermobarometry) for different $X_{H2O}$ values (EOS of Span and Wagner (1996) is used when $X_{H2O}$ = 0.0; Duan and Zhang (2006) mixed EOS is used for $X_{H2O}$ = 0.15).* ***C.*** *Example FIs from sample 03b, including the 2 larger inclusions that return anomalously high homogenization temperatures.*

725 Assuming the trapped fluids are pure $CO_2$, the homogenization temperatures indicate fluids densities
726 between 0.98 – 1.03 g/cm$^3$. Using the median temperature from all clinopyroxene-orthopyroxene
727 thermobarometry calculations for each respective sample we can convert these pure-$CO_2$ densities
728 into storage pressures ranging from 719 – 802 MPa using the Span and Wagner (1996) EOS in DiadFit
729 (Wieser and DeVitre, 2024). A Monte Carlo approach, accounting for the uncertainty in the
730 measured homogenization temperatures and the equilibration temperatures determined through
731 clinopyroxene-orthopyroxene thermobarometry, suggests uncertainties of +/- 9 MPa for sample 04b
732 and +/- 10 MPa for sample 03b (implemented in DiadFit, Wieser and DeVitre, 2024). Consequently,

our data – assuming pure $CO_2$ fluids – strongly supports the thermobarometry and thermodynamic results discussed above: the Isla Floreana gabbros were stored below the base of the crust, within the lithospheric mantle, prior to entrainment and ascent in their carrier melt.

Converting homogenization temperatures into fluid densities and, ultimately, entrapment/equilibration pressures does, however, require greater examination of the fluid composition. Prior analysis of the $H_2O$ content of Galápagos magmas reveals erupted melt $H_2O$ contents around 0.5 – 1.0 wt% across the southwestern region of the archipelago, with reactive porous flow in crystal mush zones generating anomalously $H_2O$-rich melt signatures (~2 wt%; Gleeson et al., 2022; Peterson et al., 2017). To account for the possible presence of $H_2O$ in the initial fluid phase we perform calculations using the mixed $CO_2$-$H_2O$ EOS from Duan and Zhang (2006) implemented in DiadFit (Wieser and DeVitre, 2024). For these calculations we use a fluid $X_{H2O}$ composition of 0.15, representing the maximum $X_{H2O}$ value for any Galápagos magma at mantle depths (using estimates of melt $H_2O$ contents from the nominally anhydrous mineral analyses of Gleeson et al. 2022). Results demonstrate that incorporation of minor $H_2O$ into these fluids leads to increase in the estimated equilibration pressures, with the median pressure for calculations performed with a $X_{H2O}$ of 0.15 ranging from 821 to 916 MPa. Overall, our calculations indicate that the presence of water increases the estimated pressure by ~14%, further supporting the idea that these gabbros were formed, and were stored, well-below the base of the crust.

As $H_2O$ and $CO_2$ are immiscible at room temperature, the presence of $H_2O$ will not influence the melting point of a $CO_2$-rich fluid inclusion. However, our microthermometry results reveal only 15 inclusions – all in sample 04b – with final melting temperatures within 0.2°C of the melting temperature for pure $CO_2$. Eight other FIs from sample 04b and 3 primary fluid inclusions from sample 03b have final melting temperatures within 1°C of the pure $CO_2$ melting point, with the remaining inclusions displaying final melting temperatures as low as -60.1°C. In addition, inclusions with low melting temperatures melt over a larger temperature range, with melting initiating as low

as -64.5°C in some cases (although the point of melting initiation was difficult to constrain due to the small size of many of these inclusions; ~2 μm). This melting point depression indicates the presence of an additional component (aside from $H_2O$ and $CO_2$) within the FIs from sample 03b and 04b. Raman spectroscopy did not detect any other Raman-active gaseous species (ruling out $N_2$, $H_2S$, $SO_2$ etc.). Thus we suggest that the observed freezing point depression results from the presence of a Raman-inactive noble gas (e.g., He, Ne, Ar). Although not quite as low as our temperatures here, it is notable that Frezzotti et al. (1992) report melting temperatures of -58.2-56.5°C in xenoliths from Salt Lake Crater, Oahu, which also do not show any Raman-active species other than $CO_2$.

Using mixed $CO_2$-He and $CO_2$-Ar EOS in CoolProp (Bell et al., 2014; Kunz and Wagner, 2012), we can calculate the predicted triple point temperature depression caused by the presence of He or Ar in the 03b and 04b FIs. These calculations suggest that the melting-point depression of the 03b and 04b FIs could result from the presence of up to 1.7 mol% He or 2.7 mol% Ar (or some combination of both). He and Ar proportions up to ~2 mol% have been identified in FIs from picritic lavas and mantle xenoliths collected from La Palma, Canary Islands (Sandoval-Velasquez et al., 2023), supporting this interpretation. We cannot examine the influence of He or Ar on the estimated FI equilibration pressures because converting mixed $CO_2$-He and $CO_2$-Ar fluid densities into high-temperature (~1020°C) equilibration pressures is restricted by the temperature range of the mixed EOS calibrations, and the inability of CoolProp to converge on solutions for these mixed fluids above ~300 – 400°C. To place a first order assessment on the influence of He and Ar on the estimated pressures we use CoolProp to track the P-T trajectory of isochores for theoretical FIs with a homogenization temperature of -17°C and a range of He and Ar proportions until the maximum convergence temperature for each fluid mixture is reached. The calculations reveal that, for a $CO_2$-Ar mixed fluid, the presence of 2 mol% Ar lowers the estimated equilibration pressure by <2% (at ~450°C) relative to the isochore of a pure-$CO_2$ fluid). The presence of He, however, can increase the estimated equilibration pressure by 15% (at a temperature of ~270°C), with this relative offset decreasing with increasing temperature (see Supplementary Information). Therefore, while we cannot directly

784 estimate the equilibration pressure of $CO_2$-He and $CO_2$-Ar mixed fluids at the storage temperature of
785 the Isla Floreana gabbros, we conclude that these impurities are likely to have a very minor negative
786 (Ar) or moderate positive (He) influence on the estimated storage pressure derived from the FIs in
787 samples 03b and 04b. As a result, although uncertainties in fluid composition undoubtedly influence
788 the pressure estimates derived from FI measurements, we suggest that the FIs found in samples 03b
789 and 04b confirm that the Isla Floreana gabbros were stored at pressures greater than ~700 MPa and
790 less than ~1 GPa (maximum pressure estimated from $CO_2$-$H_2O$ calculations combined with the
791 potential influence of He), with a handful of fluid inclusions recording lower pressures due to
792 decrepitation, leakage, re-equilibration, and/or stalling on ascent. Focusing on the fluid inclusions
793 with melting temperatures within 0.1°C of pure $CO_2$ indicates that the final storage pressure is
794 between 729 MPa ($X_{H2O}$ = 0.0) to 873 MPa ($X_{H2O}$ = 0.15). These pressure estimates closely align with
795 the pressures determined by our thermodynamic calculations where the gabbro phase assemblage
796 is recreated at 750 – 800 MPa and 850 – 1000 MPa (at 1020°C) for the pMELTS and Holland et al.
797 (2018) thermodynamic models, respectively.

798 Converting these pressure estimates into depths using a constant crustal density of 2800 kg/m$^3$
799 above 16 km and an assumed mantle density of 3200 kg/m$^3$ below this depth, we constrain the
800 storage depth of the Isla Floreana gabbros to 25.2 – 29.8 km depth (P = 730 – 870 MPa). Critically,
801 the depth of gabbro storage estimated here is significantly greater than the base of the oceanic crust
802 beneath Isla Floreana (~16 km; Feighner and Richards, 1994), indicating that these samples likely
803 formed, and were stored, within the mantle portion of the lithosphere. Therefore, we propose that
804 during the plume-proximal stage of Isla Floreana's volcanic history magma storage was characterized
805 by the presence of "crustal" intrusions (i.e., plagioclase-bearing cumulates) within the lherzolite –
806 harzburgite mantle residue of the Nazca lithosphere.

807 Owing to the small number of samples considered in this study we cannot rule out the possibility
808 that additional samples would reveal the presence of a wider (i.e. more vertically extensive) region

of magma storage beneath Isla Floreana. However, we note that a separate set of gabbroic samples analyzed by Lyons et al. (2007) also contain the opx-bearing mineralogy signature that is only stable at sub-Moho pressures (see Supplementary Material). Overall, we find no evidence for magma storage at shallower pressures, either during the plume-proximal or plume-distal period of Isla Floreana's magmatic history, indicating that crustal-level magma storage systems and/or intrusive bodies near the Moho either did not occur or were small and ephemeral and are not represented in the Isla Floreana xenolith populations.

# 5 Implications for volcanic structure and evolution in near-ridge settings.

Traditional models for volcanic evolution in ocean island settings are largely based on observations from Hawai'i, and relate changes in the magma storage conditions and erupted compositions of lavas to the position of each volcano relative to the centre of plume upwelling (Clague and Sherrod, 2014; Geist et al., 2014, 1995). As the pressure of magma storage beneath basaltic ocean island volcanoes and the flux of mantle derived magma into the lithosphere have recently been shown to be tightly linked (Baxter et al., 2023; Baxter and Maclennan, 2024; Gleeson et al., 2020a), we would expect to see a systematic increase in the pressure of magma storage as volcanic systems move away from the centre of plume upwelling; i.e., the shield to post-shield transition on Hawai'i (Clague and Sherrod, 2014).

If we consider the modern-day volcanic activity in the Galápagos, the available data appears to fit this prediction very well. Plume-proximal systems that receive the largest flux of mantle-derived magma, such as Isla Fernandina, Volcán Wolf, Volcán Sierra Negra, or Volcán Cerro Azul, are characterized by mid-crustal magma storage regions that feed regular volcanic activity (Bell et al., 2021; Higgins and Stock, 2024; Stock et al., 2018). By contrast, the recent volcanic activity at Isla

Floreana, located ~100 – 150 km east-south-east of the centre of Galápagos plume upwelling, is characterized by the high-pressures of magma storage typical of a post-shield, or plume-distal, low melt-flux volcanic centre (Gleeson et al., 2022, 2020a; Fig. 12). From these observations we may have expected the Isla Floreana gabbros, associated with the plume-proximal period of Isla Floreana's magmatic history (Lyons et al., 2007), to record shallow, mid-crustal pressures (similar to the modern-day western Galápagos shield volcanoes). However, our new data indicates that the Isla Floreana gabbros were stored around 10 km below the base of the crust at pressures of ~750 MPa, similar to the pressure estimated for the recent Isla Floreana magmatic system (Gleeson et al., 2022, 2020a).

As indicated above, a wider region of magma storage – extending to the base of the oceanic crust – cannot be ruled out owing to the small number of samples analyzed. However, our data, combined with the mineralogical signature of other xenolith sample suites from Isla Floreana, clearly indicates that there has been persistent high-pressure magma storage at depths greater than the base of the crust throughout the ~2.5 Myrs of magmatic activity on Isla Floreana. In fact, there is no geochemical or petrological data currently available to indicate that Isla Floreana underwent any period of sustained magma storage within the crustal portion of the lithosphere. The absence of crustal storage beneath Isla Floreana, and other eastern Galápagos volcanic islands, is supported by the absence of shallow-level crustal cumulates detected by recent gravity surveys on other islands in the eastern archipelago (Cleary et al., 2020). We suggest that Isla Floreana has been characterized by a low magma flux (relative to the modern western Galápagos islands of Isabela and Fernandina) throughout its 2.5 Myr history, insufficient to sustain crustal-level magma storage (as links between magma storage depths and mantle derived melt flux have recently been established Baxter et al., 2023; Gleeson et al., 2020a). Importantly, this indicates that the eastern Galapagos volcanic islands cannot be considered as older 'analogues' for the present-day western Galapagos shield volcanoes. The different morphologies and chemical heterogeneity of erupted products, therefore, do not

857 relate to different stages of magmatic evolution, but are likely controlled by differences in the
858 magma flux rate through these volcanoes magmatic histories.

859 The origin of the anomalously low magma flux to the Isla Floreana magma system (and other eastern
860 Galapagos volcanic islands) during its plume proximal stage of volcanic activity could have several
861 origins. Temporal variations in the volume flux of mantle plume systems can occur – and have been
862 documented in Hawai'i – on similar timescales to that investigated here (Morrow and Mittelstaedt,
863 2021; Van Ark and Lin, 2004; Vidal and Bonneville, 2004; Wessel, 2016). However, we suggest that

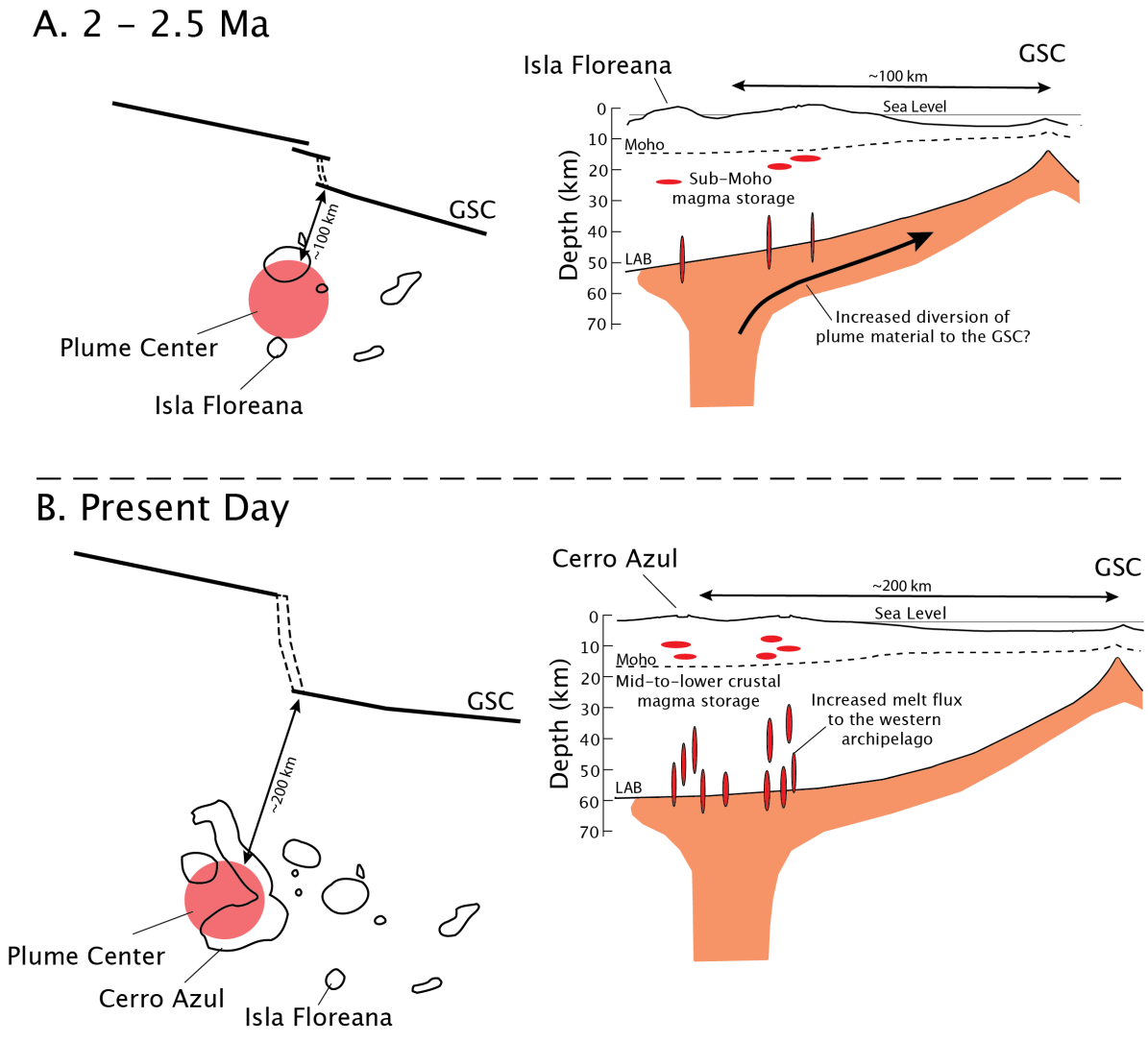


***Figure 12 –*** *Comparison of the tectonic setting of the Galápagos archipelago at 2 – 2.5 Ma (**A.**) and at the present day (**B.**). Reconstruction of the Galápagos Spreading Centre (GSC) is taken from Mittelstaedt et al. (2012), with the right hand panels adapted from Cleary et al. (2020). Schematic diagrams show the proposed increase in melt flux to the western Galápagos due to the increasing plume-ridge interaction distance with time and the smaller volume of plume material (and melt) transported north to the GSC. LAB – Lithosphere Asthenosphere Boundary.*

our data supports the recent hypothesis of Cleary et al. (2020), that the persistent low melt flux supplied to the eastern Galapagos islands is related to the changing tectonic setting of the Galápagos mantle plume. Specifically, ~2-2.5 Myrs ago, when Isla Floreana and the other eastern Galápagos volcanic islands were located close to the centre of plume upwelling, the GSC was ~100 km closer to plume stem than it is at the present day. The increased proximity of the plume to the ridge at this time might have allowed more plume material and melt to be diverted northwards towards the ridge axis, causing more distributed volcanism across the Galápagos Platform and lowering the melt flux beneath the islands (Cleary et al., 2020; Gleeson and Gibson, 2021; Harpp and Geist, 2018), an interpretation which is supported by localized crustal thickness anomalies to the north of the GSC (Mittelstaedt et al., 2014). Furthermore, diversion of the plume material northwards, towards to GSC, might have the greatest effect on Isla Floreana owing to its location at the southern margin of the Galápagos Platform. As a result, when the eastern Galápagos islands were formed, Isla Floreana was characterized by a far lower flux of magma into the lithosphere then there is beneath the present-day western Galápagos shield volcanoes of Volcán Cerro Azul or Volcán Sierra Negra.

# 6 CONCLUSIONS

Our new clinopyroxene trace element data, alongside published isotopic data of similar samples (Lyons et al., 2007), indicates that gabbroic xenoliths found in lava and scoria deposits on Isla Floreana in the southern Galápagos formed at ~2 – 2.5 Ma, when the island was located close to the centre of plume upwelling. Consequently, these samples provide an important insight into the temporal evolution of the Isla Floreana magmatic system, as well as the evolution of the Galápagos Archipelago in a rapidly evolving tectonic setting. Mineral compositions determined by EDS and WDS, alongside analysis of $CO_2$-density in clinopyroxene- and plagioclase-hosted fluid inclusions, are used to estimate the final storage conditions of these gabbros prior to entrainment and ascent in their carrier melt. Our results indicate that the Isla Floreana gabbros were stored at ~900 – 1050 $^{o}$C,

888 with pressures determined by clinopyroxene-orthopyroxene thermobarometry, fluid-inclusion $CO_2$
889 densities and thermodynamic predictions of phase stability ranging from ~700 MPa to 1 GPa.

890 The storage pressures estimated here indicate that the gabbroic nodules were stored below the
891 base of the crust (~16 km), likely at depths between 25.2 – 29.8 km (although a wider, more
892 vertically extensive magma storage zone extending to the base of the crust remains a possibility).
893 Consequently, our new data indicate that there has been persistent, high-pressure (i.e., lithospheric
894 mantle) magma storage beneath Isla Floreana throughout its 2.5 Myrs of magmatic activity, with no
895 petrological evidence indicating sustained crustal-level magma storage ever occurred, contrary to
896 traditional models for ocean island evolution. In fact, our data indicates that there are no substantial
897 differences between the magma storage conditions estimated for the plume-proximal and plume-
898 distal magmatic systems beneath Isla Floreana (Gleeson et al., 2022, 2020a). In addition, our data
899 indicates that the magma storage conditions beneath the plume-proximal stage of Isla Floreana's
900 magmatic history are very different to the mid-crustal storage regions identified beneath present-
901 day volcanic systems in the western Galápagos (Bell et al., 2021; Stock et al., 2018). As a result, our
902 new data supports recent suggestions that the eastern Galápagos volcanic centres do not represent
903 older analogs of the western Galápagos shield volcanoes (Cleary et al., 2020) but instead are
904 characterized by persistent high-pressure magma storage, possibly resulting from the interaction of
905 the Galápagos mantle plume with the nearby Galápagos Spreading Centre. Consequently, we
906 suggest that the proximity of an ocean island to a nearby ridge segment has a substantial influence
907 on the architecture of magma storage (as plume material and melt may be diverted away from the
908 plume centre and towards the ridge axis) and the evolution of magmatic systems.

## 909 ACKNOWLEDGEMENTS

910 MG acknowledges the support and funding from the Royal Commission for the Exhibition of 1851
911 Research Fellowship. EDS analyses were performed with support from NSF EAR/IF 2218698. PW and

CJD acknowledge funding from NSF EAR 2217371 and the Rose Hills Innovator Program. MJS acknowledges support from a Charles Darwin and Galápagos Islands Junior Research Fellowship at Christ's College, Cambridge.

## DATA AVAILABILITY STATEMENT

All data collected during the preparation of this project, including standard analyses, is available via https://github.com/gleesonm1/GleesonEtAl_JPet_2024_supplement and has been archived using Zenodo (https://doi.org/10.5281/zenodo.12746046). In addition, all supplementary data can be found on EarthChem (https://doi.org/10.60520/IEDA/113382). All Python code used to create the figures presented as part of this manuscript can be found in the Zenodo repository listed above. Other code packages used in this study include: PetThermoTools v0.2.29 (github.com/gleesonm1/PetThermoTools); chemMap v0.0.4 (github.com/gleesonm1/chemMap); Thermobar v1.0.43 (github.com/PennyWieser/Thermobar); DiadFit v1.0.2 (github.com/PennyWieser/DiadFit); mineralML v0.0.0.8 (github.com/sarahshi/mineralML); laserTRAM (github.com/jlubbersgeo/laserTRAM-DB); and pyrolite v0.3.5 (github.com/morganjwilliams/pyrolite/tree/develop). Thermodynamic calculations were performed using alphaMELTS for Python v2.3.1 and MAGEMin_C v1.4.9.

## REFERENCES

Argus, D.F., Gordon, R.G., DeMets, C., 2011. Geologically current motion of 56 plates relative to the no-net-rotation reference frame. Geochem. Geophys. Geosystems 12. https://doi.org/10.1029/2011GC003751

Bagnardi, M., Amelung, F., Poland, M.P., 2013. A new model for the growth of basaltic shields based on deformation of Fernandina volcano, Galápagos Islands. Earth Planet. Sci. Lett. 377–378, 358–366. https://doi.org/10.1016/j.epsl.2013.07.016

935 Baxter, R.J.M., Maclennan, J., 2024. Influence of magma flux on magma storage depths along the
936 Reykjanes Ridge. Earth Planet. Sci. Lett. 631, 118633.
937 https://doi.org/10.1016/j.epsl.2024.118633
938 Baxter, R.J.M., Maclennan, J., Neave, D.A., Thordarson, T., 2023. Depth of Magma Storage Under
939 Iceland Controlled by Magma Fluxes. Geochem. Geophys. Geosystems 24, e2022GC010811.
940 https://doi.org/10.1029/2022GC010811
941 Bell, A.F., La Femina, P.C., Ruiz, M., Amelung, F., Bagnardi, M., Bean, C.J., Bernard, B., Ebinger, C.,
942 Gleeson, M., Grannell, J., Hernandez, S., Higgins, M., Liorzou, C., Lundgren, P., Meier, N.J.,
943 Möllhoff, M., Oliva, S.-J., Ruiz, A.G., Stock, M.J., 2021. Caldera resurgence during the 2018
944 eruption of Sierra Negra volcano, Galápagos Islands. Nat. Commun. 12, 1397.
945 https://doi.org/10.1038/s41467-021-21596-4
946 Bell, I.H., Wronski, J., Quoilin, S., Lemort, V., 2014. Pure and Pseudo-pure Fluid Thermophysical
947 Property Evaluation and the Open-Source Thermophysical Property Library CoolProp. Ind.
948 Eng. Chem. Res. 53, 2498–2508. https://doi.org/10.1021/ie4033999
949 Bennett, E.N., Lissenberg, C.J., Cashman, K.V., 2019. The significance of plagioclase textures in mid-
950 ocean ridge basalt (Gakkel Ridge, Arctic Ocean). Contrib. Mineral. Petrol. 174, 49.
951 https://doi.org/10.1007/s00410-019-1587-1
952 Bernard, B., Stock, M.J., Coppola, D., Hidalgo, S., Bagnardi, M., Gibson, S., Hernandez, S., Ramón, P.,
953 Gleeson, M., 2019. Chronology and phenomenology of the 1982 and 2015 Wolf volcano
954 eruptions, Galápagos Archipelago. J. Volcanol. Geotherm. Res. 374, 26–38.
955 https://doi.org/10.1016/j.jvolgeores.2019.02.013
956 Boudoire, G., Brugier, Y.-A., Di Muro, A., Wörner, G., Arienzo, I., Metrich, N., Zanon, V., Braukmüller,
957 N., Kronz, A., Le Moigne, Y., Michon, L., 2019. Eruptive Activity on the Western Flank of Piton
958 de la Fournaise (La Réunion Island, Indian Ocean): Insights on Magma Transfer, Storage and
959 Evolution at an Oceanic Volcanic Island. J. Petrol. 60, 1717–1752.
960 https://doi.org/10.1093/petrology/egz045

961 Bow, C.S., Geist, D.J., 1992. Geology and petrology of Floreana Island, Galapagos Archipelago,
962 Ecuador. J. Volcanol. Geotherm. Res., Special Issue in Honour of Alexander R. McBirney 52,
963 83–105. https://doi.org/10.1016/0377-0273(92)90134-Y
964 Cabral, R.A., Jackson, M.G., Rose-Koga, E.F., Koga, K.T., Whitehouse, M.J., Antonelli, M.A., Farquhar,
965 J., Day, J.M.D., Hauri, E.H., 2013. Anomalous sulphur isotopes in plume lavas reveal deep
966 mantle storage of Archaean crust. Nature 496, 490–493.
967 https://doi.org/10.1038/nature12020
968 Cashman, K.V., Sparks, R.S.J., Blundy, J.D., 2017. Vertically extensive and unstable magmatic systems:
969 A unified view of igneous processes. Science 355, eaag3055.
970 https://doi.org/10.1126/science.aag3055
971 Cherniak, D.J., Liang, Y., 2012. Ti diffusion in natural pyroxene. Geochim. Cosmochim. Acta 98, 31–
972 47. https://doi.org/10.1016/j.gca.2012.09.021
973 Clague, D.A., Bohrson, W.A., 1991. Origin of xenoliths in the trachyte at Puu Waawaa, Hualalai
974 Volcano, Hawaii. Contrib. Mineral. Petrol. 108, 439–452.
975 https://doi.org/10.1007/BF00303448
976 Clague, D.A., Sherrod, D.R., 2014. Growth and degradation of Hawaiian volcanoes (No. 1801–3),
977 Professional Paper. U.S. Geological Survey. https://doi.org/10.3133/pp18013
978 Cleary, Z., Schwartz, D.M., Mittelstaedt, E., Harpp, K., 2020. Dynamic Magma Storage at Near-Ridge
979 Hot Spots: Evidence From New Galápagos Gravity Data. Geochem. Geophys. Geosystems 21,
980 e2019GC008722. https://doi.org/10.1029/2019GC008722
981 Cottaar, S., Lekic, V., 2016. Morphology of seismically slow lower-mantle structures. Geophys. J. Int.
982 207, 1122–1136. https://doi.org/10.1093/gji/ggw324
983 Dayton, K., Gazel, E., Wieser, P., Troll, V.R., Carracedo, J.C., La Madrid, H., Roman, D.C., Ward, J.,
984 Aulinas, M., Geiger, H., Deegan, F.M., Gisbert, G., Perez-Torrado, F.J., 2023. Deep magma
985 storage during the 2021 La Palma eruption. Sci. Adv. 9, eade7641.
986 https://doi.org/10.1126/sciadv.ade7641

DeVitre, C.L., Dayton, K., Gazel, E., Pamukçu, A., Gaetani, G., Wieser, P.E., 2023a. Laser heating effect on Raman analysis of CO2 co-existing as liquid and vapor in olivine-hosted melt inclusion bubbles. Volcanica 6, 201–219. https://doi.org/10.30909/vol.06.02.201219

DeVitre, C.L., Gazel, E., Ramalho, R.S., Venugopal, S., Steele-MacInnis, M., Hua, J., Allison, C.M., Moore, L.R., Carracedo, J.C., Monteleone, B., 2023b. Oceanic intraplate explosive eruptions fed directly from the mantle. Proc. Natl. Acad. Sci. 120, e2302093120. https://doi.org/10.1073/pnas.2302093120

DeVitre, C.L., Wieser, P.E., 2024. Reliability of Raman analyses of CO2-rich fluid inclusions as a geobarometer at Kīlauea. Geochem. Perspect. Lett. 29, 1–8. https://doi.org/10.7185/geochemlet.2404

Duan, Z., Zhang, Z., 2006. Equation of state of the H2O, CO2, and H2O–CO2 systems up to 10 GPa and 2573.15 K: Molecular dynamics simulations with ab initio potential surface. Geochim. Cosmochim. Acta 70, 2311–2324. https://doi.org/10.1016/j.gca.2006.02.009

Faak, K., Coogan, L.A., Chakraborty, S., 2014. A new Mg-in-plagioclase geospeedometer for the determination of cooling rates of mafic rocks. Geochim. Cosmochim. Acta 140, 691–707. https://doi.org/10.1016/j.gca.2014.06.005

Feighner, M.A., Richards, M.A., 1994. Lithospheric structure and compensation mechanisms of the Galápagos Archipelago. J. Geophys. Res. Solid Earth 99, 6711–6729. https://doi.org/10.1029/93JB03360

French, S.W., Romanowicz, B., 2015. Broad plumes rooted at the base of the Earth's mantle beneath major hotspots. Nature 525, 95–99. https://doi.org/10.1038/nature14876

Frezzotti, M.L., Burke, E.A.J., De Vivo, B., Stefanini, B., Villa, I.M., 1992. Mantle fluids in pyroxenite nodules from Salt Lake Crater (Oahu, Hawaii). Eur. J. Mineral. 4, 1137–1153.

Gao, R., Lassiter, J.C., Barnes, J.D., Clague, D.A., Bohrson, W.A., 2016. Geochemical investigation of Gabbroic Xenoliths from Hualalai Volcano: Implications for lower oceanic crust accretion and

1012 Hualalai Volcano magma storage system. Earth Planet. Sci. Lett. 442, 162–172.
1013 https://doi.org/10.1016/j.epsl.2016.02.043
1014 Gao, R., Lassiter, J.C., Clague, D.A., Bohrson, W.A., 2022. Evolution of Hawaiian Volcano Magmatic
1015 Plumbing System and Implications for Melt/Edifice and Melt/Lithosphere Interaction:
1016 Constraints from Hualālai Xenoliths. J. Petrol. 63, egac091.
1017 https://doi.org/10.1093/petrology/egac091
1018 Geist, D., Bergantz, G., Chadwick Jr., W.W., 2014. Galápagos Magma Chambers, in: The Galápagos.
1019 American Geophysical Union (AGU), pp. 55–69.
1020 https://doi.org/10.1002/9781118852538.ch5
1021 Geist, D., Howard, K.A., Larson P., 1995. The Generation of Oceanic Rhyolites by Crystal
1022 Fractionation: the Basalt-Rhyolite Association at Volcán Alcedo, Galápagos Archipelago. J.
1023 Petrol. 36, 965–982. https://doi.org/10.1093/petrology/36.4.965
1024 Geist, D., NAUMANN, T.R., STANDISH, J.J., KURZ, M.D., HARPP, K.S., WHITE, W.M., FORNARI, D.J.,
1025 2005. Wolf Volcano, Galápagos Archipelago: Melting and Magmatic Evolution at the Margins
1026 of a Mantle Plume. J. Petrol. 46, 2197–2224. https://doi.org/10.1093/petrology/egi052
1027 Geist, D., White, W.M., Albarede, F., Harpp, K., Reynolds, R., Blichert-Toft, J., Kurz, M.D., 2002.
1028 Volcanic evolution in the Galápagos: The dissected shield of Volcan Ecuador. Geochem.
1029 Geophys. Geosystems 3, 1 of 32–32 32. https://doi.org/10.1029/2002GC000355
1030 Geist, D.J., White, W.M., McBirney, A.R., 1988. Plume-asthenosphere mixing beneath the Galapagos
1031 archipelago. Nature 333, 657–660. https://doi.org/10.1038/333657a0
1032 Ghiorso, M.S., Hirschmann, M.M., Reiners, P.W., Kress III, V.C., 2002. The pMELTS: A revision of
1033 MELTS for improved calculation of phase relations and major element partitioning related to
1034 partial melting of the mantle to 3 GPa. Geochem. Geophys. Geosystems 3, 1–35.
1035 https://doi.org/10.1029/2001GC000217

1036 Gibson, S.A., Geist, D., 2010. Geochemical and geophysical estimates of lithospheric thickness
1037 variation beneath Galápagos. Earth Planet. Sci. Lett. 300, 275–286.
1038 https://doi.org/10.1016/j.epsl.2010.10.002
1039 Gibson, S.A., Geist, D.G., Day, J.A., Dale, C.W., 2012. Short wavelength heterogeneity in the
1040 Galápagos plume: Evidence from compositionally diverse basalts on Isla Santiago. Geochem.
1041 Geophys. Geosystems 13. https://doi.org/10.1029/2012GC004244
1042 Gibson, S.A., Geist, D.J., Richards, M.A., 2015. Mantle plume capture, anchoring, and outflow during
1043 Galápagos plume-ridge interaction. Geochem. Geophys. Geosystems 16, 1634–1655.
1044 https://doi.org/10.1002/2015GC005723
1045 Gleeson, M.L.M., Gibson, S.A., 2021. Insights Into the Nature of Plume-Ridge Interaction and Outflux
1046 of H2O From the Galápagos Spreading Center. Geochem. Geophys. Geosystems 22,
1047 e2020GC009560. https://doi.org/10.1029/2020GC009560
1048 Gleeson, M.L.M., Gibson, S.A., 2019. Crustal controls on apparent mantle pyroxenite signals in
1049 ocean-island basalts. Geology 47, 321–324. https://doi.org/10.1130/G45759.1
1050 Gleeson, M.L.M., Gibson, S.A., Stock, M.J., 2022. Constraints on the behaviour and content of
1051 volatiles in Galápagos magmas from melt inclusions and nominally anhydrous minerals.
1052 Geochim. Cosmochim. Acta 319, 168–190. https://doi.org/10.1016/j.gca.2021.11.005
1053 Gleeson, M.L.M., Gibson, S.A., Stock, M.J., 2020a. Upper Mantle Mush Zones beneath Low Melt Flux
1054 Ocean Island Volcanoes: Insights from Isla Floreana, Galápagos. J. Petrol. 61, egaa094.
1055 https://doi.org/10.1093/petrology/egaa094
1056 Gleeson, M.L.M., Gibson, S.A., Williams, H.M., 2020b. Novel insights from Fe-isotopes into the
1057 lithological heterogeneity of Ocean Island Basalts and plume-influenced MORBs. Earth
1058 Planet. Sci. Lett. 535, 116114. https://doi.org/10.1016/j.epsl.2020.116114
1059 Gleeson, M.L.M., Soderman, C., Matthews, S., Cottaar, S., Gibson, S., 2021. Geochemical Constraints
1060 on the Structure of the Earth's Deep Mantle and the Origin of the LLSVPs. Geochem.
1061 Geophys. Geosystems 22, e2021GC009932. https://doi.org/10.1029/2021GC009932

1062 Grove, T.L., Baker, M.B., Kinzler, R.J., 1984. Coupled CaAl-NaSi diffusion in plagioclase feldspar:
1063 Experiments and applications to cooling rate speedometry. Geochim. Cosmochim. Acta 48,
1064 2113–2121. https://doi.org/10.1016/0016-7037(84)90391-0
1065 Hagiwara, Y., Torimoto, J., Yamamoto, J., 2019. Thermoelastic equilibrium of fluid inclusion–host
1066 mineral systems under homogenization measurement. J. Mineral. Petrol. Sci. 114, 149–154.
1067 https://doi.org/10.2465/jmps.181109b
1068 Hansteen, T.H., Klügel, A., 2008. Fluid Inclusion Thermobarometry as a Tracer for Magmatic
1069 Processes. Rev. Mineral. Geochem. 69, 143–177. https://doi.org/10.2138/rmg.2008.69.5
1070 Harpp, K.S., Geist, D.J., 2018. The Evolution of Galápagos Volcanoes: An Alternative Perspective.
1071 Front. Earth Sci. 6. https://doi.org/10.3389/feart.2018.00050
1072 Harpp, K.S., Geist, D.J., Koleszar, A.M., Christensen, B., Lyons, J., Sabga, M., Rollins, N., 2014. The
1073 Geology and Geochemistry of Isla Floreana, Galápagos, in: The Galápagos. American
1074 Geophysical Union (AGU), pp. 71–117. https://doi.org/10.1002/9781118852538.ch6
1075 Harpp, K.S., Weis, D., 2020. Insights Into the Origins and Compositions of Mantle Plumes: A
1076 Comparison of Galápagos and Hawai'i. Geochem. Geophys. Geosystems 21,
1077 e2019GC008887. https://doi.org/10.1029/2019GC008887
1078 Harpp, K.S., White, W.M., 2001. Tracing a mantle plume: Isotopic and trace element variations of
1079 Galápagos seamounts. Geochem. Geophys. Geosystems 2.
1080 https://doi.org/10.1029/2000GC000137
1081 Herzberg, C., Cabral, R.A., Jackson, M.G., Vidito, C., Day, J.M.D., Hauri, E.H., 2014. Phantom Archean
1082 crust in Mangaia hotspot lavas and the meaning of heterogeneous mantle. Earth Planet. Sci.
1083 Lett. 396, 97–106. https://doi.org/10.1016/j.epsl.2014.03.065
1084 Higgins, O.J., Stock, M., 2024. A new calibration of the OPAM thermobarometer for anhydrous and
1085 hydrous mafic systems.

1086 Hoernle, K., Werner, R., Morgan, J.P., Garbe-Schönberg, D., Bryce, J., Mrazek, J., 2000. Existence of
1087 complex spatial zonation in the Galápagos plume. Geology 28, 435–438.
1088 https://doi.org/10.1130/0091-7613(2000)28<435:EOCSZI>2.0.CO;2
1089 Holland, T.J.B., Green, E.C.R., Powell, R., 2018. Melting of Peridotites through to Granites: A Simple
1090 Thermodynamic Model in the System KNCFMASHTOCr. J. Petrol. 59, 881–900.
1091 https://doi.org/10.1093/petrology/egy048
1092 Holness, M.B., Stock, M.J., Geist, D., 2019. Magma chambers versus mush zones: constraining the
1093 architecture of sub-volcanic plumbing systems from microstructural analysis of crystalline
1094 enclaves. Philos. Transact. A Math. Phys. Eng. Sci. 377, 20180006.
1095 https://doi.org/10.1098/rsta.2018.0006
1096 Hooft, E.E.E., Toomey, D.R., Solomon, S.C., 2003. Anomalously thin transition zone beneath the
1097 Galápagos hotspot. Earth Planet. Sci. Lett. 216, 55–64. https://doi.org/10.1016/S0012-
1098 821X(03)00517-X
1099 Horn, E.L., Taylor, R.N., Gernon, T.M., Stock, M.J., Farley, E.M.R., 2022. Composition and Petrology of
1100 a Mush-Bearing Magma Reservoir beneath Tenerife. J. Petrol. 63, egac095.
1101 https://doi.org/10.1093/petrology/egac095
1102 Jackson, M.G., Hart, S.R., Saal, A.E., Shimizu, N., Kurz, M.D., Blusztajn, J.S., Skovgaard, A.C., 2008.
1103 Globally elevated titanium, tantalum, and niobium (TITAN) in ocean island basalts with high
1104 3He/4He. Geochem. Geophys. Geosystems 9. https://doi.org/10.1029/2007GC001876
1105 Jochum, K.P., Nohl, U., Herwig, K., Lammel, E., Stoll, B., Hofmann, A.W., 2005. GeoReM: A New
1106 Geochemical Database for Reference Materials and Isotopic Standards. Geostand.
1107 Geoanalytical Res. 29, 333–338. https://doi.org/10.1111/j.1751-908X.2005.tb00904.x
1108 Koppers, A.A.P., Becker, T.W., Jackson, M.G., Konrad, K., Müller, R.D., Romanowicz, B., Steinberger,
1109 B., Whittaker, J.M., 2021. Mantle plumes and their role in Earth processes. Nat. Rev. Earth
1110 Environ. 2, 382–401. https://doi.org/10.1038/s43017-021-00168-6

1111 Kunz, O., Wagner, W., 2012. The GERG-2008 Wide-Range Equation of State for Natural Gases and
1112 Other Mixtures: An Expansion of GERG-2004. J. Chem. Eng. Data 57, 3032–3091.
1113 https://doi.org/10.1021/je300655b
1114 Kurz, M.D., Curtice, J., Fornari, D., Geist, D., Moreira, M., 2009. Primitive neon from the center of the
1115 Galápagos hotspot. Earth Planet. Sci. Lett. 286, 23–34.
1116 https://doi.org/10.1016/j.epsl.2009.06.008
1117 Kurz, M.D., Geist, D., 1999. Dynamics of the Galapagos hotspot from helium isotope geochemistry.
1118 Geochim. Cosmochim. Acta 63, 4139–4156. https://doi.org/10.1016/S0016-7037(99)00314-
1119 2
1120 Lamadrid, H.M., Moore, L.R., Moncada, D., Rimstidt, J.D., Burruss, R.C., Bodnar, R.J., 2017.
1121 Reassessment of the Raman CO2 densimeter. Chem. Geol. 450, 210–222.
1122 https://doi.org/10.1016/j.chemgeo.2016.12.034
1123 Lerner, A.H., Wallace, P.J., Shea, T., Mourey, A.J., Kelly, P.J., Nadeau, P.A., Elias, T., Kern, C., Clor, L.E.,
1124 Gansecki, C., Lee, R.L., Moore, L.R., Werner, C.A., 2021. The petrologic and degassing
1125 behavior of sulfur and other magmatic volatiles from the 2018 eruption of Kīlauea, Hawai'i:
1126 melt concentrations, magma storage depths, and magma recycling. Bull. Volcanol. 83, 43.
1127 https://doi.org/10.1007/s00445-021-01459-y
1128 Lissenberg, C.J., MacLeod, C.J., 2016. A Reactive Porous Flow Control on Mid-ocean Ridge Magmatic
1129 Evolution. J. Petrol. 57, 2195–2220. https://doi.org/10.1093/petrology/egw074
1130 Lubbers, J., Kent, A.J., Russo, C., 2021. LaserTRAM-DB: A Time Resolved Analysis Module for the
1131 complete reduction of Laser Ablation Inductively Coupled Plasma Mass Spectrometry data.
1132 Lyons, J., Geist, D., Harpp, K., Diefenbach, B., Olin, P., Vervoort, J., 2007. Crustal growth by magmatic
1133 overplating in the Galápagos. Geology 35, 511–514.
1134 Maclennan, J., 2019. Mafic tiers and transient mushes: evidence from Iceland. Philos. Trans. R. Soc.
1135 Math. Phys. Eng. Sci. 377, 20180021. https://doi.org/10.1098/rsta.2018.0021

1136 Mahr, J., Harpp, K.S., Kurz, M.D., Geist, D., Bercovici, H., Pimentel, R., Cleary, Z., Córdova Aguilar,
1137 M.D., 2016. Rejuvenescent Volcanism on San Cristóbal Island, Galápagos: A Late "Plumer"
1138 2016, V53C-3119.
1139 Matthews, S., Wong, K., Shorttle, O., Edmonds, M., Maclennan, J., 2021. Do Olivine Crystallization
1140 Temperatures Faithfully Record Mantle Temperature Variability? Geochem. Geophys.
1141 Geosystems 22. https://doi.org/10.1029/2020GC009157
1142 Métrich, N., Zanon, V., Créon, L., Hildenbrand, A., Moreira, M., Marques, F.O., 2014. Is the 'Azores
1143 Hotspot' a Wetspot? Insights from the Geochemistry of Fluid and Melt Inclusions in Olivine
1144 of Pico Basalts. J. Petrol. 55, 377–393. https://doi.org/10.1093/petrology/egt071
1145 Mittal, T., Richards, M.A., 2017. Plume-ridge interaction via melt channelization at Galápagos and
1146 other near-ridge hotspot provinces. Geochem. Geophys. Geosystems 18, 1711–1738.
1147 https://doi.org/10.1002/2016GC006454
1148 Mittelstaedt, E., Soule, A.S., Harpp, K.S., Fornari, D., 2014. Variations in Crustal Thickness, Plate
1149 Rigidity, and Volcanic Processes Throughout the Northern Galápagos Volcanic Province, in:
1150 The Galápagos. American Geophysical Union (AGU), pp. 263–284.
1151 https://doi.org/10.1002/9781118852538.ch14
1152 Mittelstaedt, E., Soule, S., Harpp, K., Fornari, D., McKee, C., Tivey, M., Geist, D., Kurz, M.D., Sinton,
1153 C., Mello, C., 2012. Multiple expressions of plume-ridge interaction in the Galápagos:
1154 Volcanic lineaments and ridge jumps. Geochem. Geophys. Geosystems 13.
1155 https://doi.org/10.1029/2012GC004093
1156 Morrow, T.A., Mittelstaedt, E.L., 2021. Quantifying Periodic Variations in Hotspot Melt Production. J.
1157 Geophys. Res. Solid Earth 126, e2021JB021726. https://doi.org/10.1029/2021JB021726
1158 Naumann, T., Geist, D., 2000. Physical volcanology and structural development of Cerro Azul
1159 Volcano, Isabela Island, Galápagos: implications for the development of Galápagos-type
1160 shield volcanoes. Bull. Volcanol. 61, 497–514. https://doi.org/10.1007/s004450050001

1161 Naumann, T.R., Geist, D.J., 1999. Generation of alkalic basalt by crystal fractionation of tholeiitic
1162 magma. Geology 27, 423–426. https://doi.org/10.1130/0091-
1163 7613(1999)027<0423:GOABBC>2.3.CO;2
1164 Neal, C.A., Brantley, S.R., Antolik, L., Babb, J.L., Burgess, M., Calles, K., Cappos, M., Chang, J.C.,
1165 Conway, S., Desmither, L., Dotray, P., Elias, T., Fukunaga, P., Fuke, S., Johanson, I.A.,
1166 Kamibayashi, K., Kauahikaua, J., Lee, R.L., Pekalib, S., Miklius, A., Million, W., Moniz, C.J.,
1167 Nadeau, P.A., Okubo, P., Parcheta, C., Patrick, M.R., Shiro, B., Swanson, D.A., Tollett, W.,
1168 Trusdell, F., Younger, E.F., Zoeller, M.H., Montgomery-Brown, E.K., Anderson, K.R., Poland,
1169 M.P., Ball, J.L., Bard, J., Coombs, M., Dietterich, H.R., Kern, C., Thelen, W.A., Cervelli, P.F.,
1170 Orr, T., Houghton, B.F., Gansecki, C., Hazlett, R., Lundgren, P., Diefenbach, A.K., Lerner, A.H.,
1171 Waite, G., Kelly, P., Clor, L., Werner, C., Mulliken, K., Fisher, G., Damby, D., 2019. The 2018
1172 rift eruption and summit collapse of Kīlauea Volcano. Science 363, 367–374.
1173 https://doi.org/10.1126/science.aav7046
1174 Peterson, M.E., Saal, A.E., Kurz, M.D., Hauri, E.H., Blusztajn, J.S., Harpp, K.S., Werner, R., Geist, D.J.,
1175 2017. Submarine Basaltic Glasses from the Galapagos Archipelago: Determining the Volatile
1176 Budget of the Mantle Plume. J. Petrol. 58, 1419–1450.
1177 https://doi.org/10.1093/petrology/egx059
1178 Putirka, K.D., 2008. Thermometers and Barometers for Volcanic Systems. Rev. Mineral. Geochem.
1179 69, 61–120. https://doi.org/10.2138/rmg.2008.69.3
1180 Reynolds, R.W., Geist, D.J., 1995. Petrology of lavas from Sierra Negra volcano, Isabela Island,
1181 Galápagos archipelago. J. Geophys. Res. Solid Earth 100, 24537–24553.
1182 https://doi.org/10.1029/95JB02809
1183 Riel, N., Kaus, B.J.P., Green, E.C.R., Berlie, N., 2022. MAGEMin, an Efficient Gibbs Energy Minimizer:
1184 Application to Igneous Systems. Geochem. Geophys. Geosystems 23, e2022GC010427.
1185 https://doi.org/10.1029/2022GC010427

1186 Sandoval-Velasquez, A., Rizzo, A.L., Casetta, F., Ntaflos, T., Aiuppa, A., Alonso, M., Padrón, E.,
1187 Pankhurst, M.J., Mundl-Petermeier, A., Zanon, V., Pérez, N.M., 2023. The noble gas signature
1188 of the 2021 Tajogaite eruption (La Palma, Canary Islands). J. Volcanol. Geotherm. Res. 443,
1189 107928. https://doi.org/10.1016/j.jvolgeores.2023.107928
1190 Sanfilippo, A., MacLeod, C.J., Tribuzio, R., Lissenberg, C.J., Zanetti, A., 2020. Early-Stage Melt-Rock
1191 Reaction in a Cooling Crystal Mush Beneath a Slow-Spreading Mid-Ocean Ridge (IODP Hole
1192 U1473A, Atlantis Bank, Southwest Indian Ridge). Front. Earth Sci. 8.
1193 https://doi.org/10.3389/feart.2020.579138
1194 Schwartz, D.M., Harpp, K.S., Mittelstaedt, E.L., 2014. The Interplay Between Deformation and
1195 Volcanism on Santa Cruz Island, Galápagos: A Multidisciplinary Study Using Structural,
1196 Geophysical, and Geochronological Analyses of Faults and Lavas 2014, V41B-4802.
1197 Shi, S.C., Wieser, P.E., Toth, N., Antoshechkina, P.M., Lehnert, K., 2024. MIN-ML: Leveraging Machine
1198 Learning for Probabilistic Mineral Classification in Geochemical Databases. Presented at the
1199 AGU Fall Meetings.
1200 Smith, P.M., Asimow, P.D., 2005. Adiabat_1ph: A new public front-end to the MELTS, pMELTS, and
1201 pHMELTS models. Geochem. Geophys. Geosystems 6.
1202 https://doi.org/10.1029/2004GC000816
1203 Sobolev, A.V., Hofmann, A.W., Kuzmin, D.V., Yaxley, G.M., Arndt, N.T., Chung, S.-L., Danyushevsky,
1204 L.V., Elliott, T., Frey, F.A., Garcia, M.O., Gurenko, A.A., Kamenetsky, V.S., Kerr, A.C.,
1205 Krivolutskaya, N.A., Matvienkov, V.V., Nikogosian, I.K., Rocholl, A., Sigurdsson, I.A.,
1206 Sushchevskaya, N.M., Teklay, M., 2007. The Amount of Recycled Crust in Sources of Mantle-
1207 Derived Melts. Science 316, 412–417. https://doi.org/10.1126/science.1138113
1208 Span, R., Wagner, W., 1996. A New Equation of State for Carbon Dioxide Covering the Fluid Region
1209 from the Triple-Point Temperature to 1100 K at Pressures up to 800 MPa. J. Phys. Chem. Ref.
1210 Data 25, 1509–1596. https://doi.org/10.1063/1.555991

1211 Sparks, R.S.J., Annen, C., Blundy, J.D., Cashman, K.V., Rust, A.C., Jackson, M.D., 2019. Formation and
1212 dynamics of magma reservoirs. Philos. Trans. R. Soc. Math. Phys. Eng. Sci. 377, 20180019.
1213 https://doi.org/10.1098/rsta.2018.0019
1214 Stock, M.J., Bagnardi, M., Neave, D.A., Maclennan, J., Bernard, B., Buisman, I., Gleeson, M.L.M.,
1215 Geist, D., 2018. Integrated Petrological and Geophysical Constraints on Magma System
1216 Architecture in the Western Galápagos Archipelago: Insights From Wolf Volcano. Geochem.
1217 Geophys. Geosystems 19, 4722–4743. https://doi.org/10.1029/2018GC007936
1218 Stock, M.J., Geist, D., Neave, D.A., Gleeson, M.L., Bernard, B., Howard, K.A., Buisman, I., Maclennan,
1219 J., 2020. Cryptic evolved melts beneath monotonous basaltic shield volcanoes in the
1220 Galápagos Archipelago. Nat. Commun. 11, 3767.
1221 Stock, M.J., Taylor, R.N., Gernon, T.M., 2012. Triggering of major eruptions recorded by actively
1222 forming cumulates. Sci. Rep. 2, 731. https://doi.org/10.1038/srep00731
1223 Sun, C., Liang, Y., 2012. Distribution of REE between clinopyroxene and basaltic melt along a mantle
1224 adiabat: effects of major element composition, water, and temperature. Contrib. Mineral.
1225 Petrol. 163, 807–823. https://doi.org/10.1007/s00410-011-0700-x
1226 Sun, C., Lissenberg, C.J., 2018. Formation of fast-spreading lower oceanic crust as revealed by a new
1227 Mg–REE coupled geospeedometer. Earth Planet. Sci. Lett. 487, 165–178.
1228 https://doi.org/10.1016/j.epsl.2018.01.032
1229 Sun, S. -s., McDonough, W.F., 1989. Chemical and isotopic systematics of oceanic basalts:
1230 implications for mantle composition and processes. Geol. Soc. Lond. Spec. Publ. 42, 313–
1231 345. https://doi.org/10.1144/GSL.SP.1989.042.01.19
1232 Van Ark, E., Lin, J., 2004. Time variation in igneous volume flux of the Hawaii-Emperor hot spot
1233 seamount chain. J. Geophys. Res. Solid Earth 109. https://doi.org/10.1029/2003JB002949
1234 Vidal, V., Bonneville, A., 2004. Variations of the Hawaiian hot spot activity revealed by variations in
1235 the magma production rate. J. Geophys. Res. Solid Earth 109.
1236 https://doi.org/10.1029/2003JB002559

1237 Vidito, C., Herzberg, C., Gazel, E., Geist, D., Harpp, K., 2013. Lithological structure of the Galápagos
1238 Plume. Geochem. Geophys. Geosystems 14, 4214–4240.
1239 https://doi.org/10.1002/ggge.20270
1240 Villagómez, D.R., Toomey, D.R., Geist, D.J., Hooft, E.E.E., Solomon, S.C., 2014. Mantle flow and
1241 multistage melting beneath the Galápagos hotspot revealed by seismic imaging. Nat. Geosci.
1242 7, 151–156. https://doi.org/10.1038/ngeo2062
1243 Wanamaker, B.J., Evans, B., 1989. Mechanical re-equilibration of fluid inclusions in San Carlos olivine
1244 by power-law creep. Contrib. Mineral. Petrol. 102, 102–111.
1245 https://doi.org/10.1007/BF01160194
1246 Weis, D., Harpp, K.S., Harrison, L.N., Boyet, M., Chauvel, C., Farnetani, C.G., Finlayson, V.A., Lee,
1247 K.K.M., Parai, R., Shahar, A., Williamson, N.M.B., 2023. Earth's mantle composition revealed
1248 by mantle plumes. Nat. Rev. Earth Environ. 4, 604–625. https://doi.org/10.1038/s43017-
1249 023-00467-0
1250 Wessel, P., 2016. Regional–residual separation of bathymetry and revised estimates of Hawaii plume
1251 flux. Geophys. J. Int. 204, 932–947. https://doi.org/10.1093/gji/ggv472
1252 White, W.M., McBirney, A.R., Duncan, R.A., 1993. Petrology and geochemistry of the Galápagos
1253 Islands: Portrait of a pathological mantle plume. J. Geophys. Res. Solid Earth 98, 19533–
1254 19563. https://doi.org/10.1029/93JB02018
1255 Whitty, R.C.W., Ilyinskaya, E., Mason, E., Wieser, P.E., Liu, E.J., Schmidt, A., Roberts, T., Pfeffer, M.A.,
1256 Brooks, B., Mather, T.A., Edmonds, M., Elias, T., Schneider, D.J., Oppenheimer, C., Dybwad,
1257 A., Nadeau, P.A., Kern, C., 2020. Spatial and Temporal Variations in SO2 and PM2.5 Levels
1258 Around Kīlauea Volcano, Hawai'i During 2007–2018. Front. Earth Sci. 8.
1259 https://doi.org/10.3389/feart.2020.00036
1260 Wieser, P., Petrelli, M., Lubbers, J., Wieser, E., Ozaydin, S., Kent, A., Till, C., 2022. Thermobar: An
1261 open-source Python3 tool for thermobarometry and hygrometry. Volcanica 5, 349–384.
1262 https://doi.org/10.30909/vol.05.02.349384

Wieser, P.E., DeVitre, C., 2024. DiadFit: An open-source Python3 tool for peak fitting of Raman data from silicate melts and CO2 fluids. Volcanica 7, 335–359. https://doi.org/10.30909/vol.07.01.335359

Wieser, P.E., Gleeson, M.L.M., Matthews, S., DeVitre, C., Gazel, E., 2025. Determining the pressure-temperature-composition (P-T-X) conditions of magma storage, in: Anbar, A., Weis, D. (Eds.), Treatise on Geochemistry (Third Edition). Elsevier, Oxford, pp. 83–151. https://doi.org/10.1016/B978-0-323-99762-1.00024-3

Williams, M.J., Schoneveld, L., Mao, Y., Klump, J., Gosses, J., Dalton, H., Bath, A., Barnes, S., 2020. pyrolite: Python for geochemistry. J. Open Source Softw. 5, 2314. https://doi.org/10.21105/joss.02314

Wilson, D.S., Hey, R.N., 1995. History of rift propagation and magnetization intensity for the Cocos-Nazca sspreading Center. J. Geophys. Res. Solid Earth 100, 10041–10056. https://doi.org/10.1029/95JB00762

Wilson, E.L., Harpp, K.S., Schwartz, D.M., Van Kirk, R., 2022. The Geochemical Evolution of Santa Cruz Island, Galápagos Archipelago. Front. Earth Sci. 10. https://doi.org/10.3389/feart.2022.845544

Wilson, G., Wilson, T.M., Deligne, N.I., Cole, J.W., 2014. Volcanic hazard impacts to critical infrastructure: A review. J. Volcanol. Geotherm. Res. 286, 148–182. https://doi.org/10.1016/j.jvolgeores.2014.08.030

# Supplementary Material: Persistent high-pressure magma storage beneath a near-ridge ocean island volcano (Isla Floreana, Galápagos)

January 26, 2025

Matthew Gleeson[1,2*], Penny Wieser[1], Charlotte L. DeVitre[1], Sarah C. Shi[1,3], Marc-Alban Millet[2], Duncan D. Muir[2], Michael J. Stock[4], and Johan Lissenberg[2]

[1]Department of Earth and Planetary Science, University of California Berkeley, McCone Hall, Berkeley, CA 94720, USA
[2]School of Earth and Environmental Sciences, Cardiff University, Main Building, Park Place, CF10 3AT, UK.
[3]Lamont-Doherty Earth Observatory, Columbia University. New York, NY USA
[4]Discipline of Geology, School of Natural Sciences, Trinity College Dublin, Dublin 02, Ireland

[*]Corresponding author: gleesonm@berkeley.edu

Supplementary Data and code associated with this project can be found in the associated Zenodo Repository: https://doi.org/10.5281/zenodo.12746046 and EarthChem repository: https://doi.org/10.60520/IEDA/113382

# Volcanic and chemical divides

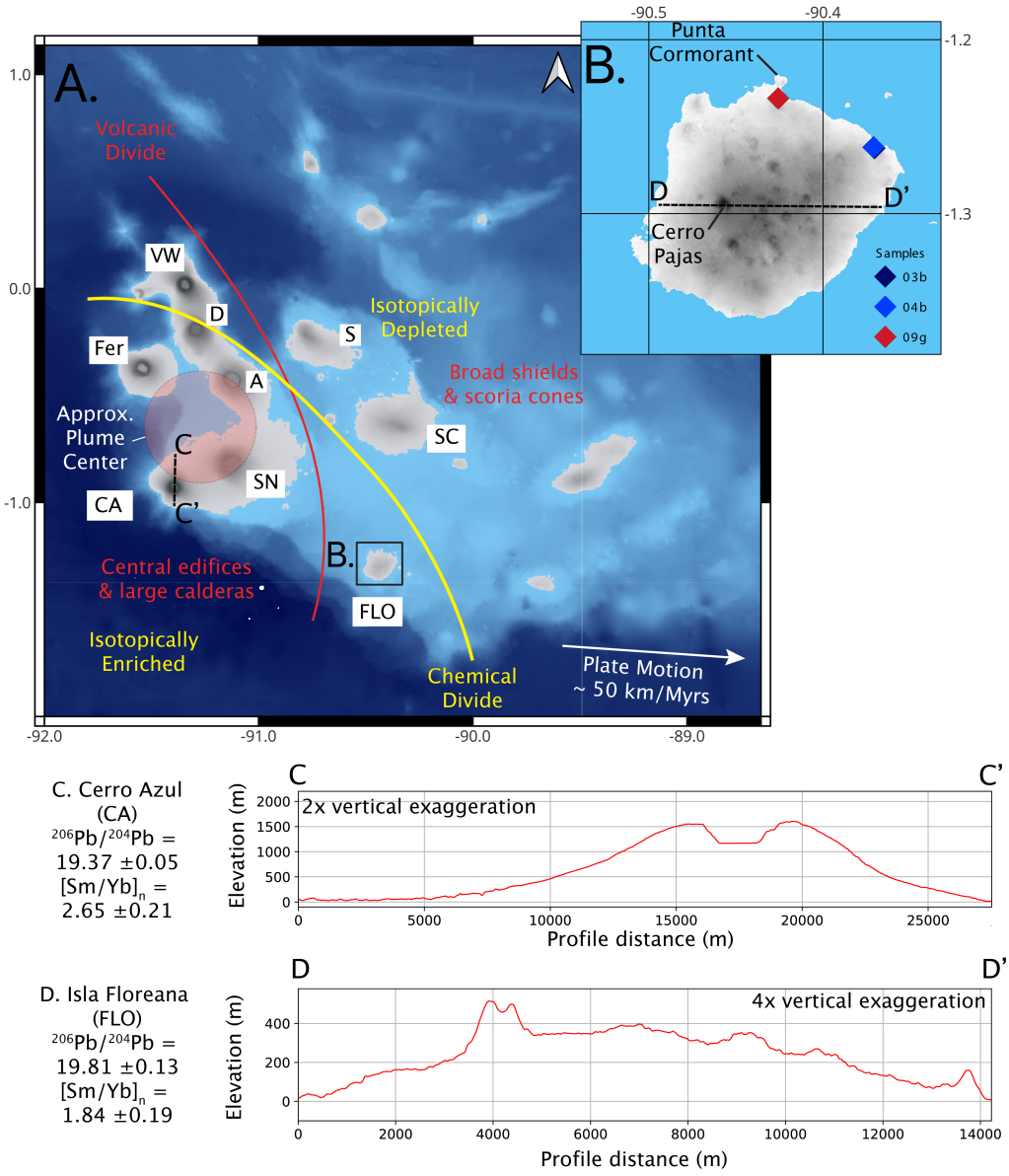


Fig. S.1: A copy of Figure 1 used in the main text. This figure here also contains topographic profiles across Volcán Cerro Azul and Isla Floreana, showing the different morphologies of volcanic systems in the western and eastern Galápagos, respectively.

# Standard analyses, precision and accuracy

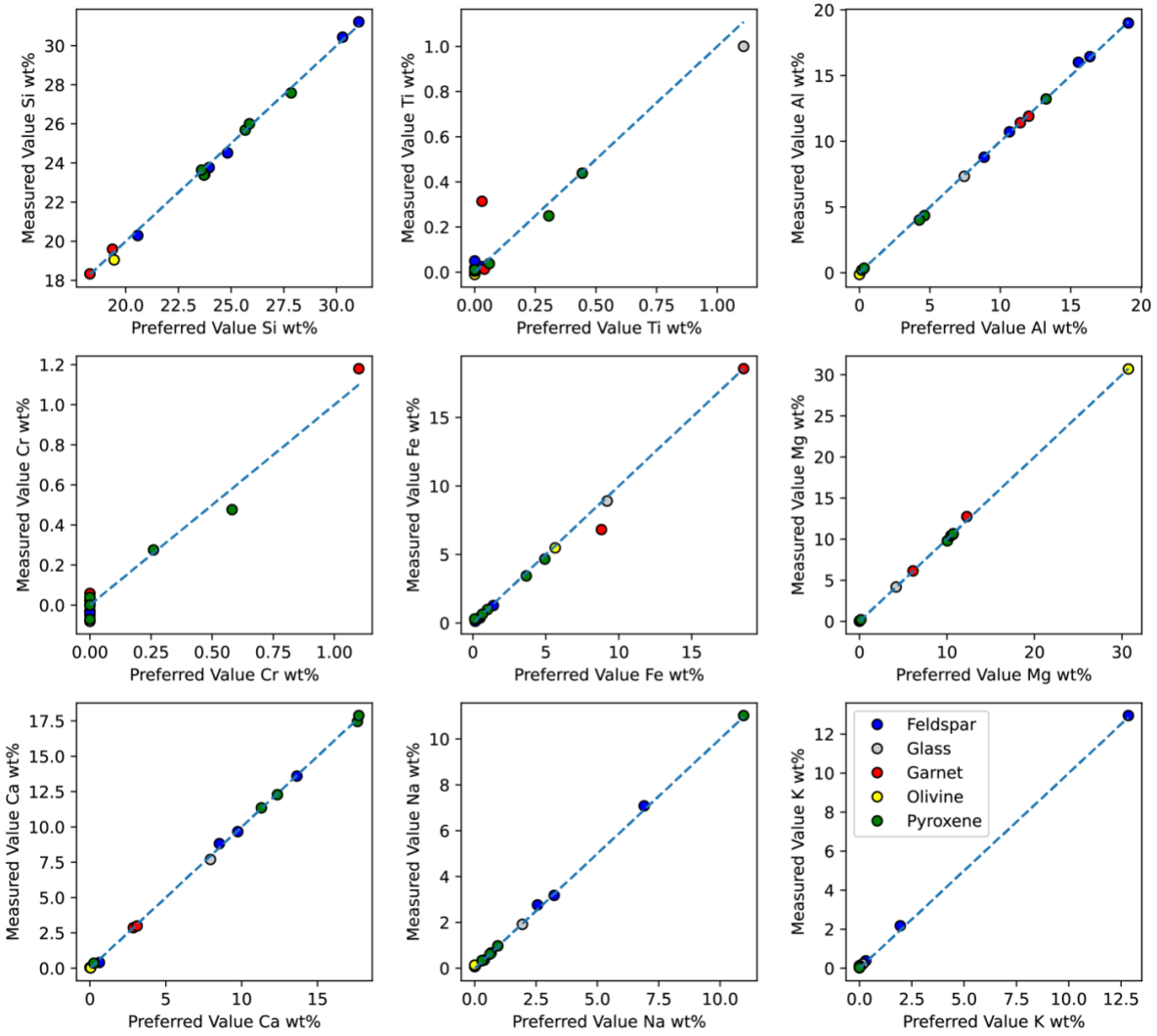


Fig. S.2: Comparison of measured and expected standard values for quantitative EDS mapping. Measured values are taken as the mean concentration of that element across the entire sample map. Preferred values represent the given value for each standard by Astimex or the Smithsonina. We note that our EDS maps detected significant $TiO_2$ in a Pyrope Garnet standard where only 0.04 wt% $TiO_2$ is reported by Astimex. This sample also reveals a slight offset in the measured and preferred $FeO_t$ values, which is not seen in our other standards.

Mineral major and minor element chemistry - across spatial scales ranging from full sample maps to individual point analyses - was collected by Energy Dispersive Spectrometry (EDS) using 2 X-Max 150 EDS detectors on the Zeiss Sigma HD Field Emission Gun Scanning Electron

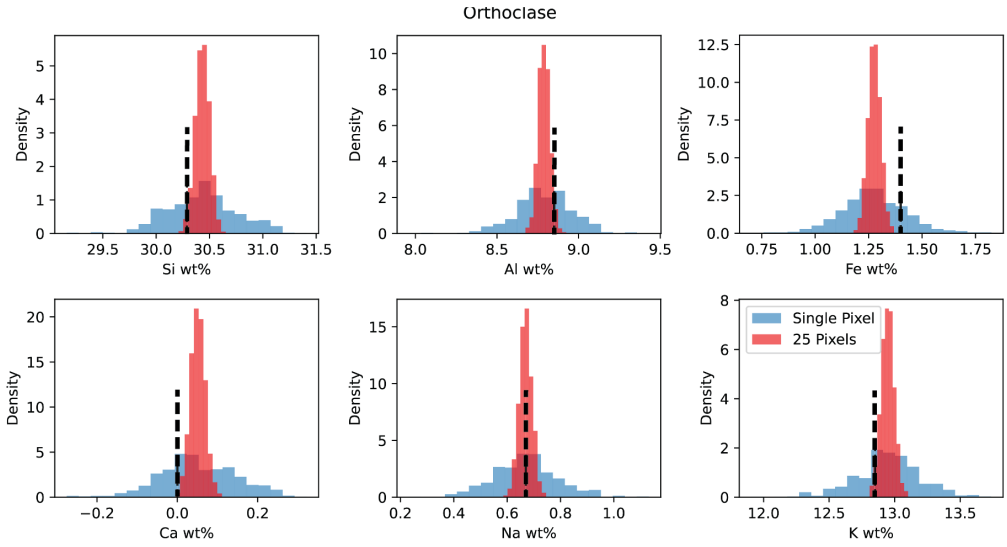


Fig. S.3: Comparison of standard map data to preferred standard values for Orthoclase. Blue histograms represent the concentrations determined from each individual pixel of the maps. Red histograms represent 1000 iterations of randomly sampled 5-by-5 pixel areas. Black dashed lines represent the preferred standard values.

Microscope (FEG-SEM) at Cardiff University. These data were then supplemented by EDS and Wavelength Dispersive Spectrometry (WDS) measurements of plagioclase crystals on the JEOL JSM IT800HL FEG-SEM at the University of California, Berkeley, using a single Ultim-Max 100 EDS detector for major elements, and a Wave WDS detector for Mg & K. Finally, Laser Ablation Inductively Coupled Plasma Mass Spectrometry (LA ICP-MS) analysis of clinopyroxene trace element concentrations was performed on a ASI RESOlution 193 nm Laser Ablation system coupled to an Agilent 8900 triple quadrupole ICP-MS hosted in the CELTIC laboratory at Cardiff University.

The primary calibration for EDS analyses performed at Cardiff University (whole-sample maps, linescans, and pyroxene point analyses) was constructed using a mix of mineral and metal standards: Albite (Si, Na), Almandine (Al, Fe), Diopside (Ca), Olivine (Mg), Rutile (Ti), Rhodonite (Mn), and Cr-metal (Cr). The accuracy of this calibration, for the different analysis types, was then assessed using a range of secondary standard materials sourced from either the Smithsonian Microbeam Standards Collection (Jarosewich et al., 1980) and Astimex Standards Ltd. The primary calibration used for EDS analysis of plagioclase crystals at UC Berkeley was constructed using Forsterite (Si), Diopside (Ca), and Nepheline (Na) standards, with the factory calibration used for all other elements. Primary and Secondary standard materials used at UC Berkeley originate from the California Division of Mines (Diopside; data from Charles Chesterman), Takei (1974; synthetic Forsterite), standards previously characterized at UC Berkeley by Ian Carmichael (Nepheline), and specimens (Albite and Labradorite) from Wenk and Kroll (1984).

Prior to and after collection of our whole-sample EDS map data we mapped a series of secondary standards, covering a range of different mineral groups, to assess the precision and accuracy of the map data. For each standard we collected a map, $\sim$1 mm by 1 mm, at the conditions used for our large-scale map analyses. Analytical accuracy was then calculated using

the mean concentration of each oxide in the EDS standard map and the preferred standard value (preferred values can be found in the associated Zenodo repository). Our data reveals that the analytical accuracy of all elements is almost always within 5%, and typically better than 2%, of the preferred value when the measured totals are >2 wt% (Fig. S.2).

To further assess the accuracy of our large-scale map data across a range of mineral groups we consider the measured composition of every pixel against the preferred standard value. This also allows us to assess the precision of EDS mapping for any particular pixel/spot and we also consider the influence of pixel 'binning', i.e., averaging the composition of pixels over a n-by-n area, on the precision of the standard map data by considering the compositions that would be returned by averaging a randomly selected 5-by-5 pixel grid (with the calculation performed 1000 times per standard). Fig. S.2 demonstrates the close agreement between the measured map data and preferred standard values for an Orthoclase standard. Additional graphs can be examined using the Jupyter Notebook supplied in the associated Zenodo repository. The relative precision of analysis is then calculated as the 1 sigma uncertainty in the standard map data, calculated both for individual pixel analyses and for 5-by-5 pixel bins (Fig. S.4).

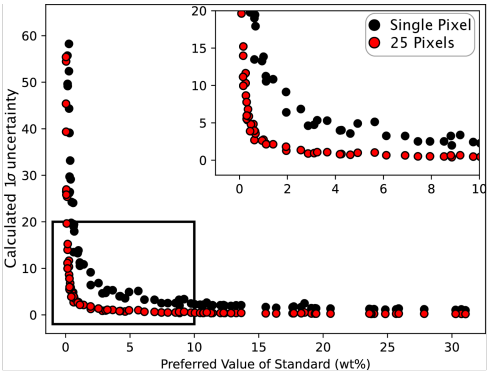


Fig. S.4: Comparison of the calculated uncertainty associated with the EDS map analysis for: (i) individual pixels; and (ii) a 5-by-5 pixel region.

Table 1: Recovery and Relative Standard Deviation for secondary standards analyzed alongside the orthopyroxene and clinopyroxene crystals found in the Galapagos Gabbros. Oxides with concentrations above 2 wt% (shown in bold) show analytical recovery between 98.9 and 100.3%, with the Relative Standard Deviation of these high concentration elements typically less than 0.4%.

| **Standard Material** | **Oxide (Preferred Value wt%)** | **Relative Standard Deviation** | **Recovery** ($\frac{Measured}{Preferred} \times 100$) |
|---|---|---|---|
| Diopside | **$SiO_2$ (55.34)** | 0.168 | 100.1 |
| | **CaO (24.80)** | 0.312 | 100.3 |
| | **MgO (17.76)** | 0.261 | 99.4 |
| | $Al_2O_3$ (0.62) | 7.216 | 93.7 |
| | $FeO_t$ (0.84) | 2.664 | 107.9 |
| | $Na_2O$ (0.40) | 6.846 | 102 |
| Cr-Diopside | **$SiO_2$ (54.91)** | 0.076 | 100.2 |
| | **CaO (24.670)** | 0.198 | 99.5 |
| | **MgO (17.73)** | 0.205 | 99.2 |
| | $Al_2O_3$ (0.30) | 5.862 | 95.7 |
| | $FeO_t$ (1.29) | 1.839 | 107 |
| | $Na_2O$ (0.40) | 4.611 | 101.2 |

Table 1: Recovery and Relative Standard Deviation for secondary standards analyzed alongside orthopyroxene and clinopyroxene crystals (continued).

| **Standard Material** | **Oxide (Preferred Value wt%)** | **Relative Standard Deviation (%)** | **Recovery (%)** |
|---|---|---|---|
| | $Cr_2O_3$ (0.30) | 6.489 | 121.4 |
| Jadeite | **$SiO_2$ (59.58)** | 0.197 | 98.9 |
| | **$Al_2O_3$ (25.04)** | 1.396 | 99.2 |
| | **$Na_2O$ (14.77)** | 1.094 | 99.9 |

Following full sample mapping the samples were characterized by point analyses and linescans to examine the chemistry of specific crystals/regions. Full details of the secondary standard data for the point analyses performed alongside measurements of both pyroxene and plagioclase crystals can be found in Supplementary Datasets 1 & 2, with the main results presented in Tables S.1 and S.2 below. Analysis of secondary standard materials by LA ICP-MS can be found in Supplementary Dataset 3.

Table 2: Recovery and Relative Standard Deviation for secondary standards analyzed alongside the plagioclase crystals found in the Galapagos Gabbros. Results for MgO and $K_2O$ demonstrate the Recovery and Standards Deviation of WDS analysis, all other oxides were measured by EDS. When $K_2O$ contents are determined by EDS they are marked by a ***. Major elements for each standard (typically concentrations $> 2$ wt%) are shown in bold.

| **Standard Material** | **Oxide (Preferred Value wt%)** | **Relative Standard Deviation (%)** | **Recovery ($\frac{Measured}{Preferred} \times 100$)** |
|---|---|---|---|
| Labradorite | **$SiO_2$ (51.25)** | 0.193 | 99.8 |
| | **$Al_2O_3$ (30.91)** | 0.11 | 99.7 |
| | **CaO (13.40)** | 0.262 | 100.1 |
| | **$Na_2O$ (3.83)** | 0.738 | 98.7 |
| | $FeO_t$ (0.41) | 5.763 | 100.3 |
| | $K_2O$ (0.12) | 1.33 | 97.6 |
| | | 7.301*** | 98.9*** |
| | MgO (0.14) | 2.977 | 86.5 |
| Anorthite | **$SiO_2$ (44.17)** | 0.28 | 100.1 |
| | **$Al_2O_3$ (34.95)** | 0.047 | 102.3 |
| | **CaO (18.63)** | 0.258 | 101.3 |
| | $Na_2O$ (0.79) | 3.288 | 84 |
| Nepheline | **$SiO_2$ (43.49)** | 0.074 | 100.9 |
| | **$Al_2O_3$ (33.76)** | 0.172 | 100.6 |
| | **$Na_2O$ (16.92)** | 0.139 | 99.4 |

Table 2: Recovery and Relative Standard Deviation for secondary standards analyzed alongside the plagioclase crystals (continued).

| **Standard Material** | **Oxide (Preferred Value wt%)** | **Relative Standard Deviation** | **Recovery** |
|---|---|---|---|
| | **$K_2O$ (5.61)** | 0.448*** | 103.0*** |
| Albite | **$SiO_2$ (68.241)** | 0.07 | 101.4 |
| | **$Al_2O_3$ (19.90)** | 0.374 | 99.5 |
| | **$Na_2O$ (11.94)** | 0.361 | 100.6 |
| Orthoclase | **$SiO_2$ (64.793)** | 0.035 | 101.5 |
| | **$Al_2O_3$ (16.72)** | 0.203 | 98.9 |
| | **$K_2O$ (15.49)** | 0.161*** | 100.3*** |
| | $Na_2O$ (0.91) | 3.237 | 105.8 |
| | $FeO_t$ (1.88) | 2.044 | 94.2 |

The accuracy of the linescan analyses was tracked through linescans – carried out using identical analytical conditions to the unknowns – performed on Diopside and Cr-Augite secondary standard materials. Plotting up the recovery values for these linescans displays several things. First there is clear heterogeneity in the Diopside standard with one end of the linescan displaying a more Fe-rich and Mg-poor composition. This area was avoided for all other analysis of the Diopside standard performed in this study. Second, most oxides return recovery values centered on 100% (Fig. S.5)

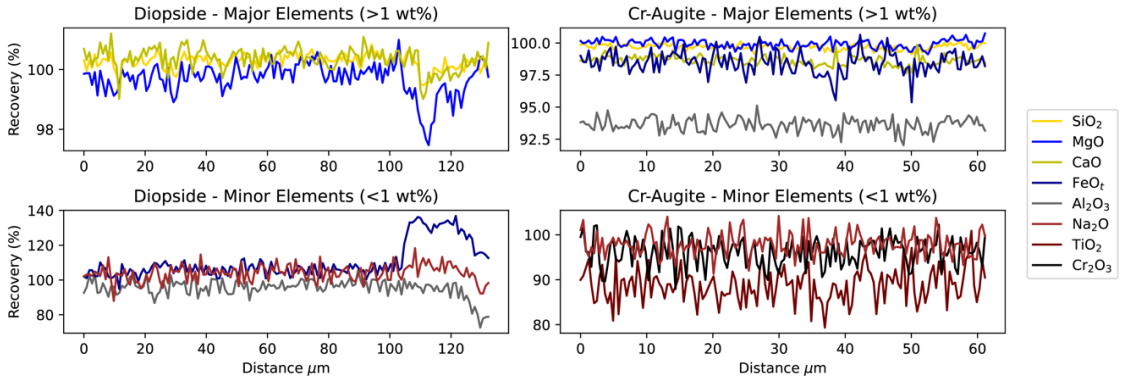


Fig. S.5: Linescan data from a Diopside and Cr-Augite standard relative to the preferred standard values.

# Whole-Rock Composition of the Isla Floreana Gabbros

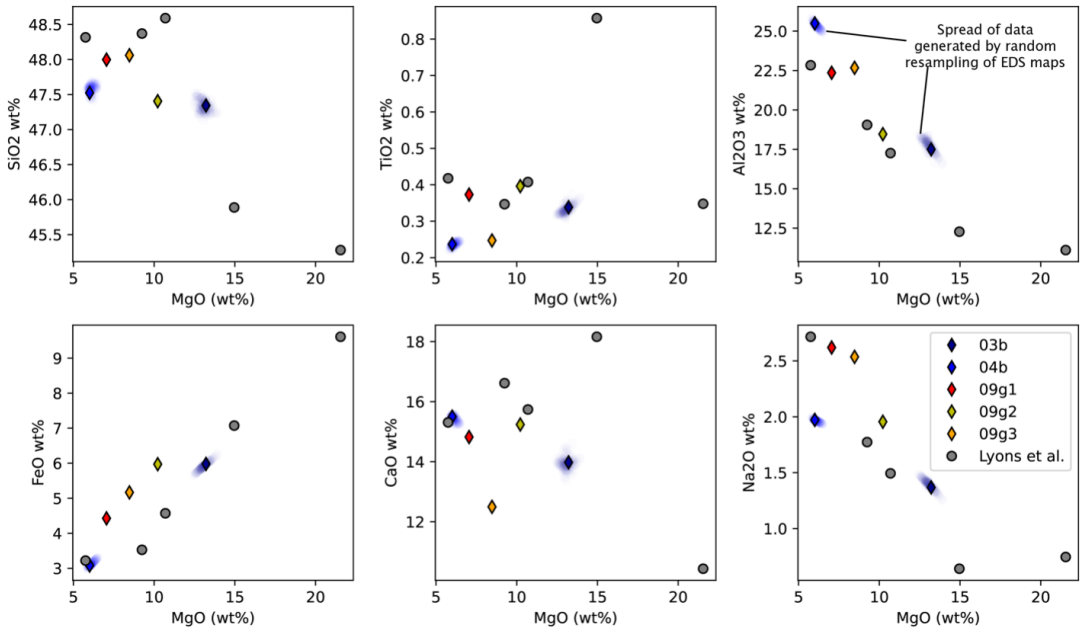


Fig. S.6: Comparison of the bulk-rock compositions generated by EDS mapping of the gabbro xenoliths analyzed in this study to XRF determined compositions of a seperate suite of gabbro xenoliths that were also collected from the northern coast of Isla Floreana (data from Lyons et al. 2007). While these represent separate sample sets, we can see that the EDS-determined compositions lie within the range of composition determined by XRF on similar samples from the same island. Also shown is the spread of compositions generated by our bulk-rock error analysis (see Supplementary Text), where smaller subregions of samples 03b an 04b are randomly selected to calculate the uncertainty associated with our bulk-rock estimates.

As the EDS map data is shown to be accurate across a range of different mineral groups we use our EDS maps to estimate a 'bulk-rock' composition for each of the Galapagos gabbros following the methods outlined in the main text. For these calculations we used mineral densities of 3.35 g/cm$^3$ for orthopyroxene, 3.4 g/cm$^3$ for clinopyroxene, 3.5 g/cm$^3$ for olivine, 2.7 g/cm$^3$ for plagioclase, and 4.05 g/cm$^3$ for spinel. Densities for all phases were taken from The Engineering Toolbox (2009), using linear interpolation between end-member components (based on mole proportions) to estimate the approximate density for each phase identified in the Galapagos gabbros. To assess the uncertainty generated by the random 'cut' of the sample analyzed by EDS mapping we 'resampled' the 03b and 04b maps 200 times, on each iteration a random set of coordinates was generated to extract an enclosed region covering at least 50% of the total sample surface and a bulk-rock composition was generated for this sub-area. This analysis reveals little variation in most elements, with the relative standard deviation of major elements $<$2% (Fig. S.6).

The composition of the Isla Floreana gabbros also helps to confirm their origin as cumu-

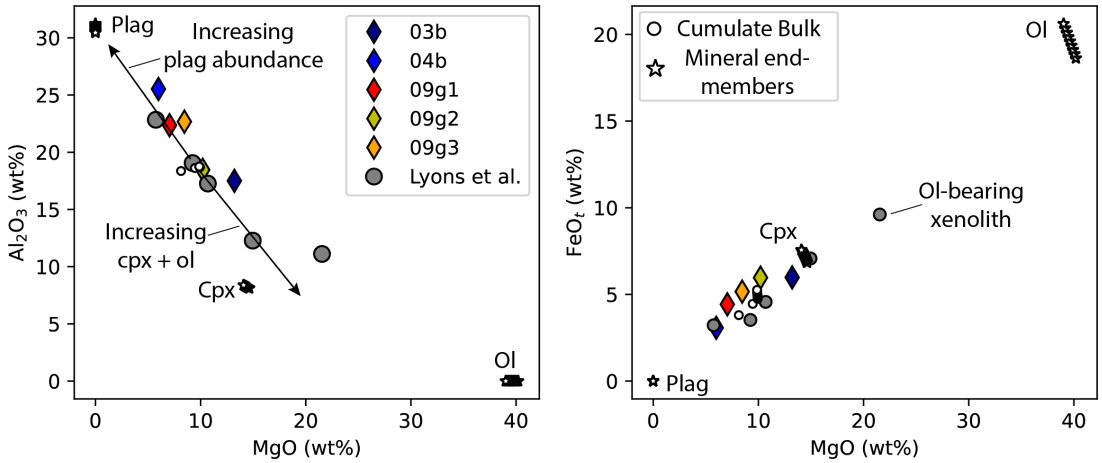


Fig. S.7: Gabbro bulk-rock compositions compared to the composition of cumulate residues and mineral compositions predicted by fractional crystallization models in pMELTS. Models demonstrate that the gabbro compositions plot along a mixing line between plagioclase and clinopyroxene/olivine, confirming that these samples likely originated as olivine-bearing gabbroic mushes, with orthopyroxene forming during subsolidus reactions.

late deposits, likely containing an initial mixture of olivine, clinopyroxene, plagioclase, and some residual melt (with olivine then being replaced by orthopyroxene during subsolidus reactions). Fractional crystallization calculations in pMELTS (performed using PetThermoTools) were used to track the composition of the cumulate residue (i.e., the bulk composition of the solid products) during gabbroic crystallization at 7000 bars. A high-MgO basalt from Cerro Azul, a $H_2O$ content of 0.5 wt% and a $Fe^{3+}/Fe_t$ ratio of 0.15 were used as the starting parameters. Results are shown in Fig. S.7, and demonstrate that the composition of all samples analyzed in this study (and by Lyons et al., 2007) can be explained as cumulate rocks with varying enrichment/depletion in plagioclase (potentially explained by density-driven variations in settling velocity).

# Phase Diagram Analysis

In the main text we use thermodynamic calculations to assess the conditions of subsolidus storage for the Isla Floreana gabbros. Here we show the phase diagrams calculated using PetThermoTools for samples 03b and 04b as well as gabbro FLX513 from Lyons et al. (2007). These calculations were performed using the Holland et al. (2018), pMELTS (Ghiorso et al. 2002), and rhyolite-MELTS (Gualda et al., 2012) thermodynamic models. In all figures below (Fig. S.8 – 16) we highlight the position of the olivine-out reaction and garnet-out reactions (with increasing and decreasing pressure, respectively), as well as the position of the orthopyroxene-in boundary (with decreasing temperature). These three reactions boarder the P-T regions where the mineral assemblage of the Isla Floreana gabbros are recreated by the thermodynamic models. Python code and Jupyter Notebooks used to create these phase diagrams are included in the Zenodo repository associated with this publication.

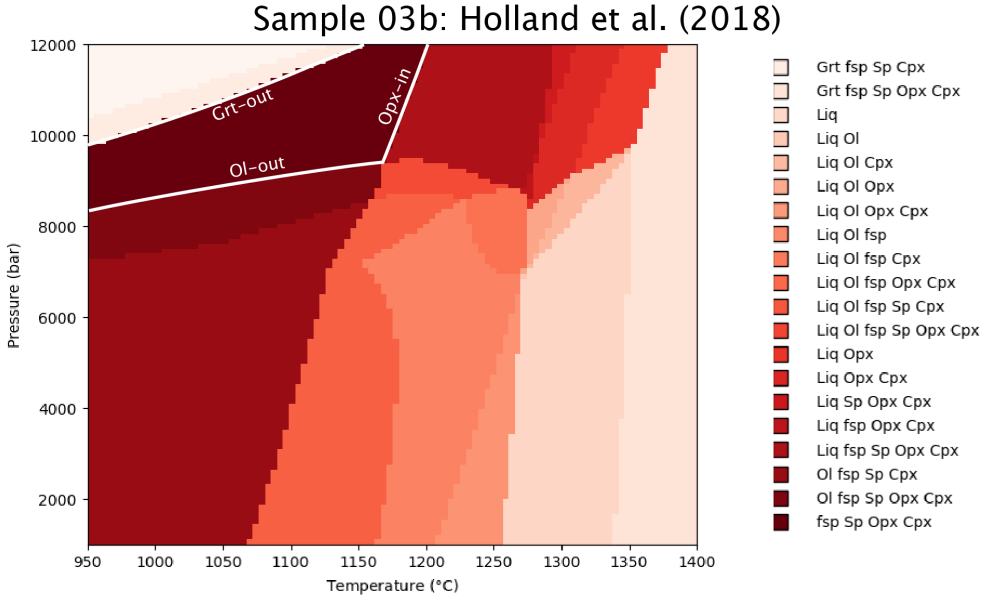


Fig. S.8: Phase diagram calculated using the EDS determined composition of sample 03b and the Holland et al. (2018) thermodynamic model. Calculations performed via PetThermoTools and MAGEMin (Gleeson & Wieser 2024; Riel et al. 2022; MAGEMin_C v1.4.9). Position of the garnet, orthopyroxene, and olivine stability regions indicated by the white lines.

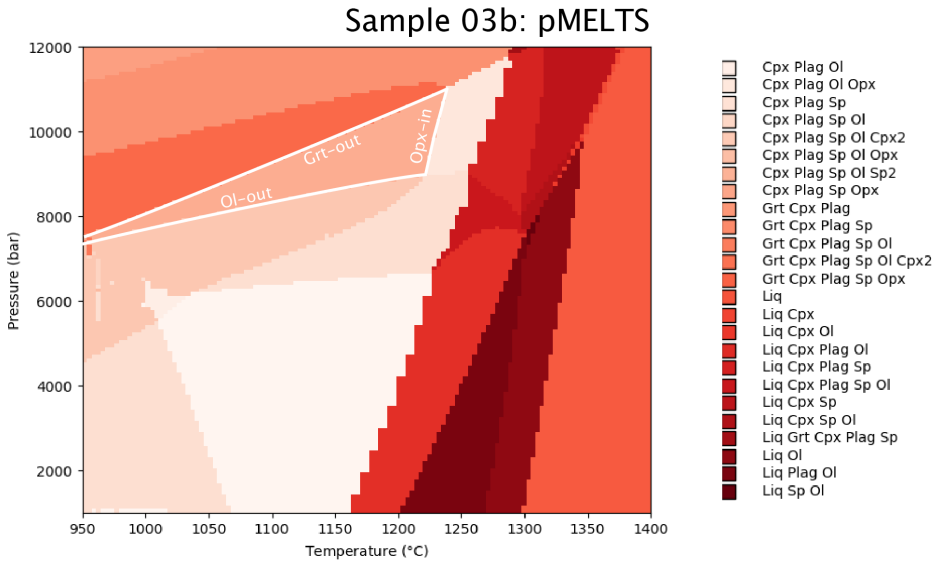


Fig. S.9: Phase diagram calculated using the EDS determined composition of sample 03b and the pMELTS thermodynamic model (Ghiorso et al. 2002). Calculations performed via PetThermoTools and alphaMELTS for Python (Gleeson & Wieser 2024). Position of the garnet, orthopyroxene, and olivine stability regions indicated by the white lines.

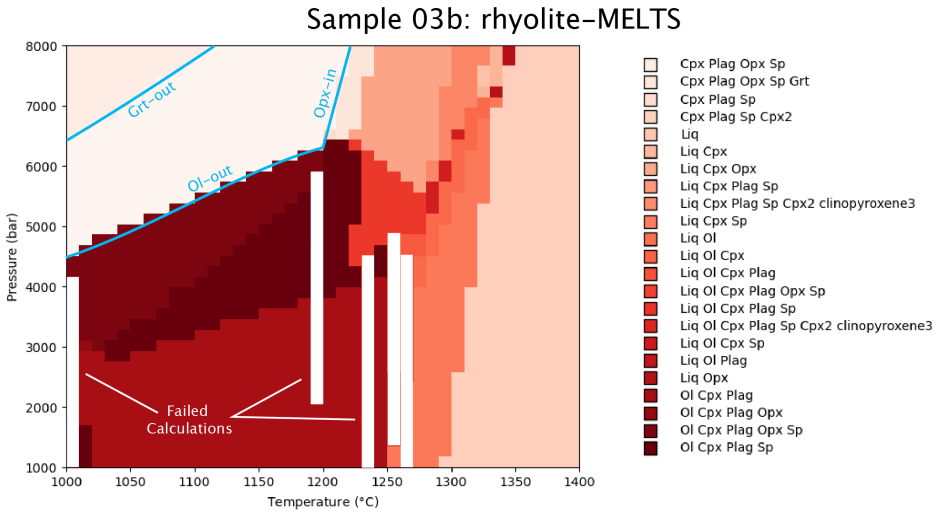


Fig. S.10: Phase diagram calculated using the EDS determined composition of sample 03b and the rhyolite-MELTS v1.0.2 thermodynamic model (Gualda et al. 2012). Calculations performed via PetThermoTools and alphaMELTS for Python (Gleeson & Wieser 2024). Position of the garnet, orthopyroxene, and olivine stability regions indicated by the blue lines.

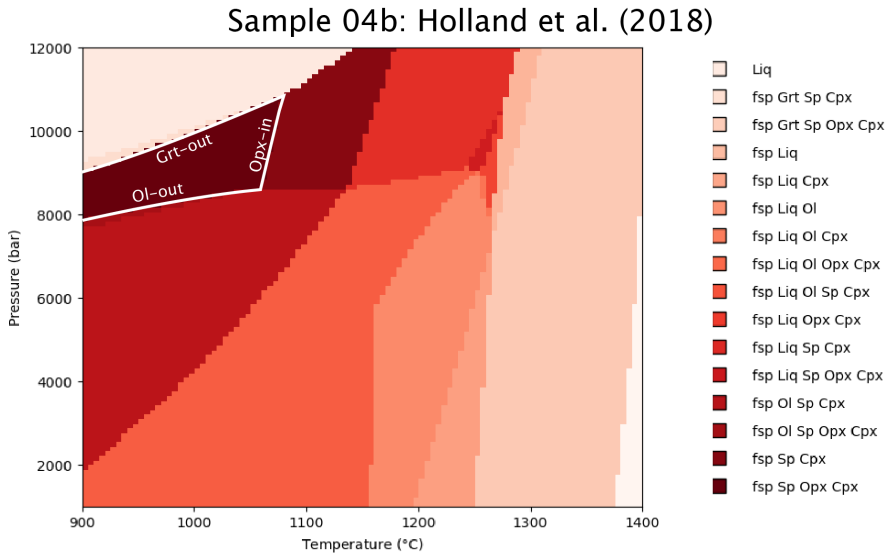


Fig. S.11: Phase diagram calculated using the EDS determined composition of sample 04b and the Holland et al. (2018) thermodynamic model. Calculations performed via PetThermoTools and MAGEMin (Gleeson & Wieser 2024; Riel et al. 2022; MAGEMin_C v1.4.9). Garnet, orthopyroxene, and olivine stability regions indicated by the white lines.

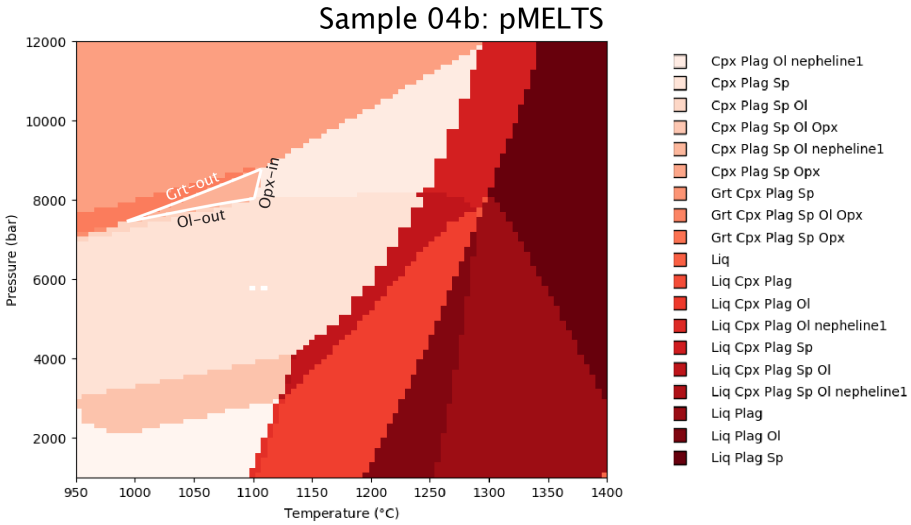


Fig. S.12: Phase diagram calculated using the EDS determined composition of sample 04b and the pMELTS thermodynamic model (Ghiorso et al. 2002). Calculations performed via PetThermoTools and alphaMELTS for Python (Gleeson & Wieser 2024). Position of the garnet, orthopyroxene, and olivine stability regions indicated by the white lines.

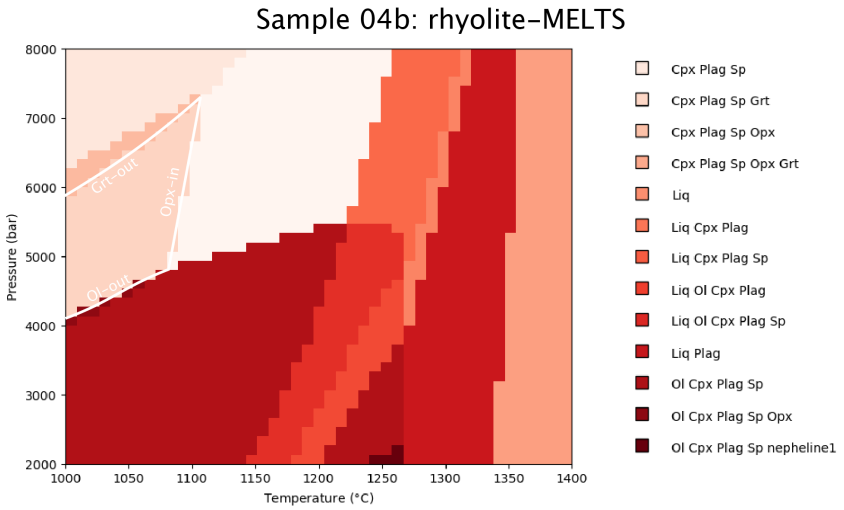


Fig. S.13: Phase diagram calculated using the EDS determined composition of sample 04b and the pMELTS thermodynamic model (Ghiorso et al. 2002). Calculations performed via PetThermoTools and alphaMELTS for Python (Gleeson & Wieser 2024). Position of the garnet, orthopyroxene, and olivine stability regions indicated by the white lines.

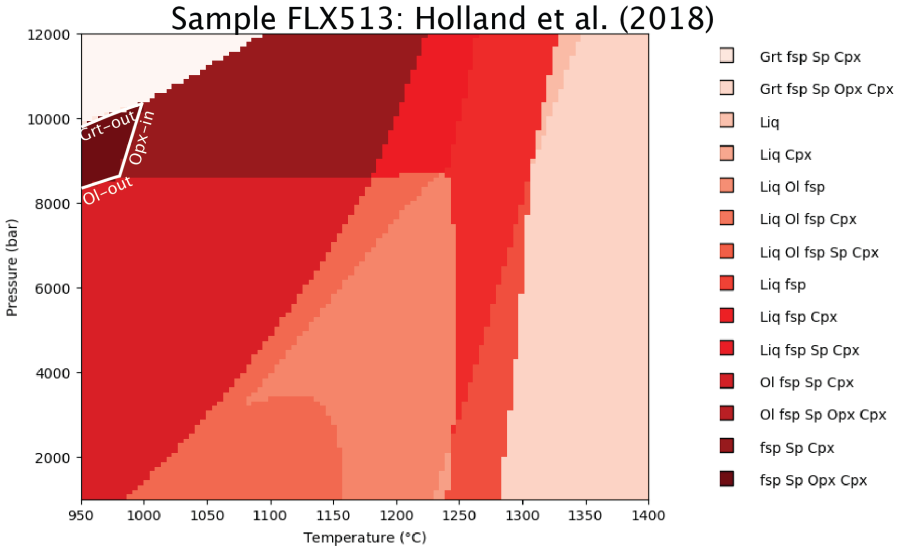


Fig. S.14: Phase diagram calculated using the XRF determined composition of sample FLX513 from Lyons et al. (2007) and the Holland et al. (2018) thermodynamic model. Calculations performed via PetThermoTools and MAGEMin (Gleeson & Wieser 2024; Riel et al. 2022; MAGEMin_C v1.4.9). Garnet, orthopyroxene, and olivine stability regions indicated by the white lines.

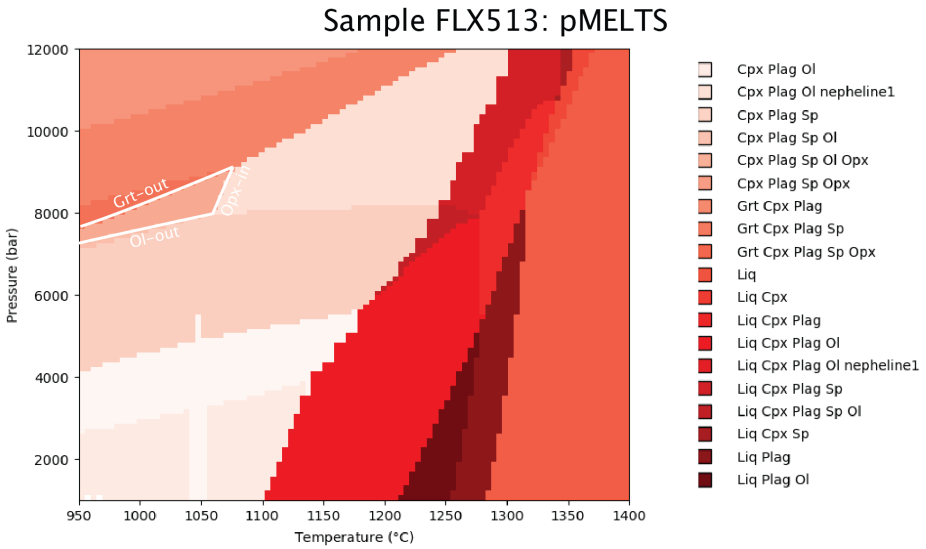


Fig. S.15: Phase diagram calculated using the XRF determined composition of sample FLX513 from Lyons et al. (2007) and the pMELTS thermodynamic model (Ghiorso et al. 2002). Calculations performed via PetThermoTools and alphaMELTS for Python (Gleeson & Wieser 2024). Position of the garnet, orthopyroxene, and olivine stability regions indicated by the white lines.

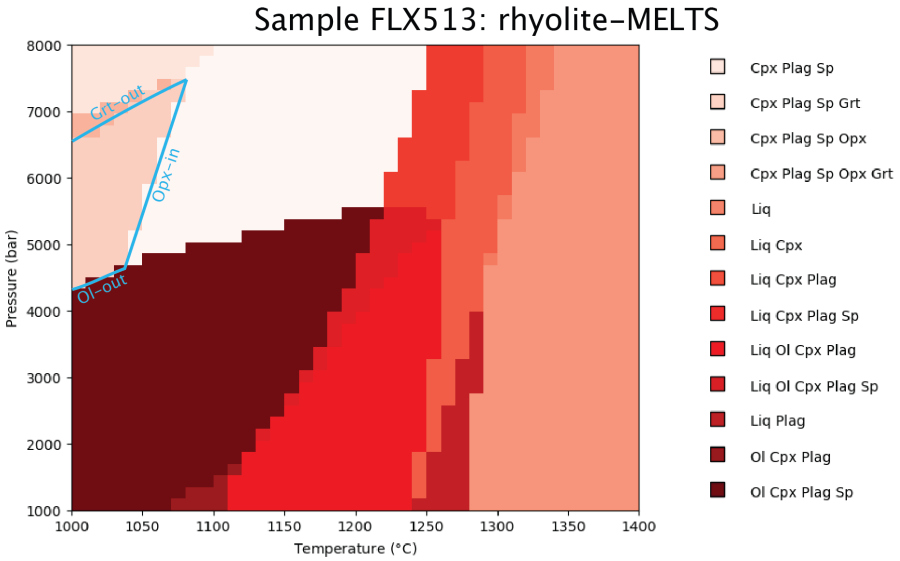


Fig. S.16: Phase diagram calculated using the XRF determined composition of sample FLX513 from Lyons et al. (2007) and the pMELTS thermodynamic model (Ghiorso et al. 2002). Calculations performed via PetThermoTools and alphaMELTS for Python (Gleeson & Wieser 2024). Position of the garnet, orthopyroxene, and olivine stability regions indicated by the blue lines.

# Phase Maps and Mineral Proportions

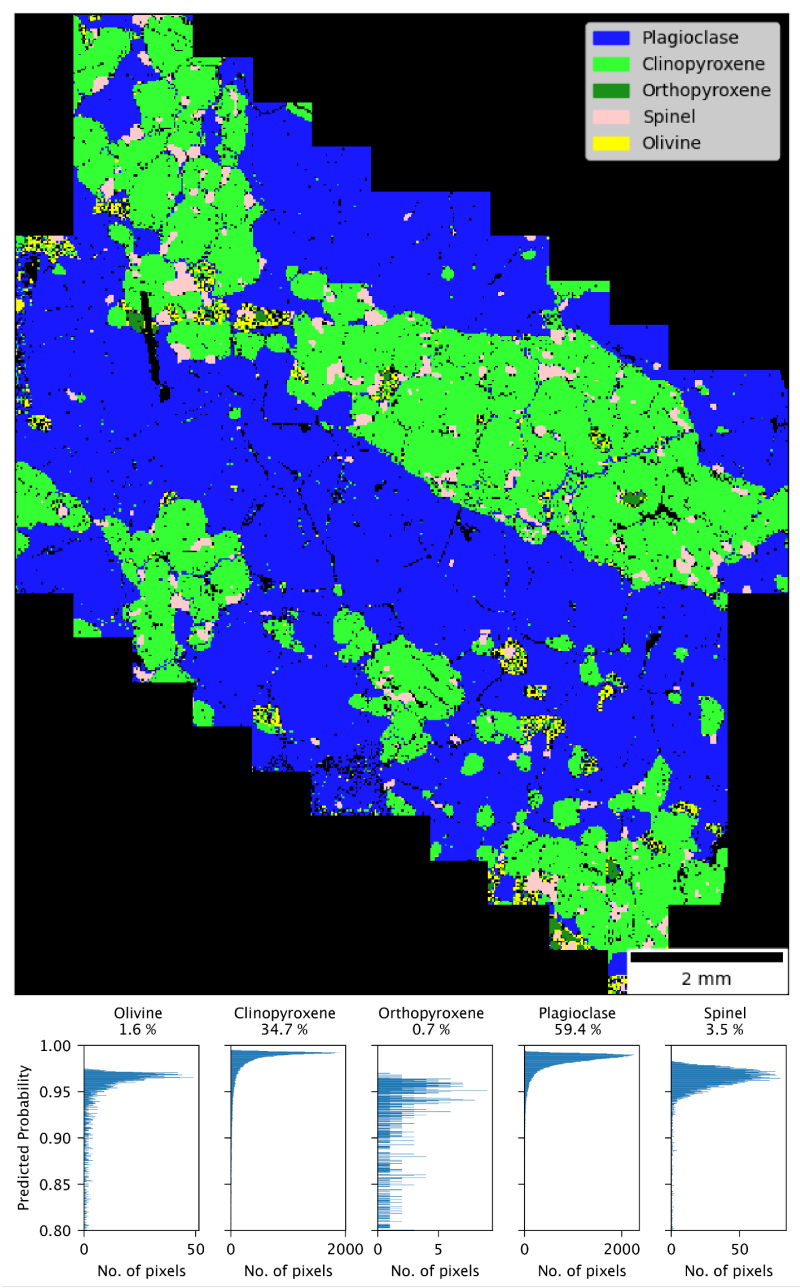


Fig. S.17: Phase map of sample 09g1 and associated phase proportions. As with all 09g samples olivine is identified at the boundaries of the orthopyroxene crystals

One of the main outcomes of our EDS maps, combined with the new capabilities of mineralML (Shi et al. 2023), is the ability to automatically convert EDS map data into phase maps and estimates of phase proportions. This is shown in Fig. 2 of the main text, with phase maps and associated phase proportions of the additional three samples shown here.

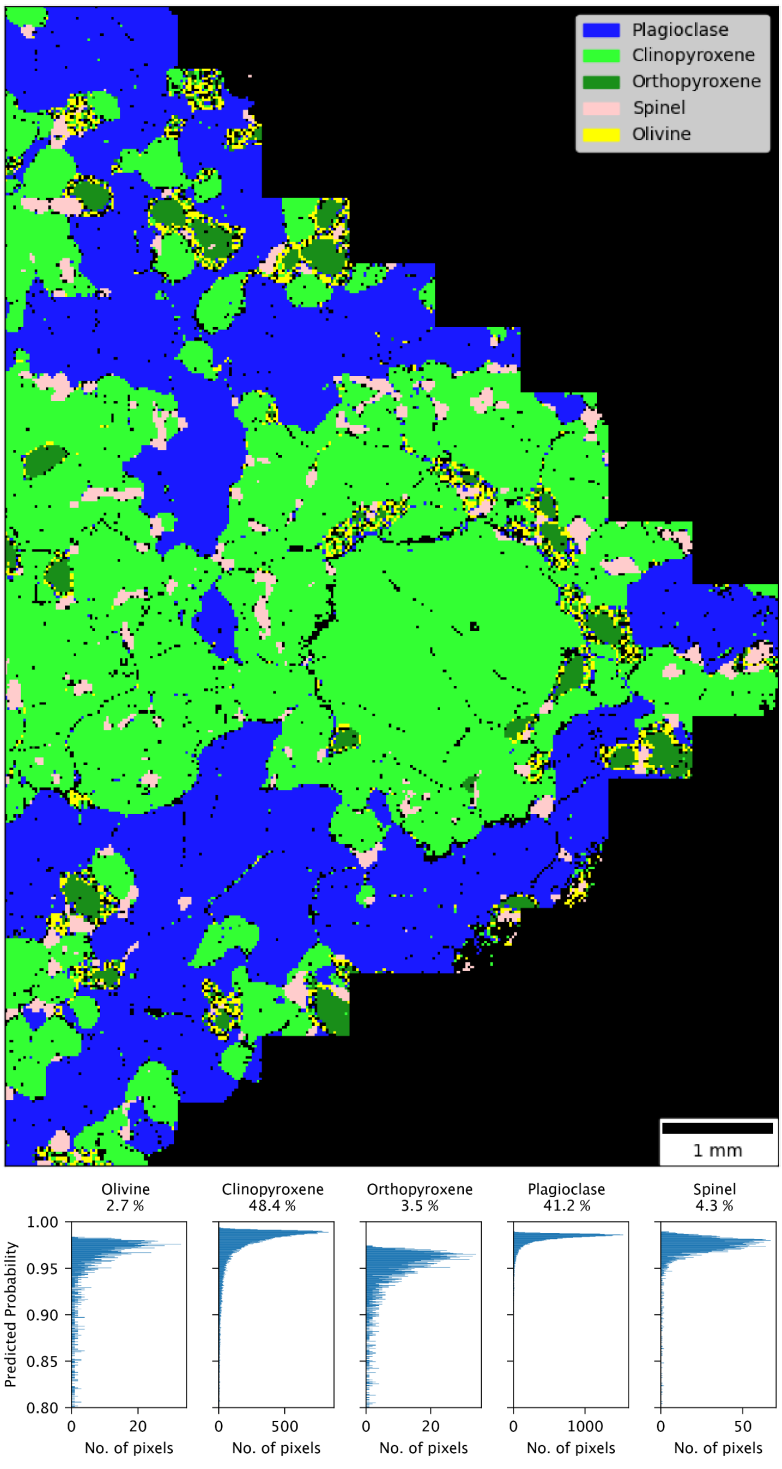


Fig. S.18: Phase map of sample 09g2 and associated phase proportions.

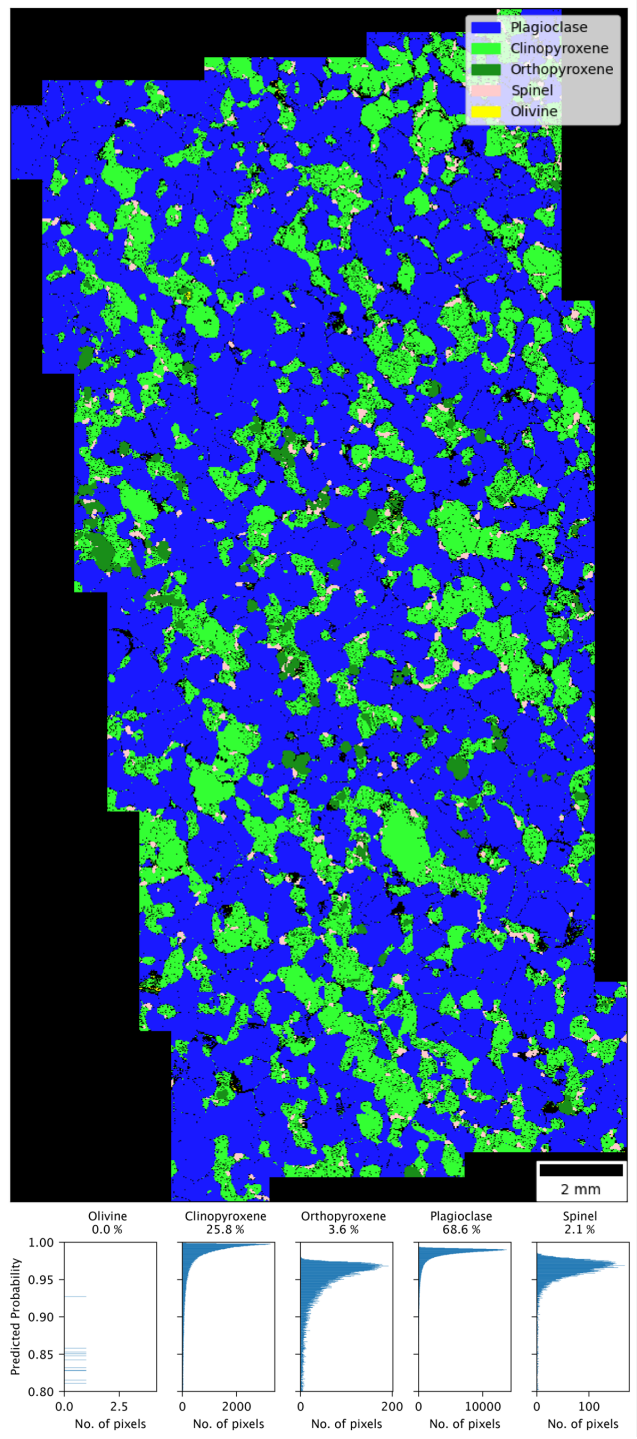


Fig. S.19: Phase map of sample 04b and associated phase proportions. This sample contains the highest proportion of plagioclase identified in any of the sample considered in this study.

# Compositional Variability

Data collected from EDS mapping provide insights into the compositional variability of the samples, with limited heterogeneity present with the exception of core-rim An zoning in sample 03b. Example compositional maps are shown below alongside histograms of the Plagioclase An content, Clinopyroxene Mg#, and Spinel Cr# calculated from the EDS map data. Code used to produce these figures is available in a Jupyter Notebook found within the associated Zenodo Repository.

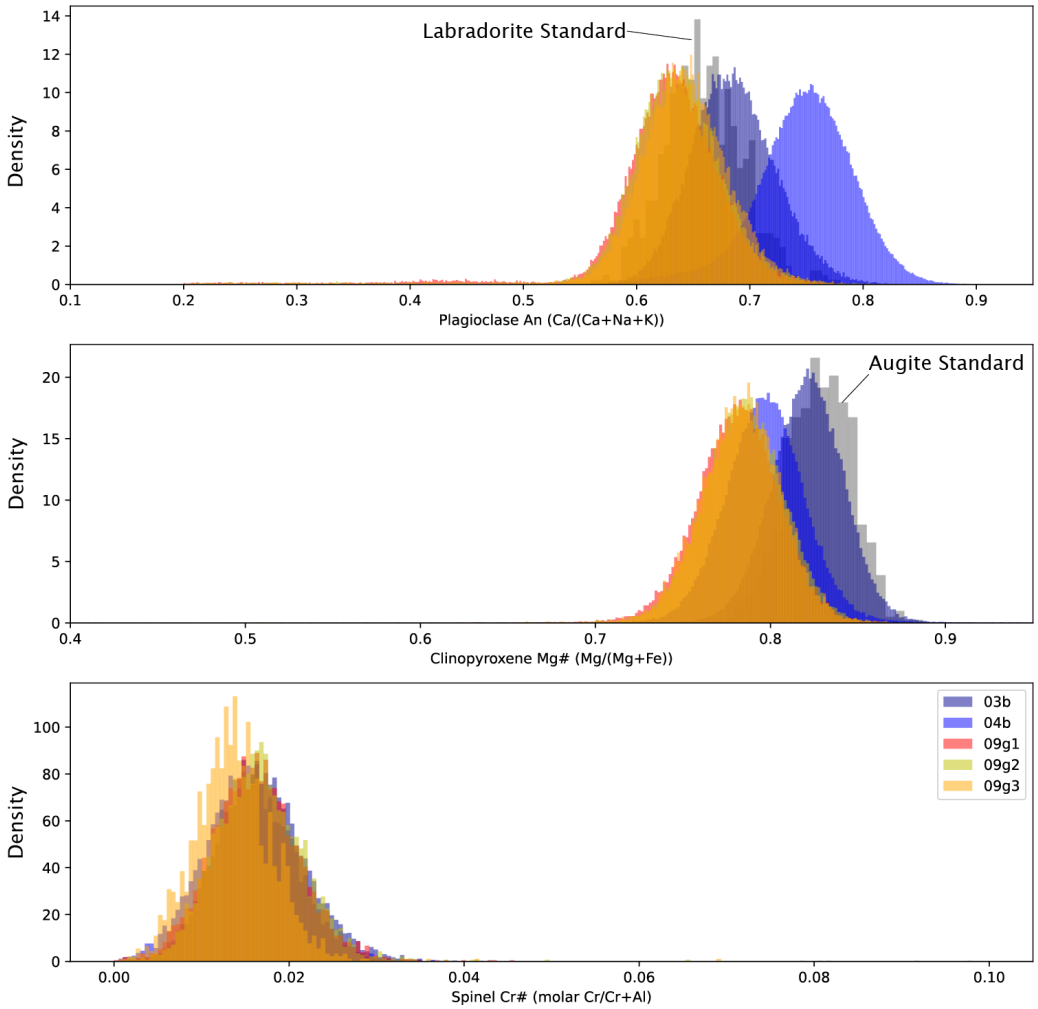


Fig. S.20: Histograms of key compositional parameters for the Isla Floreana gabbros. Plagioclase An contents reveals a tail to low An values for most samples, with these analyses typically found near or along grain boundaries. Labradorite and Augite standards indicate that the spread of compositions associated with the primary normal distribution of each sample it largely controlled by the analytical uncertainty of the EDS map analyses. Spinel crystals have extremely low Cr# values. Data for 09g1, 09g2, and 09g3 are near identical and overlap on all plots.

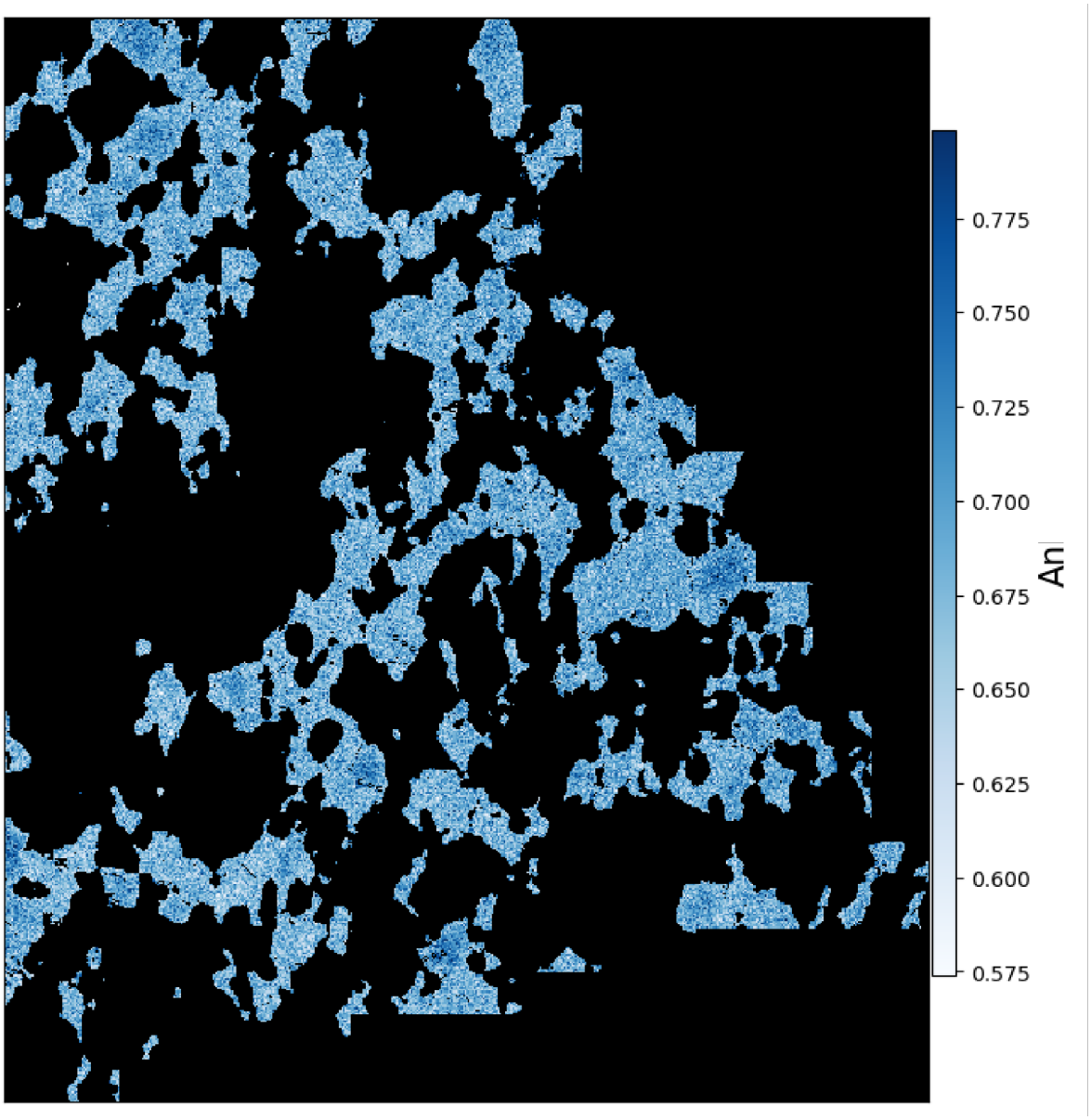


Fig. S.21: EDS map of An contents in plagioclase crystals from sample 03b. The darker colors in the core of some crystals indicate higher An contents, revealing the presence of core-rim normal zoning.

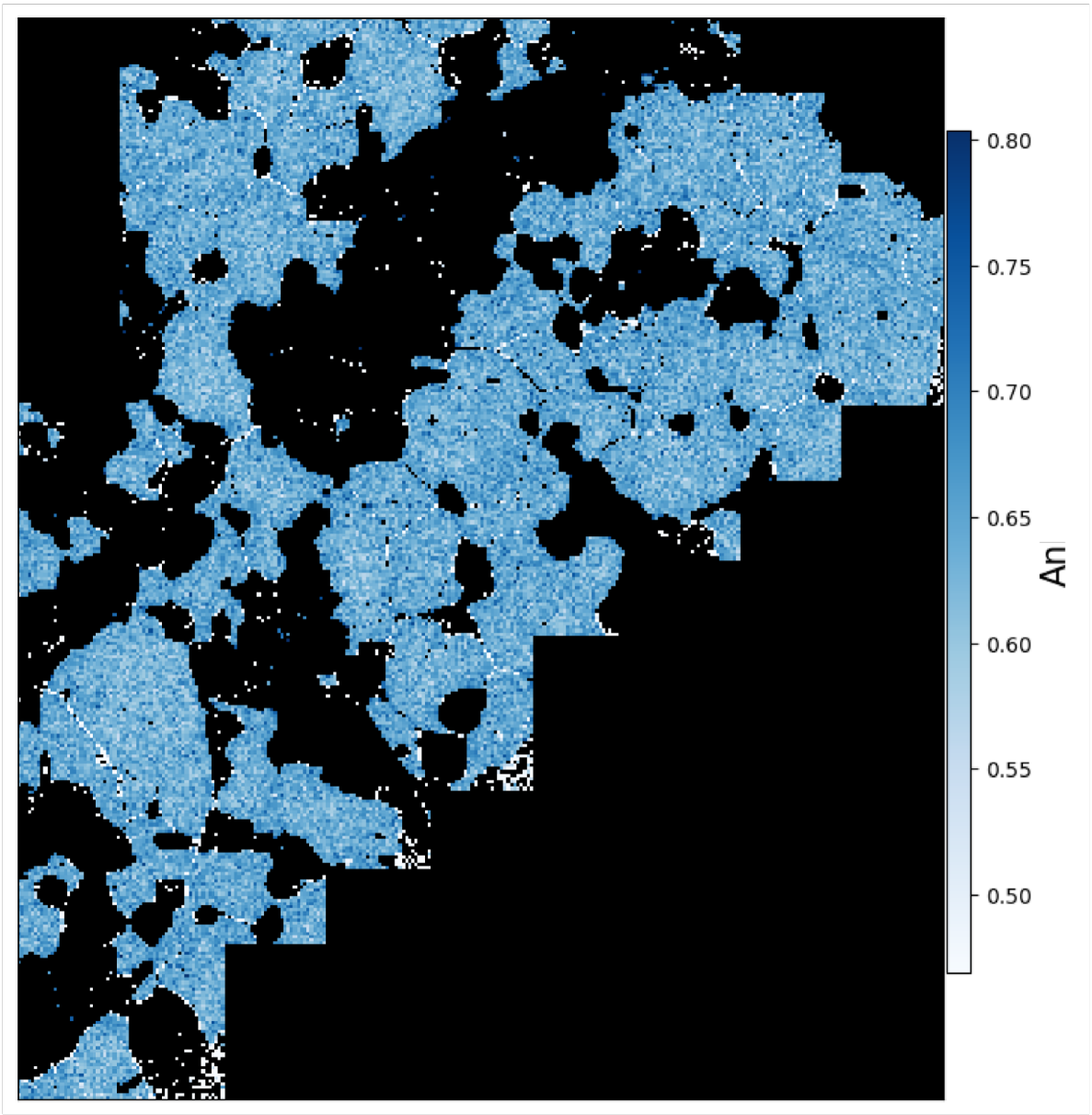


Fig. S.22: EDS map of An contents in plagioclase crystals from sample 09g3. Limited compositional variability is found in this sample compared to sample 03b.

In addition to the large-scale map data, high-resolution maps of orthopyroxene-clinopyroxene grain boundaries also reveal information about the compositional heterogeneity of the Isla Floreana gabbros, in particular, the presence of olivine in orthopyroxene breakdown rims.

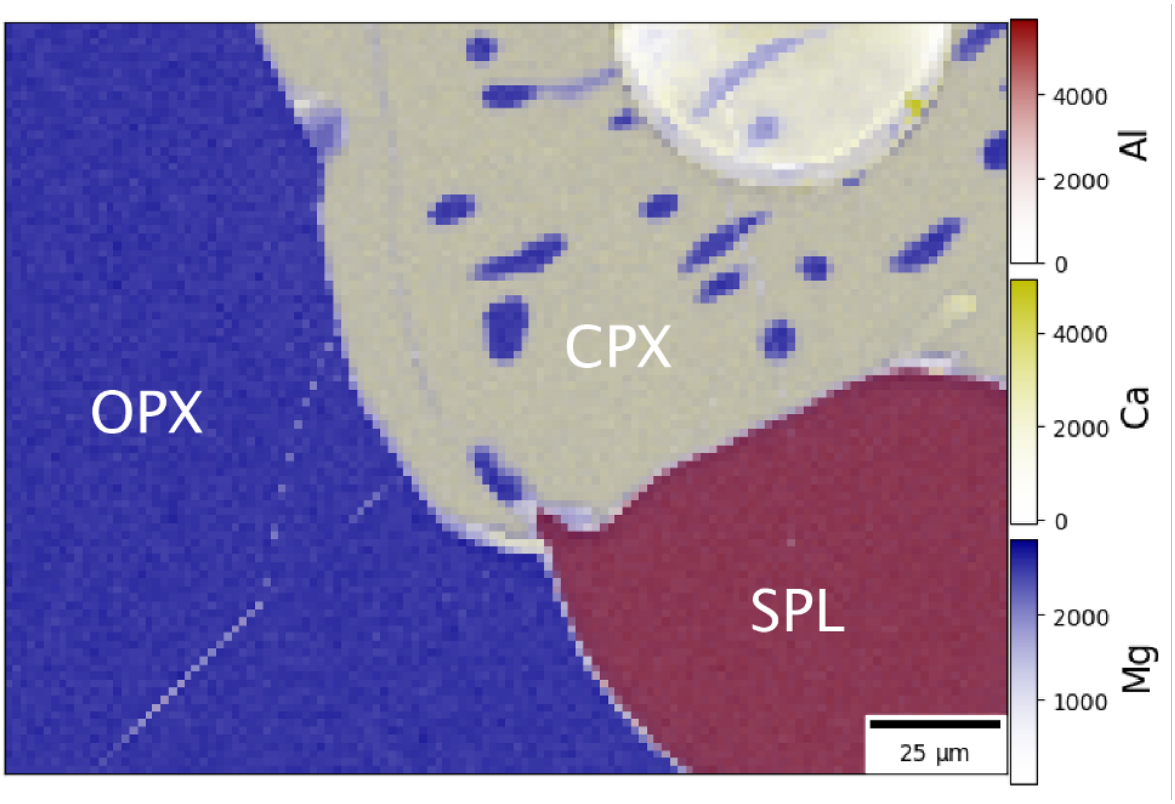


Fig. S.23: EDS chemical map of a clinopyroxene-orthopyroxene-spinel triple boundary in sample 04b. Colors are based on the total counts of Mg, Ca, and Al for each pixel. Exsolution of orthopyroxene is seen in the clinopyroxene crystals. This is a feature only seen in sample 04b.

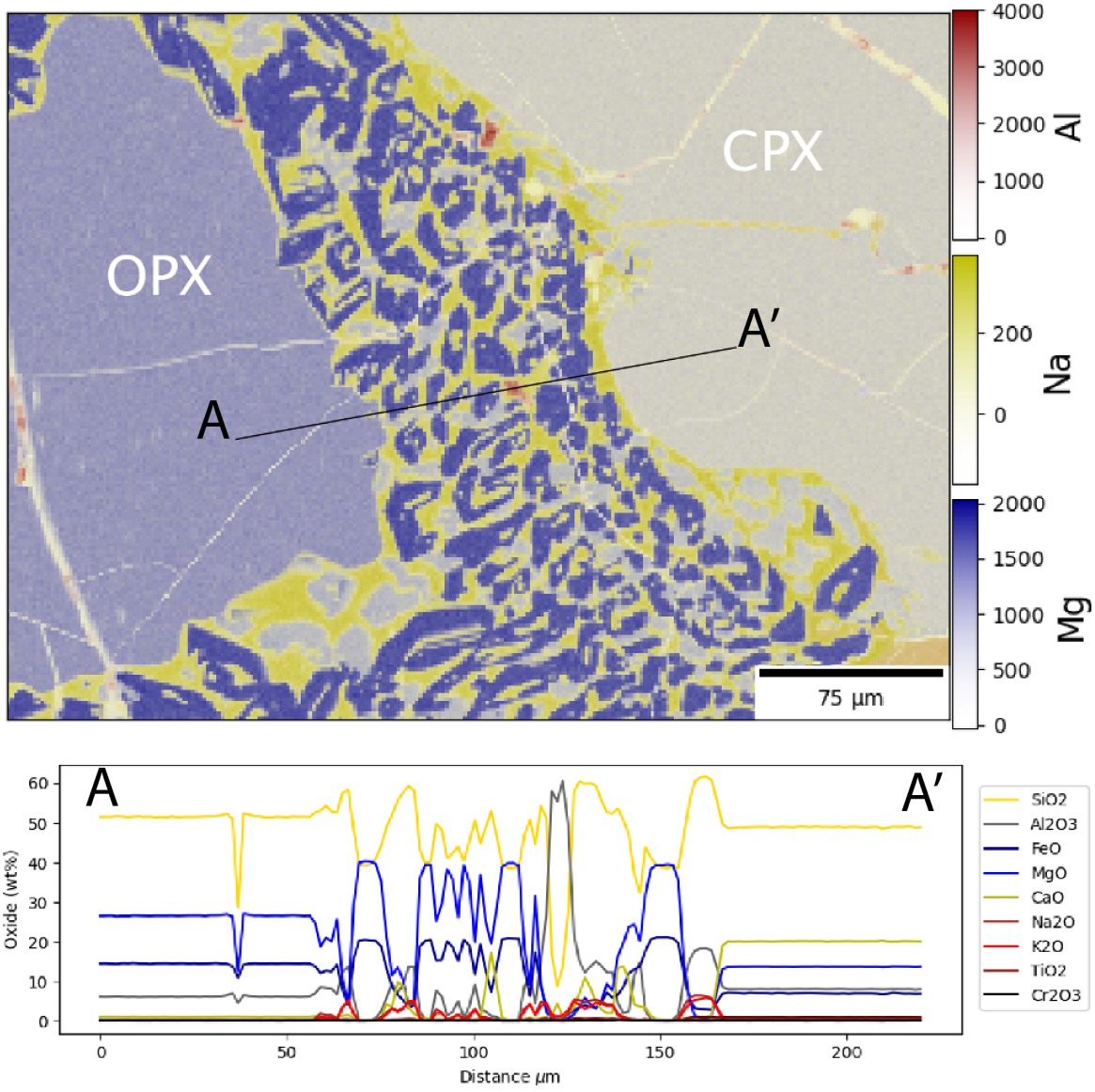


Fig. S.24: EDS chemical map of a clinopyroxene-orthopyroxene grain boundary in sample 09g1. Colors are based on the total counts of Mg, Ca, and Al for each pixel. A small spinel crystal, indicated by the high Al2O3 contents in the linescan is also found in the breakdown zone.

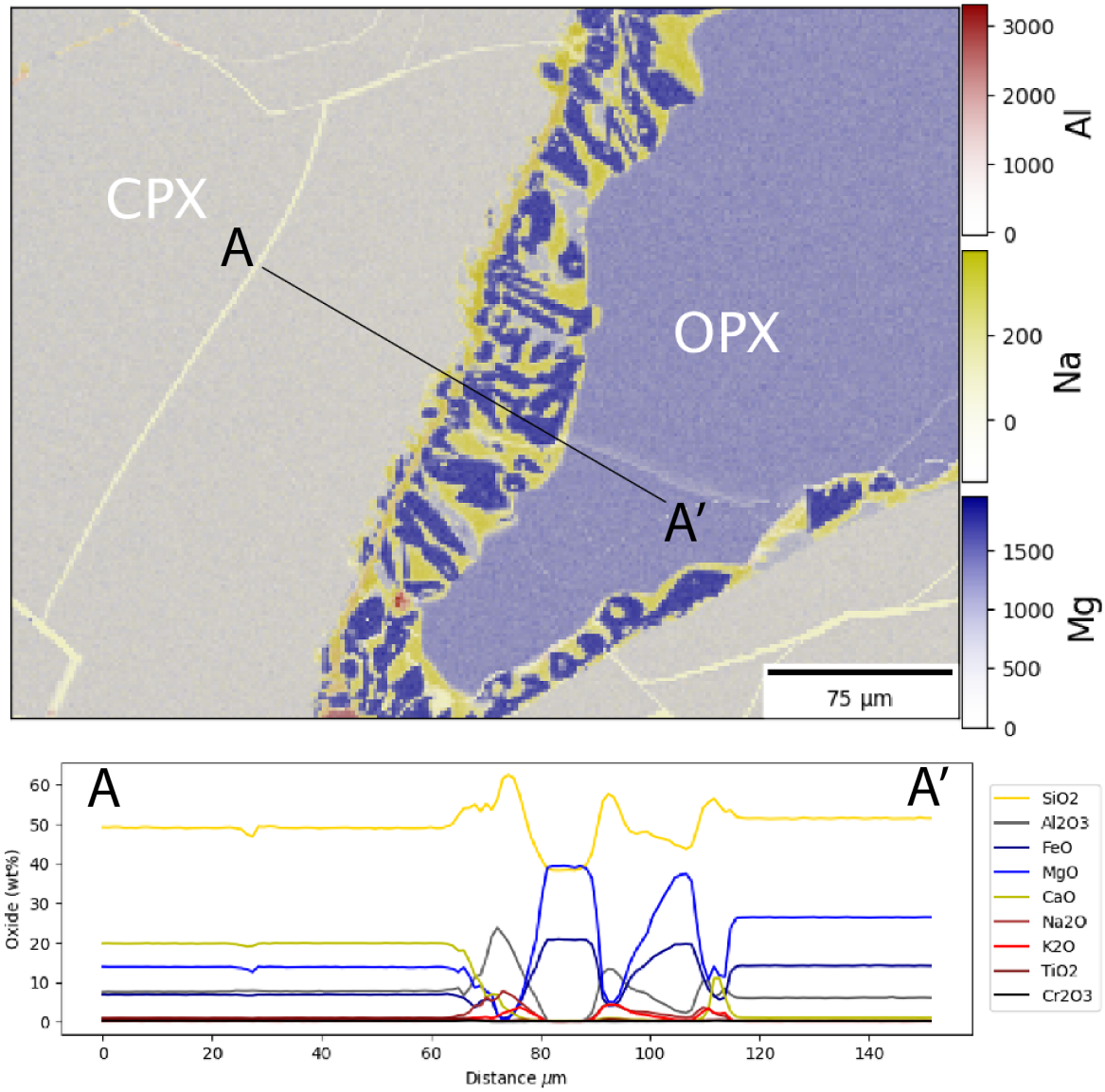


Fig. S.25: EDS chemical map of a clinopyroxene-orthopyroxene grain boundary in sample 09g2. Colors are based on the total counts of Mg, Ca, and Al for each pixel. The orthopyroxene grain is surrounded by a breakdown rim composed of olivine and silicate melt.

# Fluid Inclusions

## Fluid compositions

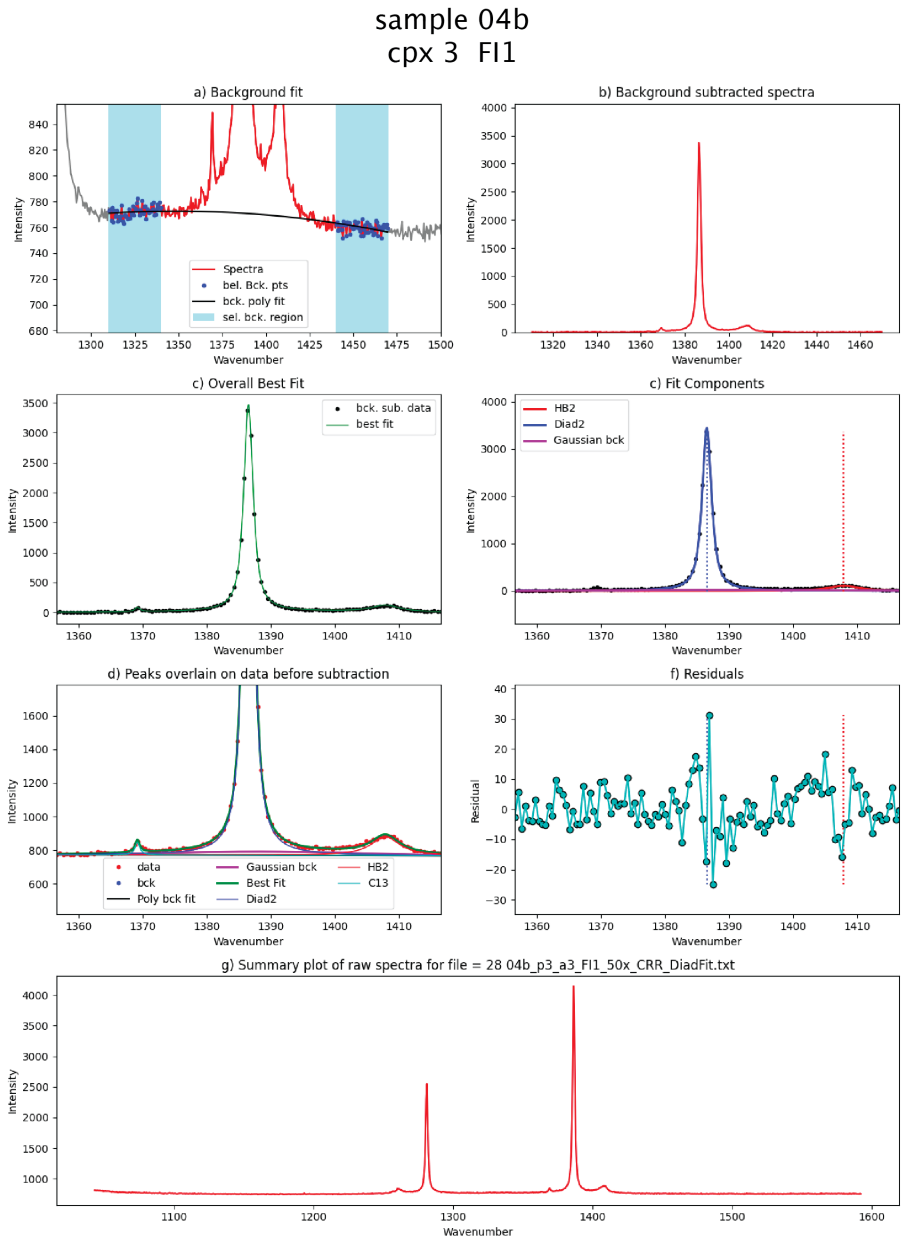


Fig. S.26: Raman spectrum for FI 1 in clinopyroxene 3 from sample 04b. Panels a. - f. demonstrate the way DiadFit determines the background position (a.) and finds the best fit to the second $CO_2$ diad and nearby secondary peaks. The raw spectra is then shown in panel g. with both the $CO_2$ diads clearly visible.

In this study we analyzed 43 fluid inclusions across 2 samples. Where possible we analyzed fluid inclusions by both microthermometry and Raman Spectroscopy to determine their composition and $CO_2$ density. Comparison of the two methods indicates close agreement in the estimated $CO_2$ densities, with the majority of data plotting between 0.98 - 1.02 g/cm$^3$ for

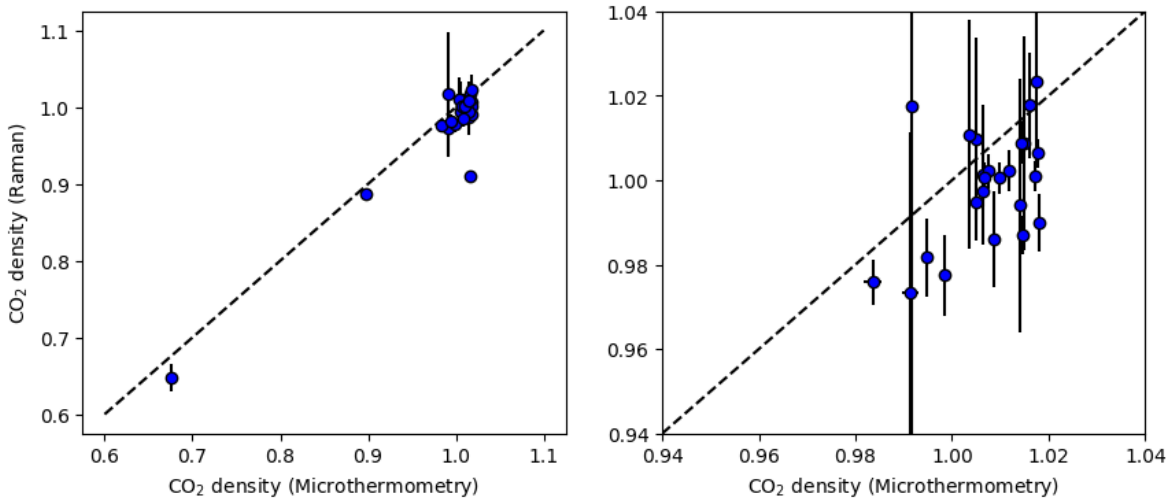


Fig. S.27: Comparison of the $CO_2$ density (in g/cm$^3$) estimated using microthermometry and Raman Spectroscopy.

both approaches (Fig. S.27) Microthermometry revealed several inclusions that have melting temperatures $> 1^oC$ below the theoretical melting point for pure $CO_2$, indicating the presence of impurities within these inclusions. Notably, the inclusions with lower melting temperatures are not offset with respect to the estimated $CO_2$ densities from those with melting temperatures near the pure $CO_2$ theorectical melting temperature. This indicates that any impurity is likely to have little influence on our overall study (and calculated storage pressures). Nevertheless, both Raman Spectroscopy and COOLPROP modeling (Bell et al. 2014) were used to assess the cause of the observed melting point depression. Within our standard Raman analyses (6 mW laser power, 1800 grating), which targets wavenumbers between 1050 cm$^{-1}$ and 1580 cm$-1$, the $CO_2$ diads and associated minor peaks (hot bands, C-13) were the only peaks identified (Fig. S.26). In short, the Raman analyses provide no evidence for the presence of $SO_2$, carbonates, or any other Raman-active species within this wavenumber region. Further examples of the raman spectra collected can be found in the associated Zenodo repository.

To confirm that our analyses did not miss the presence of impurities - owing to the choice of grating and/or low laser power - we also performed Raman analyses on a small number of fluid inclusions selected to encompass the entire range of melting temperatures identified in this study. For these secondary analyses we increased the laser power to 49 mW and the grating was changed to 300. This enabled us to access wavenumbers up to 3270 cm$^{-1}$. Comparison of three spectra acquired using these conditions are shown in Fig. S.28 and demonstrate that there are no observable differences in the Raman spectra of fluid inclusions with melting temperatures between -56.5$^o$C and -60.1$^o$C. Consequently, we conclude that the melting point depression observed in our fluid inclusions does not result from the presence of a Raman active species (e.g., $N_2$, $CH_4$, CO, etc.), but is likely caused by the presence of a noble gas (e.g., He, Ar, Ne).

Using CoolProp (Bell et al., 2014) we assessed the potential He and Ar proportions in the fluid inclusions by calculating their influence on the triple-point temperature of mixed fluids (relative to the melting temperature of pure $CO_2$) using $CO_2$ - He and $CO_2$ - Ar equations of state from (Fig. S29; Kunz and Wagner, 2012).

The EOS calculations also allow us to calculate the densities of $CO_2$-He and $CO_2$-Ar mixed

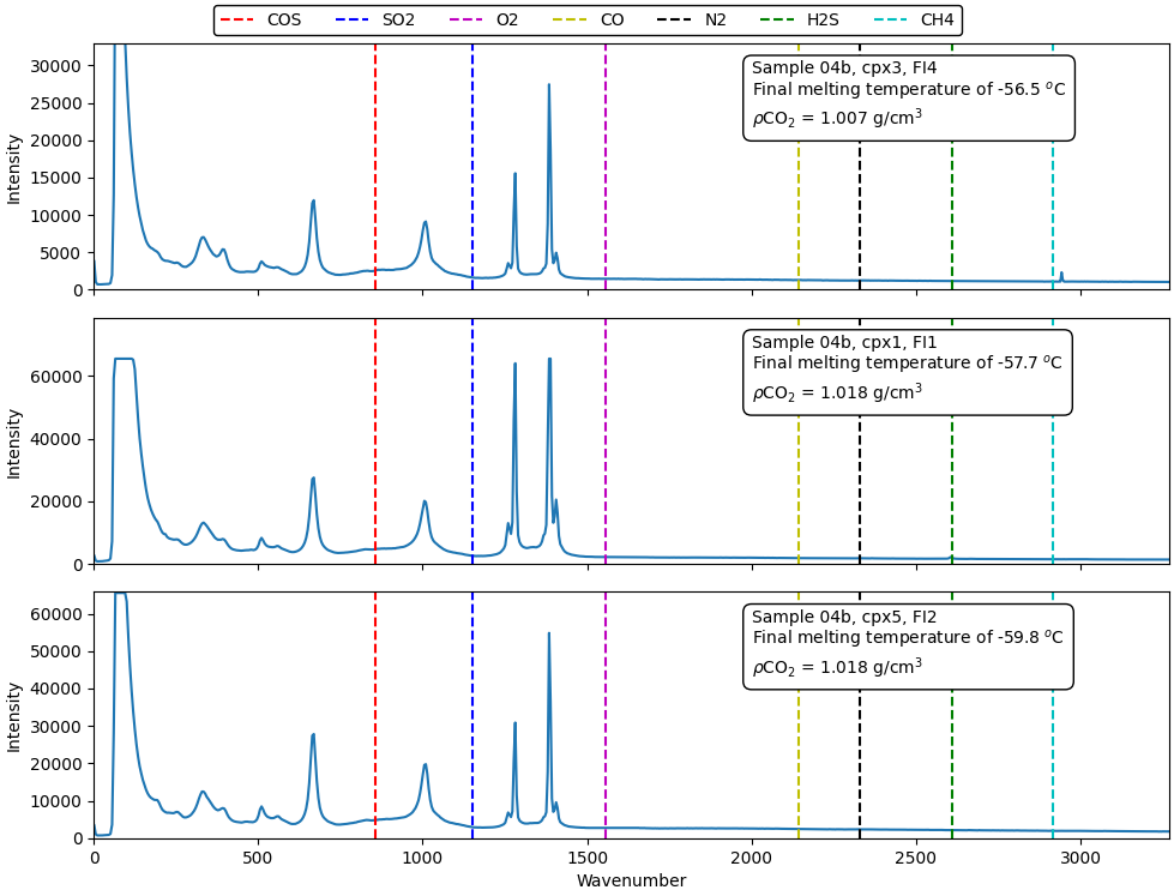


Fig. S.28: Comparison of Raman spectra collected at 49 mW for inclusions showing a range of melting temperatures. Comparison of the spectra demonstrates no notable difference between the different includes with no peaks overlapping with the positions of know Raman vibrations associated with common gaseous species (positions taken from Frezzotti et al., 2012.)

fluids, converting the measured homogenization temperatures (and He or Ar proportions) into these values. Results indicate that the presence of He increases the estimated density (i.e., a greater fluid density is required to match a specific homogenization temperature). In contrast, the presence of Ar in the FIs would lead to a very small reduction in the estimated density (relative to a pure-$CO_2$ fluid; Fig. S30).

Finally, to assess the influence of He and Ar on the estimated entrapment and/or equilibration pressures for the FIs considered in this study, we calculate the position of isochores for theoretical FIs with homogenization temperatures of -17$^o$C and a range of He or Ar contents. Results indicate that the presence of He and Ar have opposite effects on the calculated pressures (Fig. S31). Calculations are performed with increasing temperature until CoolProp is no longer able to calculate the density of the mixed fluid. Typically this limit happens at $<$450$^o$C for calculations involving the presence of He or Ar.

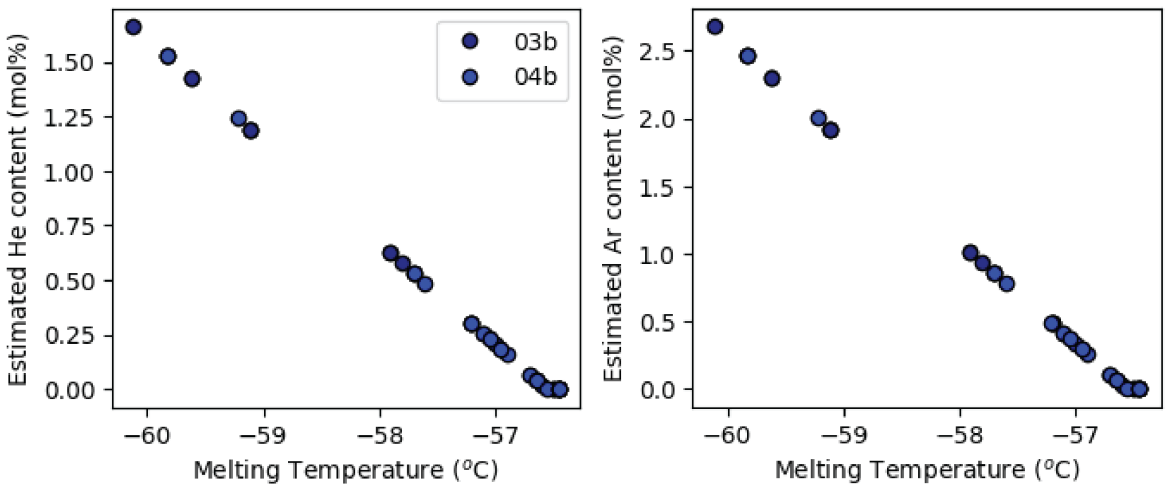


Fig. S.29: Melting temperature of the 03b and 04b fluid inclusions against the He (left) and Ar (right) contents required to cause these melting temperature decreases according to the mixed EOS of Kunz and Wagner (2012).

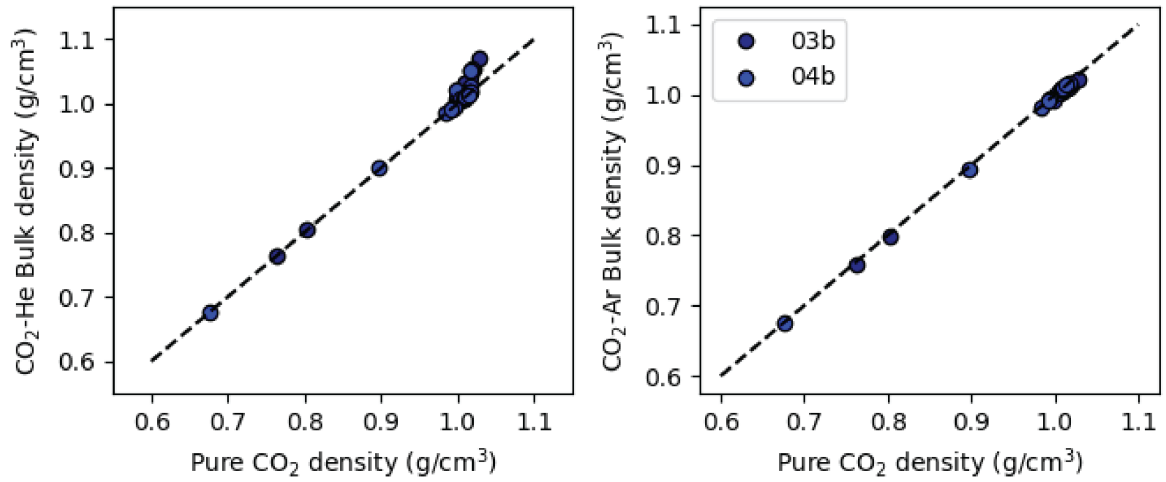


Fig. S.30: Calculated $CO_2$ densities (using the EOS of Span and Wagner (1996)) against estimated $CO_2$-He (left) and $CO_2$-Ar (right) mixed fluid densities using the mixed EOS of Kunz and Wagner (2012).

## Fluid Inclusion Textural Constraints

Within this study we were primarily interested in the inclusions that contain the highest $CO_2$ densities, as these are most likely to record the long-term storage pressure of the gabbro xenoliths/cumulates, rather than relecting processes happening on ascent. For that reason, we targeted fluid inclusions that were typically ¡ 15

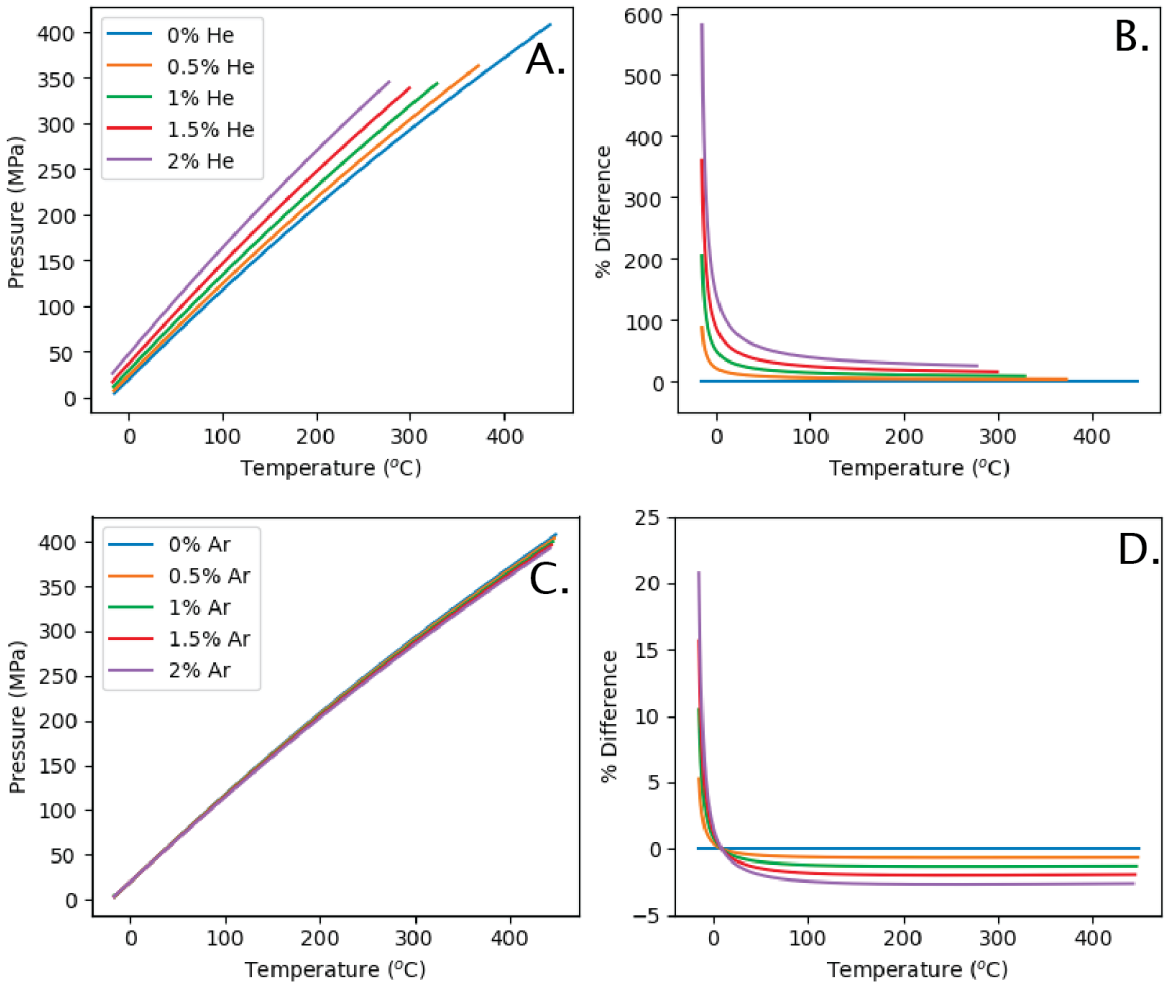


Fig. S.31: Isochores for FIs with different He (A.) and Ar (C.) contents. Results show an increase in pressure with increasing He, but a slight decrease with increasing Ar. Relative pressure variations against temperature are shown in B. (He) and D. (Ar)

$mum$ and are not located on cracks. Some inclusions were identified on cracks/fractures and did not return any signal when analyzed by Raman Spectroscopy, indicating complete loss of $CO_2$ at low pressure (see Fig. S.38). Three inclusions in sample 04b display clear signs of decrepitation (irregular morphology or many smaller bubbles surrounding the main inclusion) and display systematically lower $CO_2$ densities than the rest of the inclusions considered in this study. Finally, the three other inclusions that contain $CO_2$ densities less than 0.9 g/cm$^3$ are larger than the majority of inclusions considered in this study (sample 03b, cpx 2, FI1 & 3, see Fig. 11 of the main text) or are located near a crack and grain boundary (sample 04b, cpx 1, FI3). Both factors are known to make fluid inclusions more susceptible to re-equilibration and could, potentially, explain the lower $CO_2$ densities in these inclusions.

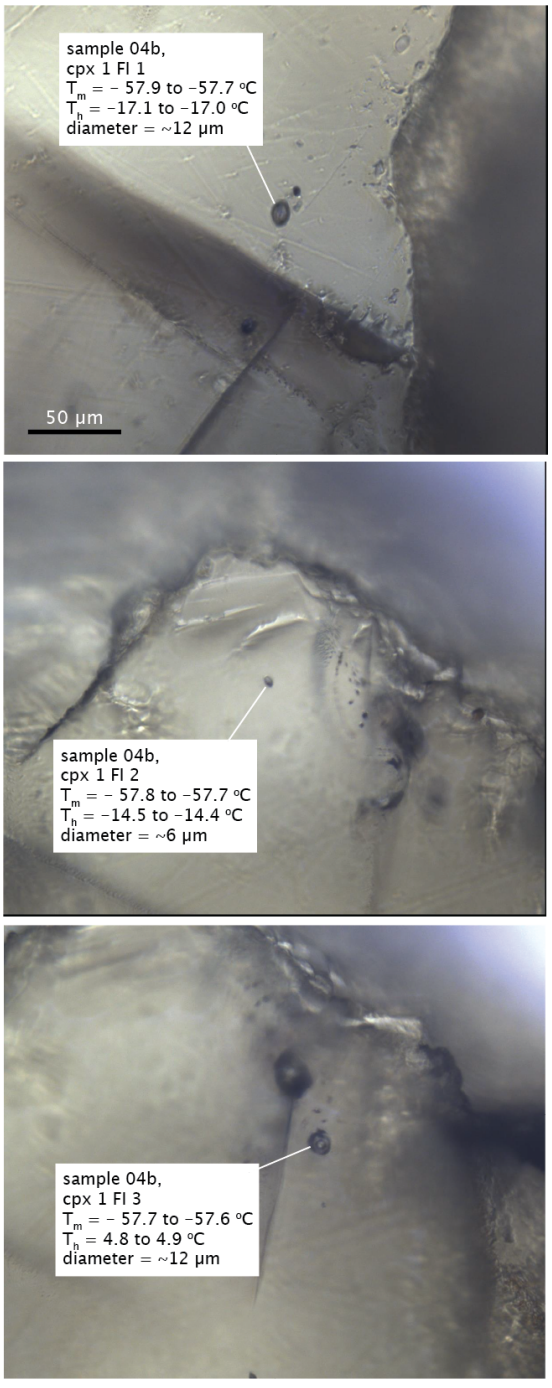


Fig. S.32: Microscope images of fluid inclusions in sample 04b, clinopyroxene 1. Melting and homogenization temperatures, alongside an estimate of the maximum inclusion diameter are given for each inclusion.

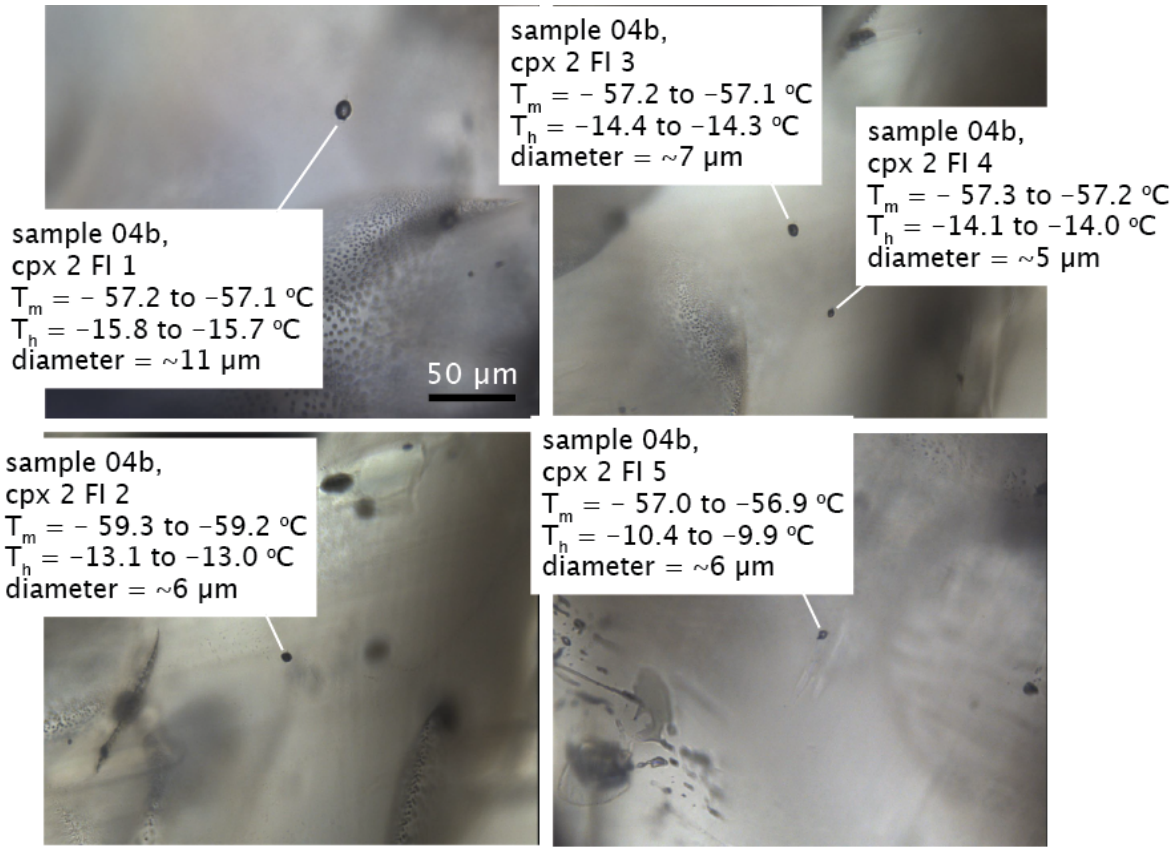


Fig. S.33: Microscope images of fluid inclusions in sample 04b, clinopyroxene 2. Melting and homogenization temperatures, alongside an estimate of the maximum inclusion diameter are given for each inclusion.

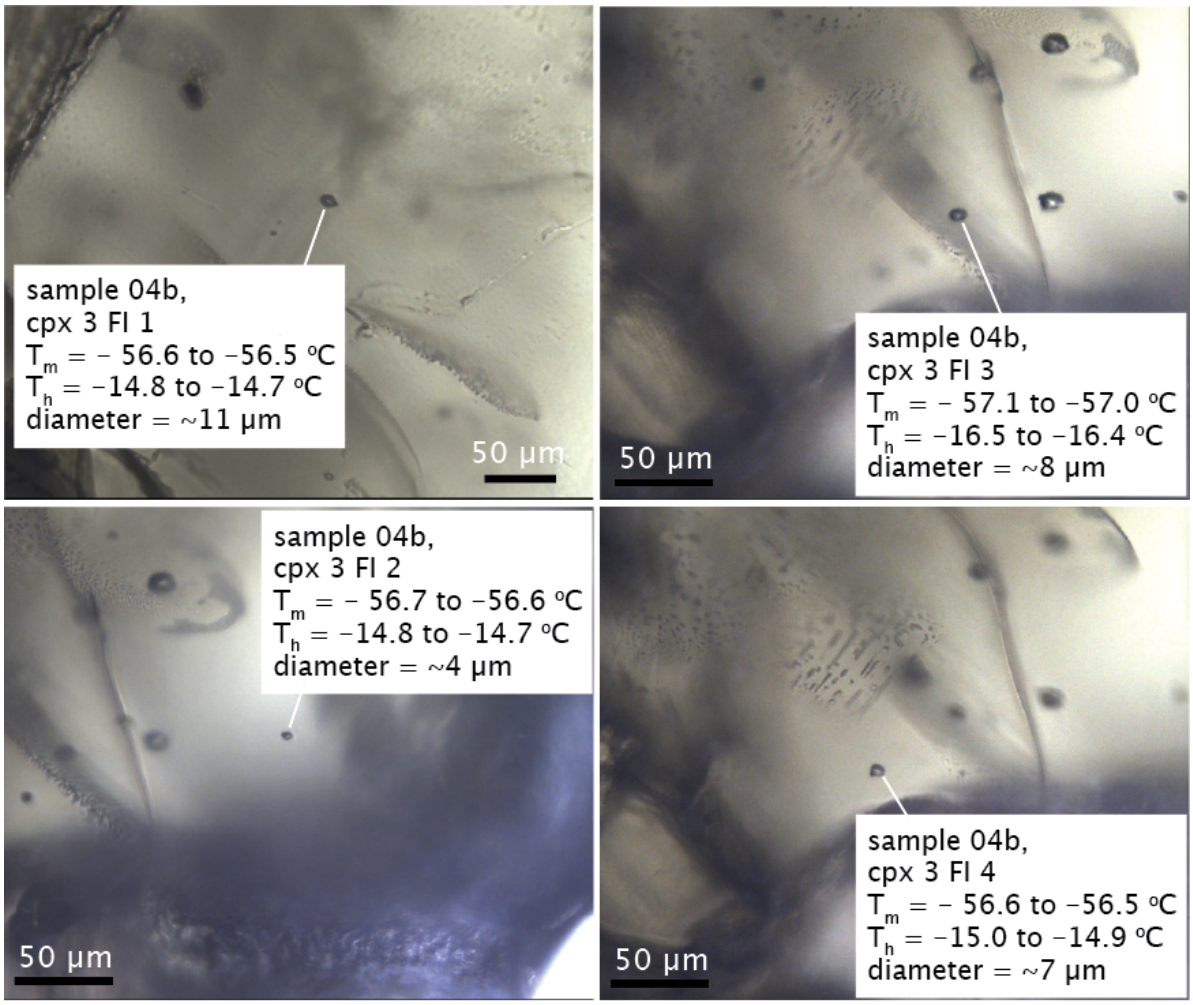


Fig. S.34: Microscope images of fluid inclusions in sample 04b, clinopyroxene 3. Melting and homogenization temperatures, alongside an estimate of the maximum inclusion diameter are given for each inclusion.

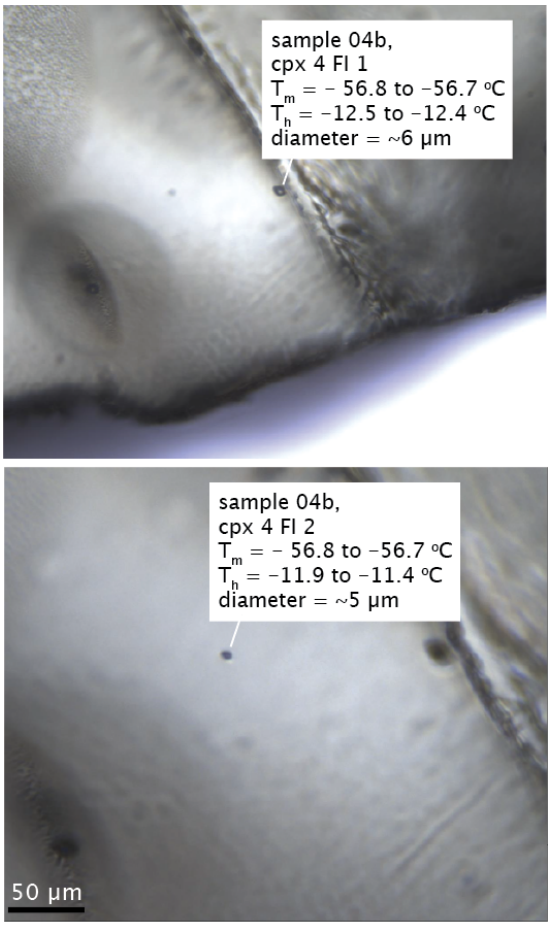


Fig. S.35: Microscope images of fluid inclusions in sample 04b, clinopyroxene 4. Melting and homogenization temperatures, alongside an estimate of the maximum inclusion diameter are given for each inclusion.

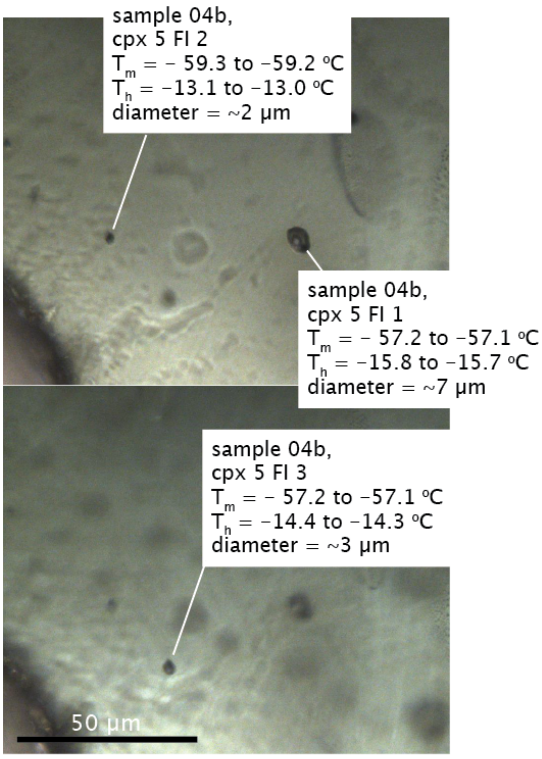


Fig. S.36: Microscope images of fluid inclusions in sample 04b, clinopyroxene 5. Melting and homogenization temperatures, alongside an estimate of the maximum inclusion diameter are given for each inclusion.

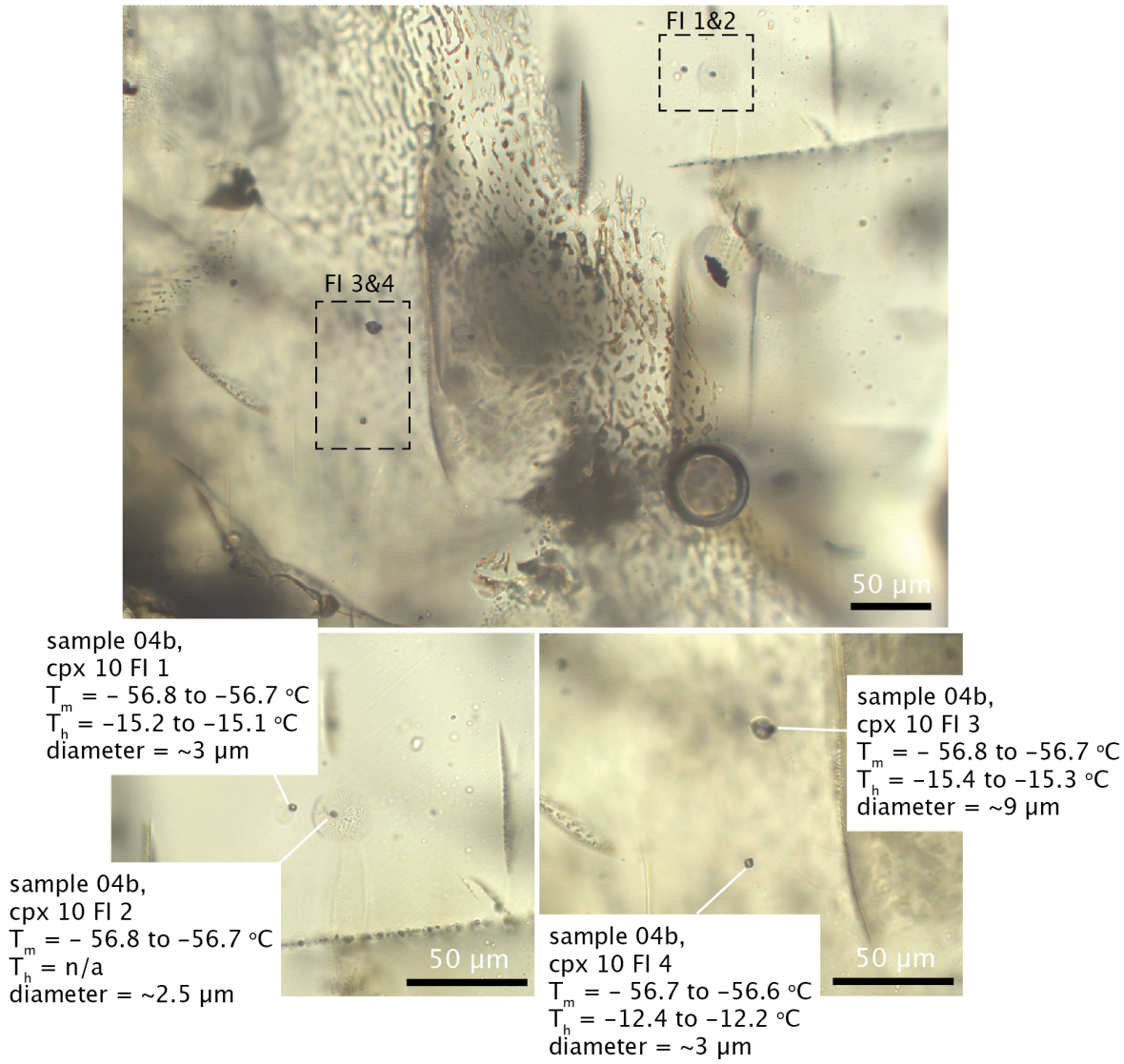


Fig. S.37: Microscope images of fluid inclusions in sample 04b clinopyroxene 10. This figure highlights 2 regions of a crystal with 2 fluid inclusions analyzed in each area. Fluid inclusion 2 displays clear signs of decrepitation and we were not able to determine the homogenization temperature by microthermometry. For other inclusions the melting and homogenization temperatures, alongside an estimate of the maximum inclusion diameter are given.

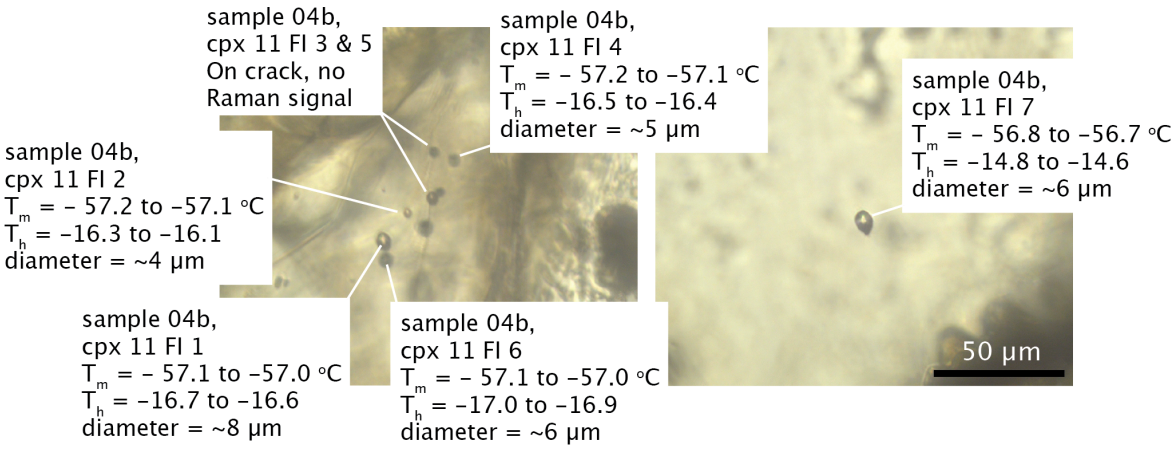


Fig. S.38: Microscope images of fluid inclusions in sample 04b clinopyroxene 11. This figure highlights 2 regions of a crystal with fluid inclusions analyzed in each area. Fluid inclusions 1 - 6 represent a trail of inclusions near a crack in the crystal. Inclusions 3 and 5 are located directly on the crack and we were not able to make any measurements of these inclusions by either Raman Spectroscopy or Microthermometry (indicating a complete loss of $CO_2$ from these inclusions). For other inclusions the melting and homogenization temperatures, alongside an estimate of the maximum inclusion diameter are given.

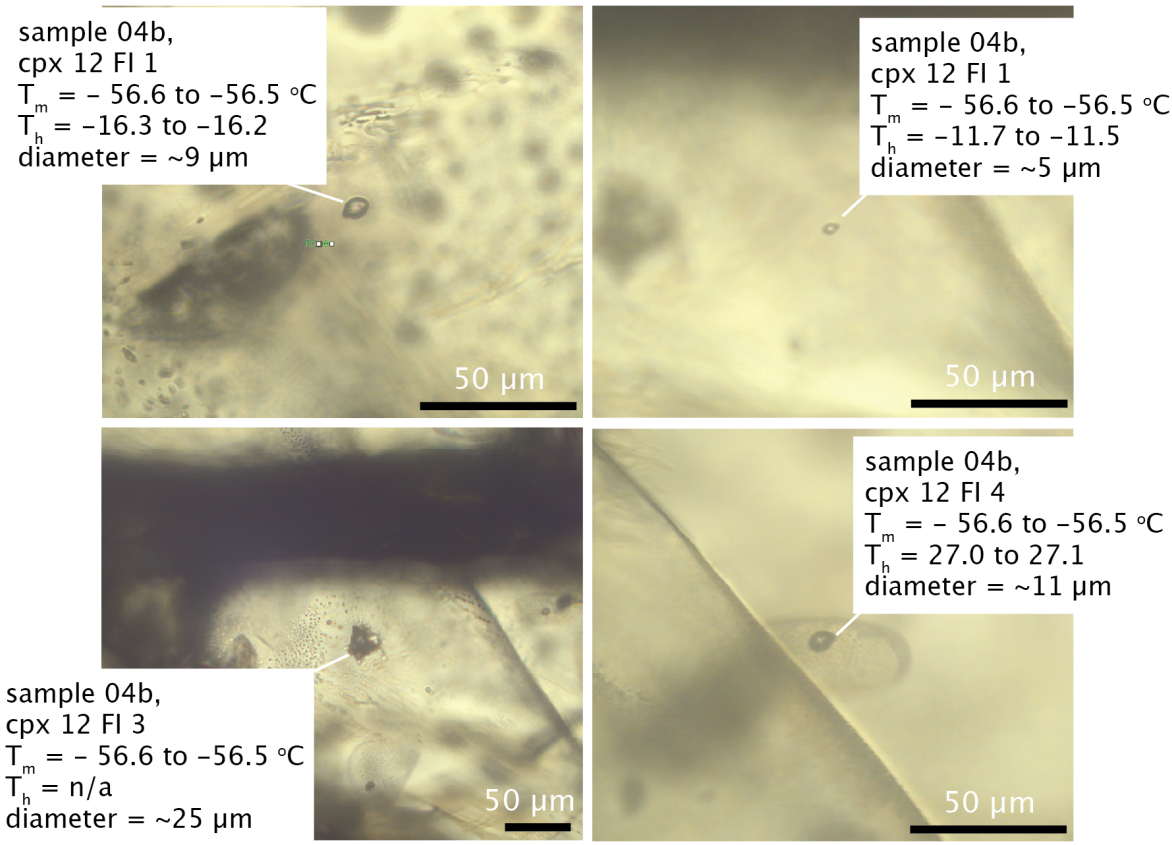


Fig. S.39: Microscope images of fluid inclusions in sample 04b clinopyroxene 12. Fluid inclusions 3 and 4 display clear signs of decrepitation and we were not able to determine the homogenization temperature of fluid inclusion 3 by microthermometry. For other inclusions the melting and homogenization temperatures, alongside an estimate of the maximum inclusion diameter are given.

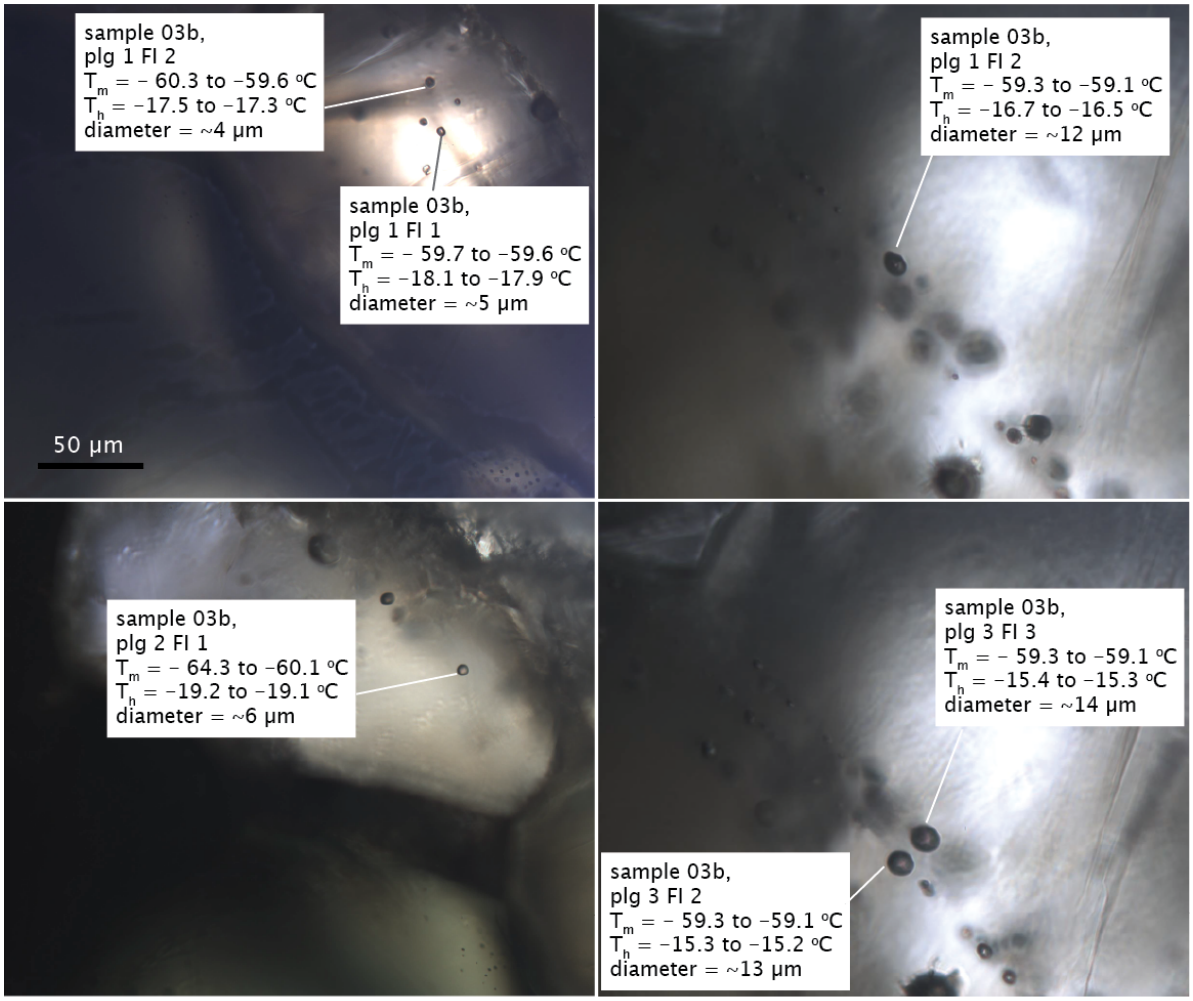


Fig. S.40: Microscope images of fluid inclusions in sample 03b with three separate plagioclase crystals shown (plagioclase 1 - top left, plagioclase 2 - bottom left, plagioclase 3 - right). Melting and homogenization temperatures, alongside an estimate of the maximum inclusion diameter are given for each inclusion.

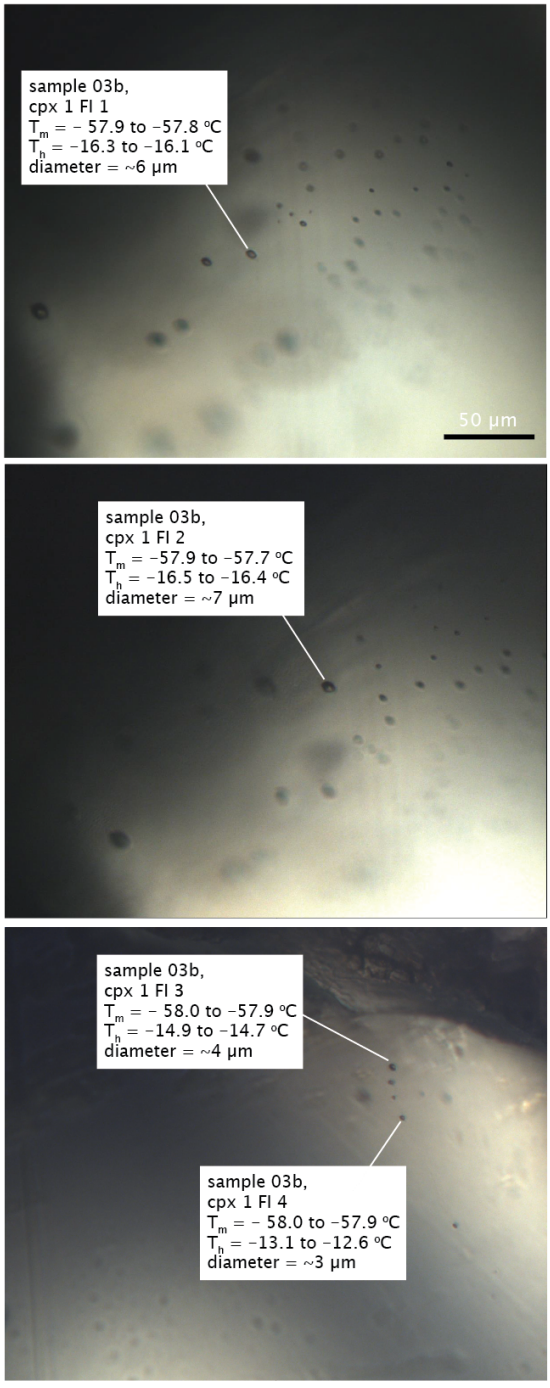


Fig. S.41: Microscope images of fluid inclusions in sample 03b, clinopyroxene 1. Melting and homogenization temperatures, alongside an estimate of the maximum inclusion diameter are given for each inclusion.

# References


Bell, I.H., Wronski, J., Quoilin, S., Lemort, V., 2014. Pure and Pseudo-pure Fluid Thermophysical Property Evaluation and the Open-Source Thermophysical Property Library CoolProp. Ind. Eng. Chem. Res. 53, 2498–2508. https://doi.org/10.1021/ie4033999

Frezzotti, M.L., Tecce, F. and Casagli, A., 2012. Raman spectroscopy for fluid inclusion analysis. Journal of Geochemical Exploration, 112, pp.1-20.

Ghiorso, M.S., Hirschmann, M.M., Reiners, P.W., Kress III, V.C., 2002. The pMELTS: A revision of MELTS for improved calculation of phase relations and major element partitioning related to partial melting of the mantle to 3 GPa. Geochem. Geophys. Geosystems 3, 1–35. https://doi.org/10.1029/2001GC000217

Gualda, G.A., Ghiorso, M.S., Lemons, R.V. and Carley, T.L., 2012. Rhyolite-MELTS: a modified calibration of MELTS optimized for silica-rich, fluid-bearing magmatic systems. Journal of Petrology, 53(5), pp.875-890.

Holland, T.J.B., Green, E.C.R., Powell, R., 2018. Melting of Peridotites through to Granites: A Simple Thermodynamic Model in the System KNCFMASHTOCr. J. Petrol. 59, 881–900. https://doi.org/10.1093/petrology/egy048

Jarosewich, E., Nelen, J.A., Norberg, J.A., 1980. Reference Samples for Electron Microprobe Analysis*. Geostand. Newsl. 4, 43–47. https://doi.org/10.1111/j.1751-908X.1980.tb00273.x

Kunz, O., Wagner, W., 2012. The GERG-2008 Wide-Range Equation of State for Natural Gases and Other Mixtures: An Expansion of GERG-2004. J. Chem. Eng. Data 57, 3032–3091. https://doi.org/10.1021/je300655b

Lyons, J., Geist, D., Harpp, K., Diefenbach, B., Olin, P., Vervoort, J., 2007. Crustal growth by magmatic overplating in the Galápagos. Geology 35, 511–514.

Riel, N., Kaus, B.J.P., Green, E.C.R., Berlie, N., 2022. MAGEMin, an Efficient Gibbs Energy Minimizer: Application to Igneous Systems. Geochem. Geophys. Geosystems 23, e2022GC010427. https://doi.org/10.1029/2022GC010427

Shi, S.C., Wieser, P.E., Toth, N., Antoshechkina, P.M., Lehnert, K., 2023. MIN-ML: Leveraging Machine Learning for Probabilistic Mineral Classification in Geochemical Databases. Presented at the AGU Fall Meetings.

Span, R., Wagner, W., 1996. A New Equation of State for Carbon Dioxide Covering the Fluid Region from the Triple-Point Temperature to 1100 K at Pressures up to 800 MPa. J. Phys. Chem. Ref. Data 25, 1509–1596. https://doi.org/10.1063/1.555991

Takei, H. and Kobayashi, T., 1974. Growth and properties of Mg2SiO4 single crystals. Journal of Crystal Growth, 23(2), pp.121-124.

The Engineering ToolBox (2009). Minerals - Densities. [online] Available at: https://www.engineeringtoolbox.co
density-d_1555.html

Wenk, H.R. and Kroll, H., 1984. Analysis of P-1, I-1 and C-1 plagioclase structures. Bulletin de minéralogie, 107(3), pp.467-487.